A fundamental investigation of the floating overhead power transmission system

羅, 若

A fundamental investigation of the floating overhead power transmission system

（浮体式洋上架空送電システムに関する基礎検討）

羅　若

LUO RUO

ラ　ジャク

February, 2023

Abstract

The increasing demand for energy consumption urges seeking safe, clean and renewable energies. In recent years, many countries have set a series of national-wide policies on exploiting ocean renewable energies to fulfil their goal of decarbonization. Since Japan possesses an immense exclusive economic zone, fully developing its own energy potential is the key to ensuring energy security.

The present thesis concentrates on offshore power transmission, an essential research topic relating to the productivity of ocean energy development. In past engineering practices, submarine cables were the only feasible solution. However, its maintenance cost, transmission loss and sensitivity to the seabed environment restrict its applications. According to the deep-water environment in the surrounding seas of Japan, the present work proposes a floating overhead power transmission system (FOPTS) that uses TLP to support transmission conductors learning from the experience of floating offshore wind turbines (FOWTs). In addition to the numerical modelling, water tank experiments and wind tunnel tests are also carried out to verify the reliability of the system, so as to provide guidance and inspiration for subsequent research.

Chapter II focuses on the process and development environment of numerical modelling. First, dynamic modelling of the TLP system is carried out based on classical mechanics, and the overhead conductor are modelled using the lumped-parameter method. Meanwhile, the offshore wind and waves are modelled using the potential flow theory and the wake oscillator model. Wind-wave misalignment, turbulence effect of winds, and other factors were added to the model to consider the actual offshore environment. Using MATLAB SIMSCAPE®, each mechanical module is designed

separately and can be freely combined to perform efficient FOPTS numerical simulations.

Chapter III introduces the water tank experiment for verifying the hydrodynamic module. A TLP model is created using 3D printing and equipped with a pulley-wire system to study the wire response. The response of the tower-wire system under regular waves reveals that the sheave mechanic can effectively suppress the motion of the wire without changing the dynamic performance of the TLP itself. At the same time, the experimental results are compared with the numerical simulation, and good consistency is obtained to prove the reliability of the numerical model.

Chapter IV introduces the parametric design workflow for FOPTS. Based on the conclusion of Chapter III, the parameters of TLP and overhead conductor are separately designed in the frequency domain. Based on the research of National Renewable Energy Laboratory (NREL) and Zhao et al. (2012), a three-legged TLP with better hydrodynamic performance is used to ensure the stability of overhead conductor. The newly designed FOPTS parameters are fully listed at the end of the chapter.

Chapter V introduces the wind tunnel test for verifying the aerodynamic module of overhead conductor. The TLP motion in waves is simulated by a stepper motor, and the tension and motion responses of the conductor are studied under different wind and wave conditions. The influence of Everyday Strength (EDS) and subharmonic resonance on the dynamic performance of overhead conductor was observed through experiments. The experimental results are in good agreement with the simulation, proving the reliability of the lumped-parameter method and wake oscillator model in numerical modelling.

Chapter VI conducts a series of numerical simulations. Based on the environmental

data from the Sea of Japan, the response of FOPTS equipped with different types of ACSR conductors is simulated. The numerical study focuses on the safety assessment of the conductor, mooring line and ship navigation. It is found that different conductors respond differently, and an overweight conductor is more sensitive to wind and wave misalignment under extreme wind and wave conditions. Although an overweight conductor has high power transmission efficiency, they should be used carefully in consideration of stress safety. The effect of conductor motion on ship navigation is also studied, and safety clearance for daily navigation is obtained. Regarding mooring lines, the change of wave direction has little effect on the tendon force of the three-legged TLP, while the extreme wind condition affects the lower limit of tendon tension, which is the main factor affecting mooring safety. The influence of the second-order wave force on the calculation accuracy of the conductor response is studied. It is found that when the EDS is small, the influence of the second-order force on the conductor response is more apparent, and the influence of the EDS is less than 3% when the value of the EDS is selected according to the design conditions, which can be ignored to improve the computational efficiency.

Chapter VII summarizes the main conclusions. When the sheave mechanic was introduced, it was proven effective in separating each part of FOPTS for frequency design. Wind-wave misalignment has a clear impact on the performance of overhead conductors, which should be considered in designing. For the design of the overhead conductor, the setting of Everyday strength (EDS) is the most critical, and subharmonic resonance is an essential factor to the safety of power conductor under regular sea conditions. Through experimental verification, the numerical model proposed in this study has been proven reliable. Improvements and prospects for future research are also

given at the end of this chapter.

Table of contents

CHAPTER I

Introduction

1.1 Historical background

The oceans provide vast renewable energy resources [1-4]. Many countries have scheduled offshore power plants as part of their national decarbonization projects to confirm their energy safety (as shown in Fig 1-1). In recent years, deep-sea development [5-6] has been considered a positive choice in the near future. In offshore development, offshore wind power (OWP), without many limiting factors of onshore wind farms (noise, land use, etc.), shows a potential growth in recent 10 years (as shown in Fig 1-2). In recent years, the price decline of wind power [7] in recent years (as shown in Fig 1-3) caused by technological advancement will promote the OWP industrialized development and lead wind power to become a mainstream energy source for daily life.
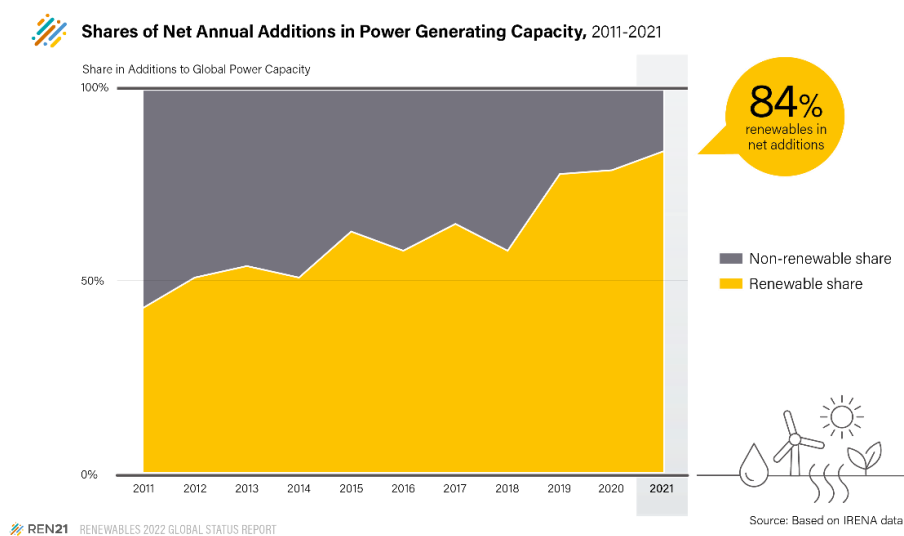
Fig 1-1. Shares of annual net additions in power generating capacity, 2011-2021[7]
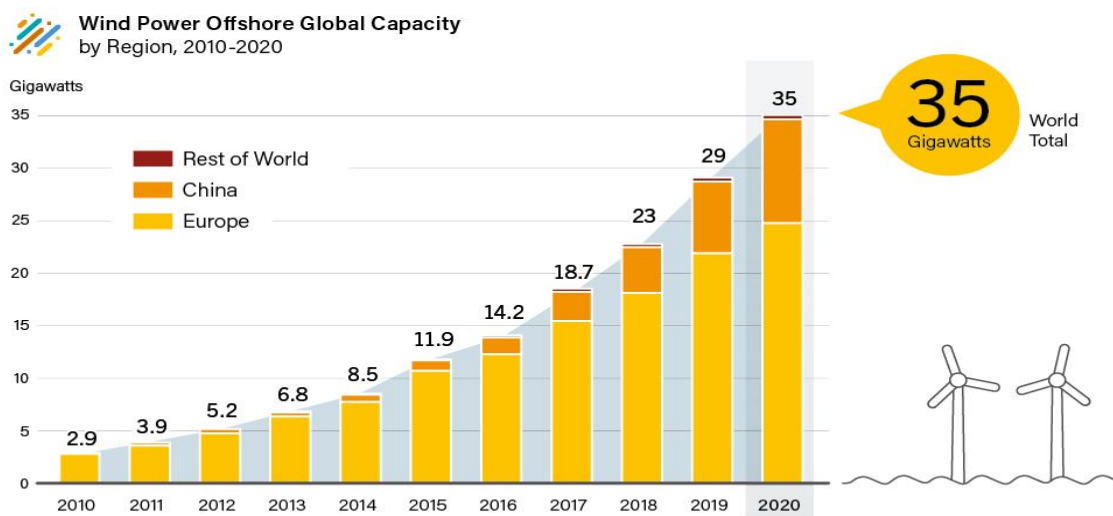
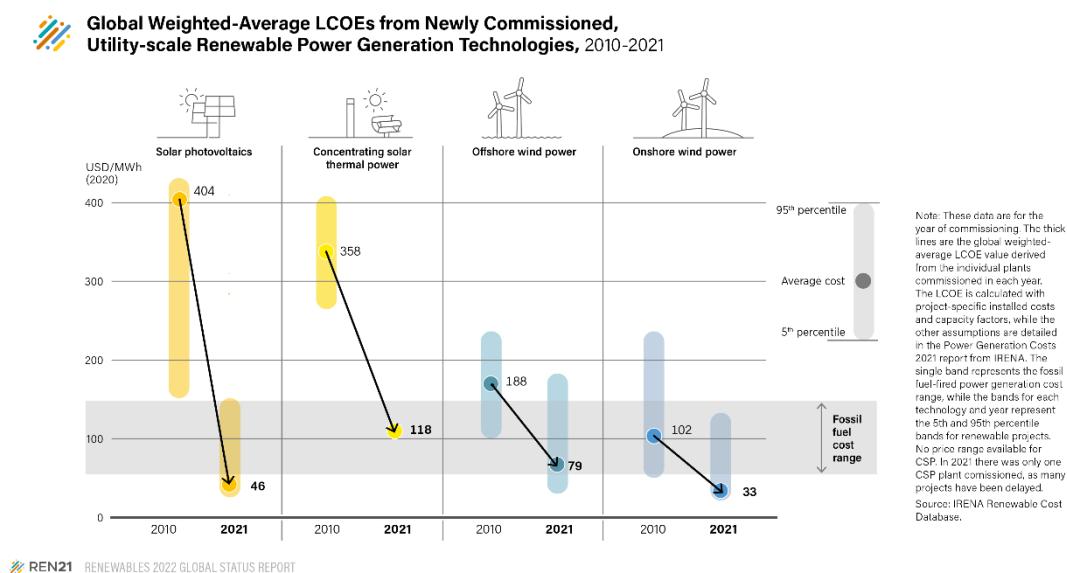Fig 1-2. Offshore wind power capacity, 2010-2020[7].

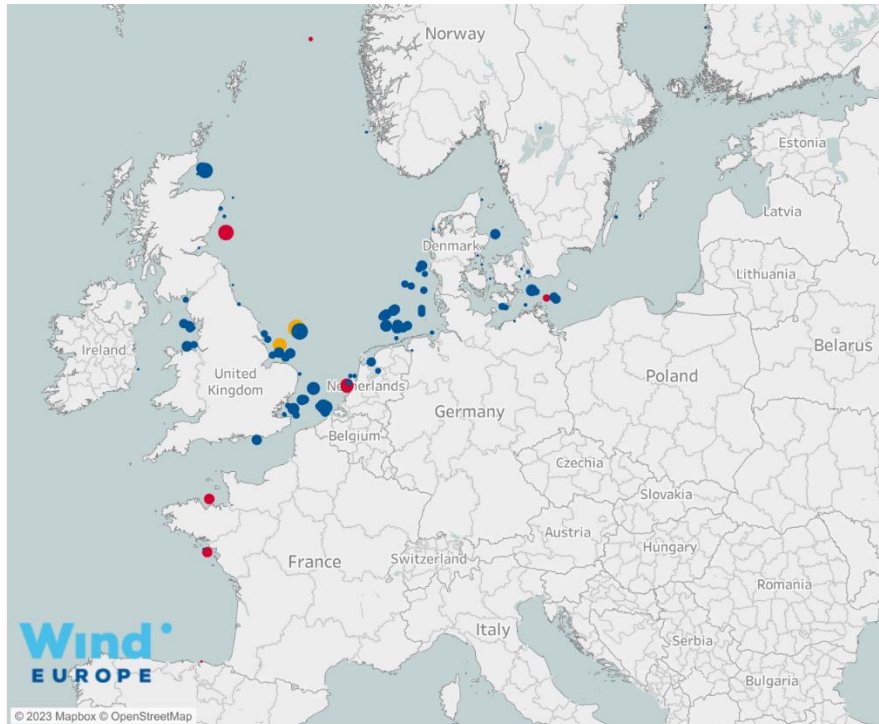Fig 1-3. Decrease for power generation costs of renewable energy, 2010-2021[7]

Fig 1-5. Distribution of offshore wind farms in Europe (blue: in operation; red: under

construction)[12]

Fig 1-4. EEZ of Japan

形式	設置海域		離岸距離 (km)	水深 (m)	風車定格 (MW)	台数 (台)	合計出力 (MW)	運開 (年月)
着床式	北海道	瀬棚港	0.7	13	0.6	2	1.2	2003.12
	秋田県	秋田港	0.1	-	3.0	1	3.0	2015.2
	山形県	酒田港	0.05	4	2.0	5	10.0	2004.1
	茨城県	神栖市	0.04～0.05	4	2.0	7	14.0	2010.2
		神栖市		4	2.0	8	16.0	2013.2
	千葉県	銚子沖 *	3.1	12	2.4	1	2.4	2013.3
	福岡県	北九州沖 *	1.4	14	2.0	1	2.0	2013.6
浮体式	長崎県	五島市 *	1.0	100	2.0	1	2.0	2013.10
	福島県	いわき市 楢葉沖 *	20	120	2.0	1	2.0	2013.12
					7.0	1	7.0	2016.4
					5.0	1	5.0	2017.5
合 計						29	64.6	

*実証研究

Fig 1-5. OWTs operated in Japan[16]

Even though systemic research and engineering development only started at the beginning of this century, many countries have scheduled offshore power plants as part of their national decarbonization projects. China has made a national target of 5 GW offshore capacity by 2020 [8-9]. European countries have a total OWP capacity of 15GW and expect an installation of 150GW by the year 2050 [10-11]. With the development of technology, the primary cost was relatively reduced in the past ten years, as shown in Fig 1-3. For this reason, the World Bank Group has carried out a new program to speed the deployment of offshore wind power in emerging markets, which shows strong confidence in the foresight of this industry.

Japan has an over $4400000 km^2$ EEZ and restores a potential of 1000GW in OWP but shows a slow progress in the offshore power development. Since Japan is highly dependent on the export of fossil fuels, the government started the national project for OWP in 2010 to consider energy safety [13-15]. Even though in the last decade, Japan has been largely behind in promoting related systems of OWP compared to the EU or

China, the highly developed technology provides a strong guarantee for the OWP business. Until 2020, Japan has developed over 60MW OWP installations, including two deep-sea FOWTs, showing a solid technological strength to the world [16]. The goal for OWP installation in the future is shown in Fig 1-6. The Japan OWP will reach a target of 10GW in 2030 and 40GW in 2040. OWP is a vital power source for Japan's electricity demand and decarbonization. In addition, since the business scale is large and the base of related industries is wide, researchers must attract domestic and foreign investment and develop it into a new major industry in Japan.
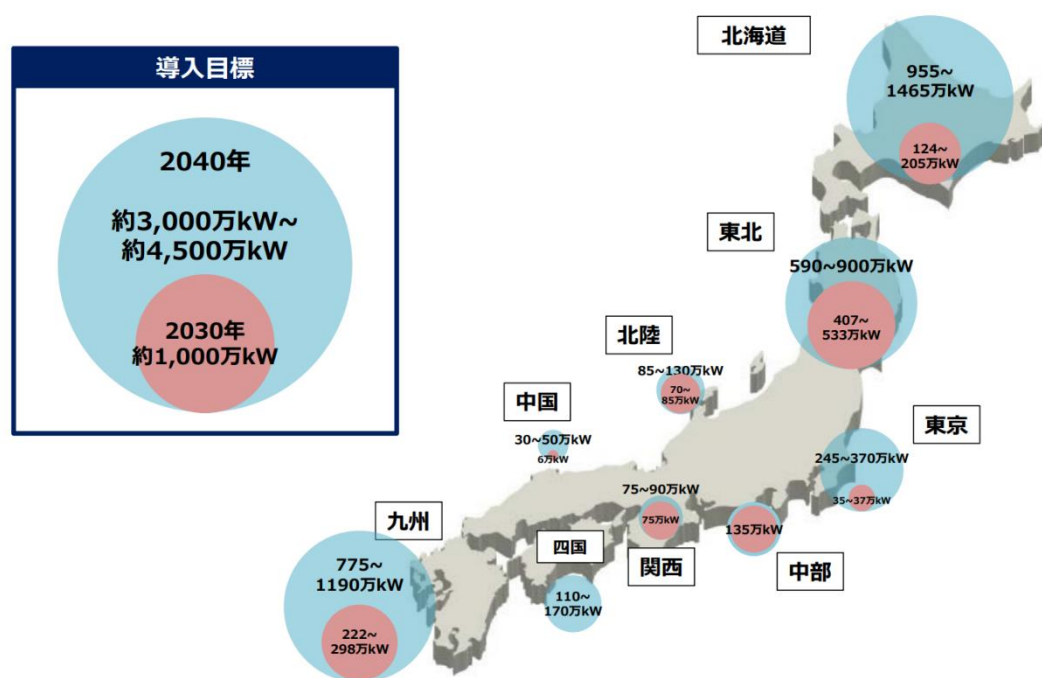

Fig 1-6. Installation plan on OWP of Japan [17]

1.2 Proposal of FOPTS

The present research will focus on the power transmission. Submarine cables are the only practical method for long-distance offshore power transmission [18-19]. Though the cost of cables has been relatively reduced with the development of material

technology [20-21], the maintenance cost (caused by ocean currents, earthquakes, etc.[22-23]) and electrical loss in transmission can reach a high level [24-27] in offshore work condition because of the complex seabed environment. To provide an alternative power transmission method, the floating overhead power transmission system (FOPTS) has recently been studied by RIAM, Kyushu University. The overview of FOPTS can be shown in Fig 1-7. Since bare conductor lines are supported beyond the water surface by transmission towers, FOPTS can significantly reduce the electric loss during power transmission with a low impedance [28]. The maintenance cost for the floating tower and conductor wire can also be lower compared to operations on the seabed.
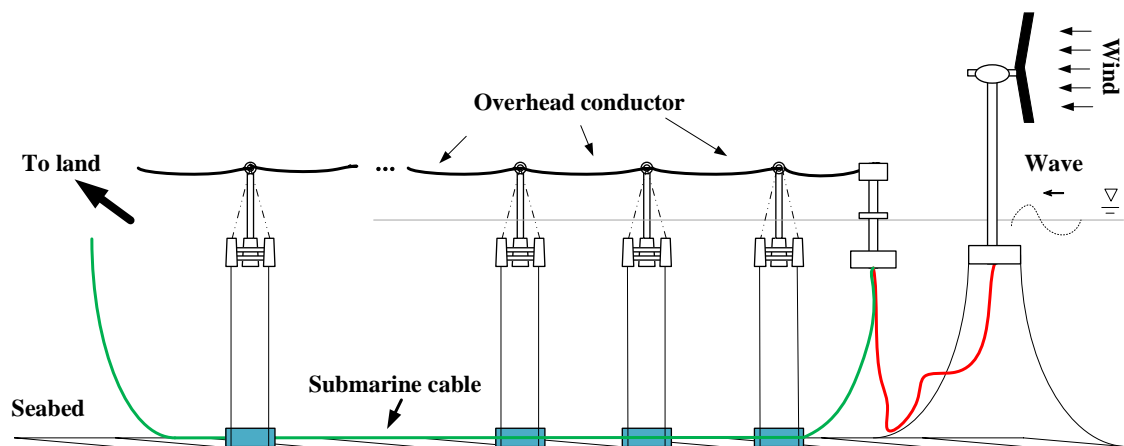
Fig 1-7. Overview of two types of the offshore power transmission system.

1.3 Related research

The background of our research is based on the offshore environment of Japan. Though Japan has the world's top-level exclusive economic zone (EEZ) that reserves a significant amount of wind energy resources [29-30], different to Europe, the OWP for Japan should adapt to the long-distance and deep water environment to satisfy the fact of Japan's sea area.

A typical support structure option for the offshore wind turbine (OWT) is shown in Fig 1-8. From this figure, it is evident that the rigid type foundations (such as monopile, tripod and lattice tower) are always deployed at places within a water depth of 50m. Considering these situations, a floating platform, which has many advantages in deep waters in cost, construction, installation, and decommission [31], should be a possible option for the electric post of FOPTS. Therefore, the design and evaluation of FOPTS could gain experience from the floating offshore wind turbines (FOWT) [32-34]:

(1) Floating foundation design

FOWT is a complex dynamic system with a higher degree of freedom constrained by a mooring system. The usual floating foundation can be a spar, semi-submersible, tension leg, barge, or another innovative platform [35-38]. In the design of FOPTS, the tension-leg platform (TLP) concept is considered promising because of the significant motion reduction compared to other floating types without requiring a large draft like a spar or a spreading mooring system like a semi-submersible.

Moreover, in the form of TLP, a small water plane can effectively reduce the hydrodynamic loads on the floating foundation of FOPTS. Zhao et al. [39] numerically studied two TLP floating wind turbines with different waterplane areas and compared their hydrodynamic performance, certifying that the multi-legged TLP can effectively restrain pitch rotation. Oguz et al. [40] studied a TLP floating wind turbine with a small waterplane area and experimentally proved the significant effect of underwater pontoons in depressing rotations. Since FOPTS is expected to have less load above the water (on the tower and the wire) than FOWT (on the blades and the tower), the design of the underwater part (pontoon, buoyancy column, etc.) is the essential aspect.
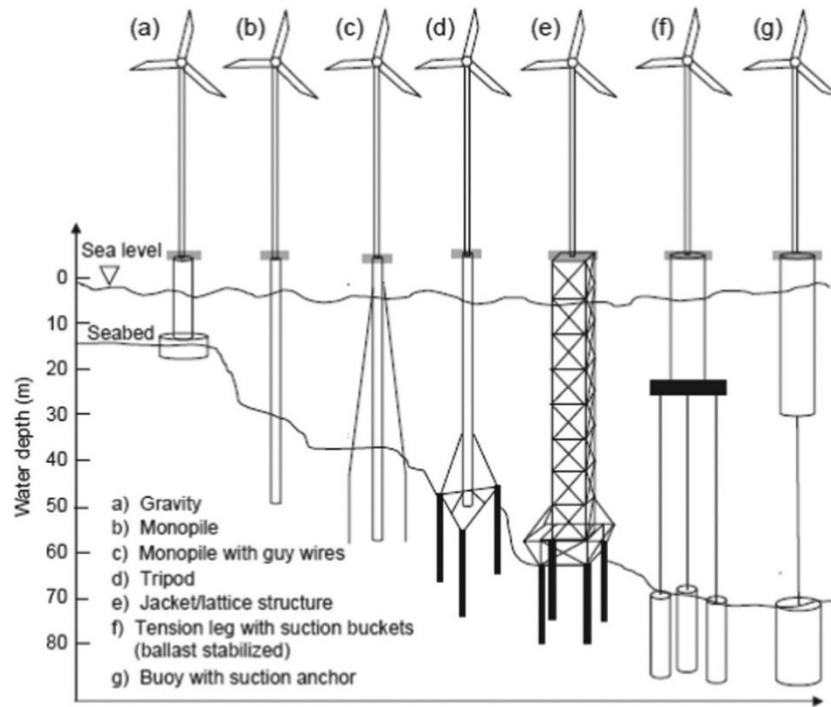
Fig 1-8. Typical support structure options applicable at different water depths [37]

(2) Performance evaluation

A reliable numerical tool is usually required for the simulation under various sea conditions to reduce the overall cost in practical applications. When viscous effects are not dominant for large-diameter marine structures, the boundary integral equation method based on potential flow theory is considered more appropriate in contrast to computational fluid dynamics (CFD) methods, owing to the computational efficiency.

Noticeably, wind-wave misalignment, an unignorable phenomenon in offshore environments, should be carefully considered in the design and simulations. Many researchers, such as Barj et al. [41], Bachynski et al. [42] and Yoshida et al. [43], numerically studied the wind-wave misalignment effects on the FOWT's load and motion. Li et al. [44] developed a numerical model to evaluate the impact on the power output, an essential metric for evaluating an offshore wind farm. For FOPTS, wind-wave misalignment is supposed to affect only the conductor wire due to the absence of

the wind turbine rotor. Therefore, our subsequent studies should concentrate on the behaviour of the overhead conductor.

(3) Safety evaluation

Safety evaluation for a FOWT mainly involves structural strength and mooring. Yeter et al. [45] assessed the ultimate strength of a jacket offshore wind turbine support structures at different water depths. Campanile et al. [46] proposed a selection method of mooring systems for FOWTs in deep water based on ultimate, accidental and fatigue limit state design conditions, with reference to power production, parked wind turbine and mooring line fault conditions. Since the primary purpose of FOPTS is power transmission, researchers should focus their concerns on the safety of conductor wire [47] and mooring system.

Previous relevant works are somewhat limited, possibly because FOPTS is a newly-arisen topic. Pioneering efforts were initially presented by Zhu et al. [48], Hu et al. [49] and then summarized by Zhu and Hu [50]. Numerical simulations and towing tank experiments were carried out to test FOPTS atop triangular TLPs, and an optimization approach was also proposed to handle the overall system's design. Unfortunately, these works focused on the motion response and stability of the floater but gave pretty limited attention to the conductor, which ought to be the primary facility for transmitting the power. To fill the knowledge gap, since knowing the behaviour of conductor wires and their inverse interactions with the floater is essential, the dynamics of conductor wires are carefully modelled and studied in the present study. To this end, a numerical tool for simulating precisely the wire dynamics is developed in a graphical programming environment using Matlab®. The developed tool is validated by

experiment data after that. Worth mentioning is that the support TLP is re-designed to improve the wire's safety under extreme conditions and overcome the shortage of triangle TLP in Zhu [48-50].
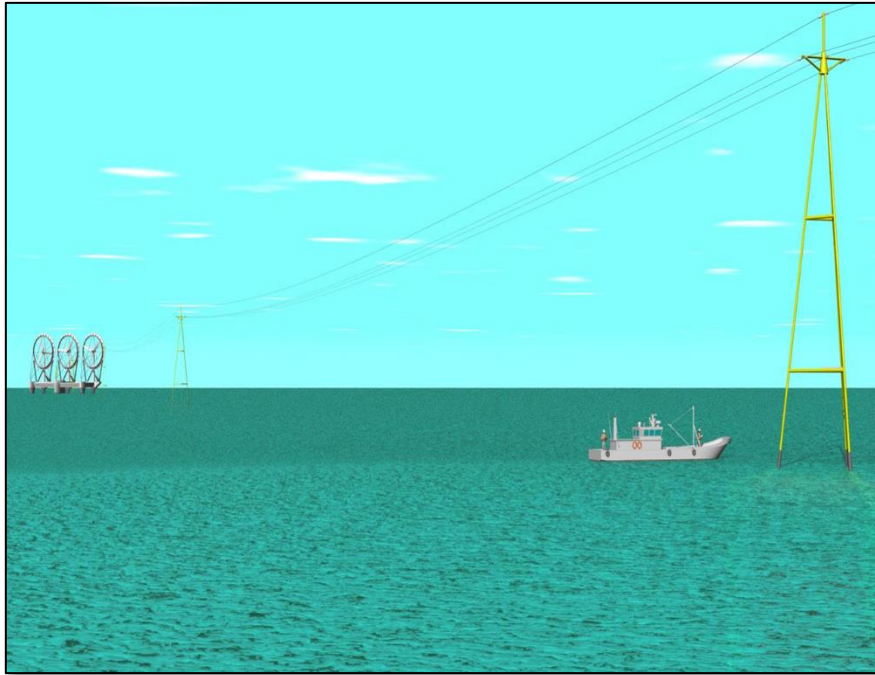
Fig 1-9. An image of offshore overhead power transmission system

1.4 Scope of the present thesis

The present research aims to provide a fundamental investigation of the new proposed FOPTS scheme. The remainder of the paper will be organized as follows: we first outline the fundamental theories and mathematical method used in this work, and the numerical environment applied in the research is also introduced in Section 2.6. In Chapter III, we perform a water tank experiment to study the tower-wire system, and validations to confirm the feasibility of the simulation are also attached in this chapter. In chapter IV, the hydrodynamics of FOPTS are improved accordingly to guarantee the safety of conductor wires, and a control law to adjust the wire force is applied to the

system, which is helpful in affecting the dynamics of overhead conductor wire. To validate the aerodynamic model based on the new design, we present a wind tunnel experiment in Chapter V. A numerical investigation for the offshore environment is described in Chapter VI, composite environmental factors is considered, and safety evaluations for conductor wires and mooring lines are conducted in the research. In conclusion, the numerical method developed in this study could be used in predictions of FOPTS dynamics with acceptable accuracy and contribute to offshore power development.

CHAPTER II

Basic theories and mathematical algorithms

2.1 Introduction

The basic theories and methods applied in FOPTS research will be presented in this chapter. A FOPTS consists of TLP, the conductor wire, and the mooring system. The manoeuvring model of TLP (including the mooring system) will be introduced in Section 2.2, which is based on the classic sea-keeping theories of marine structures. Section 2.3 uses the lumped-parameter method to model the conductor wire. The external loads from the wind-wave environment will be expressed in Section 2.4 and Section 2.5. In section 2.6, the numerical background used to model the FOPTS is declared, and the overview of the numerical model is introduced by a diagram figure.

2.2 Modeling of TLP

2.2.1 Hydrodynamics governing equation

Regarding the floating TLP tower as an oscillating system, the governing equation is based on Newton's Second Law and can be expressed as [51-52]:

$$\sum_{j=1}^{6} \left\{ [M_{ij} + A_{ij}(\infty)]\ddot{\xi} + \int_{0}^{t} K_{ij}(t-\tau)\dot{\xi}(\tau)\mathrm{d}\tau \right\} = F_{exc} + F_{res} + F_{mooring} + F_{wind} \qquad (2\text{-}1)$$

where $\dot{\xi}$ is the velocity vector expressed in the body-fixed coordinate frame according to Cummins Equation. The position vector η expressed in the inertial reference frame can be converted from ξ by the equation below:

$$\eta = J(\varphi, \theta, \psi)\xi \tag{2-2}$$

J is the frame transformation matrix, (φ, θ, ψ) is the rotate direction.

M_{ij}, C_{ij} are the mass matrix and the restoring matrix of the floating body, respectively:

$$M = \begin{bmatrix} m & 0 & 0 & 0 & 0 & 0 \\ 0 & m & 0 & 0 & 0 & 0 \\ 0 & 0 & m & 0 & 0 & 0 \\ 0 & 0 & 0 & J_\varphi & 0 & 0 \\ 0 & 0 & 0 & 0 & J_\theta & 0 \\ 0 & 0 & 0 & 0 & 0 & J_\psi \end{bmatrix}$$

m is the mass of the TLP. The moment of inertia J_φ, J_θ, J_ψ can be calculated by:

$$J_\varphi = mr_\varphi^2$$

$$J_\theta = mr_\theta^2 \tag{2-3}$$

$$J_\psi = mr_\psi^2$$

r_φ, r_θ, r_ψ are the radius of gyrations for each DOF, respectively.

K_{ij} is the retardation function that can be calculated through the cosine transformation of the damping coefficient $B_{ij}(\omega)$.

$$K_{ij}(t) = \frac{2}{\pi} \int_0^\infty B_{ij}(\omega) cos\omega d\omega \tag{2-4}$$

$A_{ij}(\infty)$ is the inifitite-frequency limit of added mass $A_{ij}(\omega)$:

$$A_{ij}(\infty) = A_{ij}(\omega) + \frac{1}{\omega} \int_0^\infty K_{ij}(t) sin\omega t dt \tag{2-5}$$

The coefficients $A_{ij}(\omega)$ and $B_{ij}(\omega)$ can be obtained by potential flow programs, The coefficients $A_{ij}(\omega)$ and $B_{ij}(\omega)$ can be obtained by potential flow solvers, such as WAMIT® [53], HydroSTAR® [54] and HAMS [55-56], by integrating wave pressure over the wetted surface of the structure, obeying potential-flow theory.
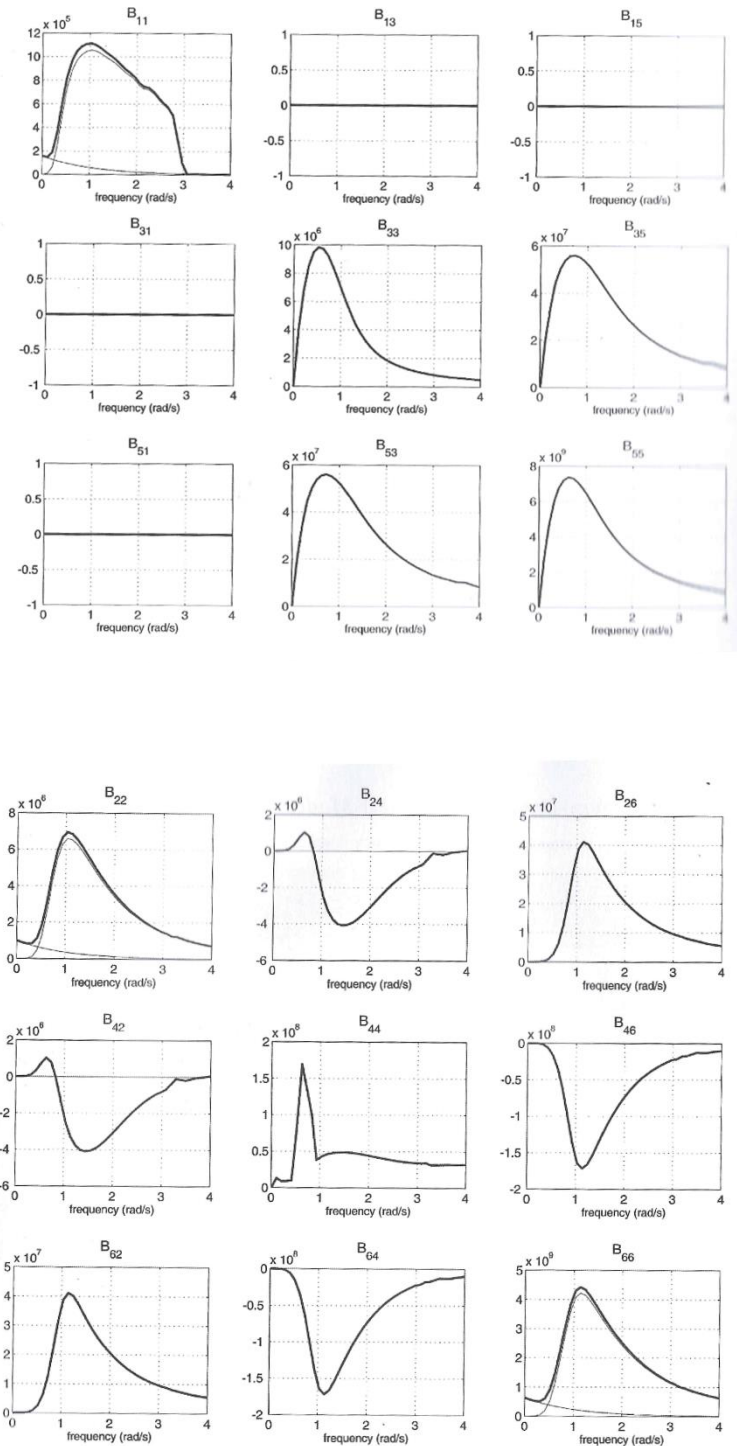
Fig 2-1. A typical example of $B(\omega)$ [51]

As shown in Fig 2-1, the retardation function $K(t)$ would converge to zero after a special time spot, the potential damping can be isolated as:

$$F_{PD} = \int_{-\infty}^{t} K(t-\tau)\dot{\xi}(\tau)\mathrm{d}\tau = B(\infty)\dot{\xi}(t) + \int_{0}^{t} K(t-\tau)\dot{\xi}(\tau)\mathrm{d}\tau \qquad (2\text{-}6)$$

where $B(\infty)$ is the value of $B(\omega)$ when frequency converges to infinite.

External force F_i consists of the wave excitation load F_{exc}, the restoring forces F_{res}, the mooring force $F_{mooring}$, and the aerodynamic loads F_{wind}. The restoring force F_{res} is can be calculated according to the linear model:

$$F_{res} = -\rho g \begin{Bmatrix} 0 \\ 0 \\ A_{wp}z \\ \nabla\overline{GM_t}\varphi \\ \nabla\overline{GM_l}\theta \\ 0 \end{Bmatrix} \qquad (2\text{-}7)$$

where A_{wp} is the water-plane area, $\nabla\overline{GM_t}$ and $\nabla\overline{GM_l}$ are the metacentric height in transverse and longitudinal direction, respectively. $[z, \varphi, \theta]$ is the offset of heave, pitch and yaw.

The mooring force $F_{mooring}$ for TLP can be calculated by referring to Section 2.2.2, and the wave excitation loads consist of first-order term F_{exc}^1 and second-order term F_{exc}^2 can be easily obtained by methods in Section 2.2.4.
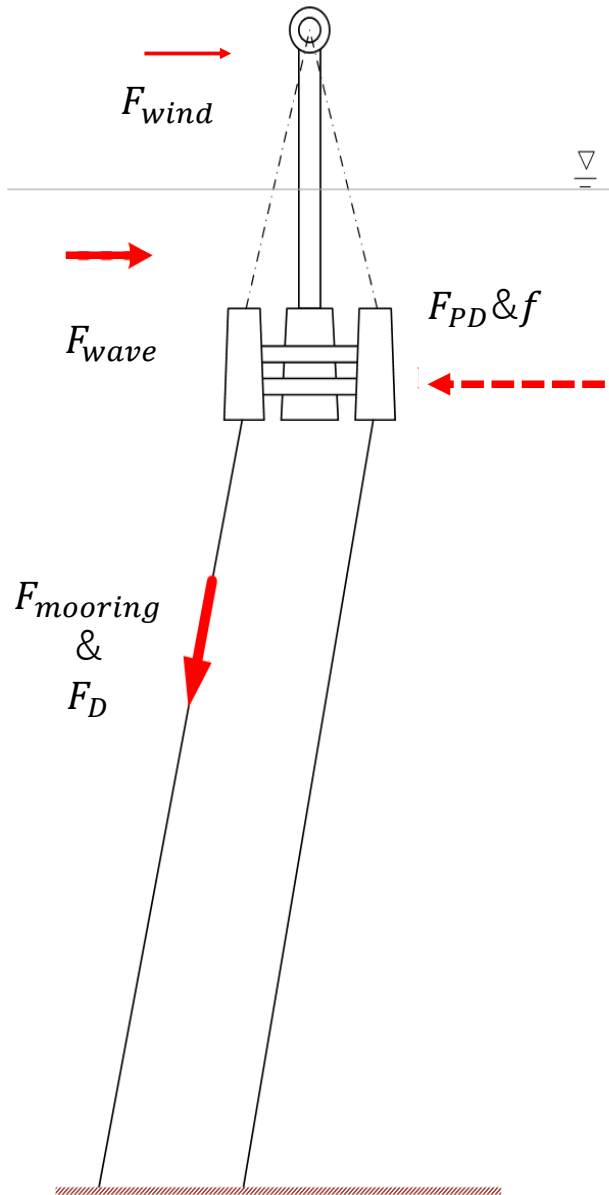
Fig 2-2. A schematic view of TLP tower

The viscous damping [51] of the TLP structure mainly contains potential damping and "vortex shedding" damping. As the potential damping can be expressed by retardation function K mentioned above, vortex shedding damping f is expressed as:

$$f(\dot{\xi}) = -0.5\rho C_D A |\dot{\xi}| \dot{\xi} \tag{2-8}$$

A is the projected cross-sectional area. ρ is the water density.. C_D is drag coefficient determined by Reynolds number R_n, which can be determined by:

$$R_n = \frac{\dot{\xi}D}{v} \tag{2-9}$$

where D is the characteristic length of the calculated part. v is the kinematic coefficient and is usually considered as 1.56×10^6 under a salt water condition. Thus, the damping force and torque can also be calculated approximately by surface integration.

2.2.2 Mooring force

The mooring lines of TLP are always tensioned, and the pretension of tendons can be calculated by:

$$T_0 = \frac{(m_d - m)g}{3} \tag{2-10}$$

where m_d is the displacement of the TLP.

Considering linear elastic mooring line with a strength limit, the hybrid linear elastic spring model can be expressed as:

$$F_m = \begin{cases} 0 & (l_m \leq d_m) \\ k(l_m - l_0) & (l_m \geq d_m) \end{cases} \tag{2-11}$$

where k is the spring coefficient of tendons, which is always considered a constant

when the mooring line is elastic. l_m and l_0 are the exact length and the nominal length of the tendon, respectively.

According to the research by Low [57], when the tendon is tensioned (the mooring system is in operation), for the calculation in numerical simulations, the equivalent stuffiness matrix for a mooring system of hybrid can be written as:

$$K = \begin{bmatrix} K_{11} & & & & & \\ & K_{22} & & & & \\ K_{31} & K_{32} & K_{33} & K_{34} & K_{35} & K_{36} \\ & K_{42} & & K_{44} & & \\ K_{51} & & & & K_{55} & \\ & & & & & K_{66} \end{bmatrix} \qquad (2\text{-}12)$$

Elements in matrix (2-12) can be determined by follows:

(1) Panning stiffness K_{11} , K_{22}, K_{33} :

$$K_{nn} = \frac{T_0 + \Delta T_n}{\sqrt{l_0^2 + {\Delta_n}^2}} \qquad (2\text{-}13)$$

$$\Delta T_n = k(\sqrt{l_0^2 + {\Delta_n}^2} - l_0^2)$$

where n=1,2,3 is the surge, sway and heave DOF (x, y, z) of TLP. Δn is the offset of each DOF:

$$\Delta_1 = x; \Delta_2 = y; \Delta_3 = z \qquad (2\text{-}14)$$

(2) Rotating stiffness K_{44}, K_{55}, K_{66} :

$$K_{44} = kR_{\varphi}^2 \cos\varphi + T_0 \frac{\sin\varphi}{\varphi}\bar{h}$$

$$K_{55} = kR_{\theta}^2 \cos\varphi + T_0 \frac{\sin\theta}{\theta}\bar{h}$$

$$K_{66} = (T_0 + \Delta T_6)\frac{R_{\psi}^2}{\sqrt{l_0^2 + R_{\psi}^2\psi^2}}$$

$$\Delta T_6 = \sqrt{l_0^2 + R_{\psi}^2\psi^2} - l_0$$

(2-15)

where $R_{\varphi}, R_{\theta}, R_{\psi}$ are the distances from mooring point to rotate axis. $\bar{h}$ is the vertical distance from mooring points to the rotate center.

(3) Coupled elements:

For the axis-symmetric mooring type, the coupled elements K_{34} and K_{35} could be adapted as zero. The remainder of coupled elements should satisfy:

$$K_{31} = \frac{T_0}{x}\left(\frac{l_0}{\sqrt{l_0^2 + x^2}} - 1\right) + \frac{\Delta T_1}{x}\frac{l_0}{\sqrt{l_0^2 + x^2}}$$

$$K_{32} = \frac{T_0}{x}\left(\frac{l_0}{\sqrt{l_0^2 + y^2}} - 1\right) + \frac{\Delta T_2}{x}\frac{l_0}{\sqrt{l_0^2 + y^2}}$$

$$K_{36} = \frac{T_0}{x}\left(\frac{l_0}{\sqrt{l_0^2 + R_{\psi}^2\psi^2}} - 1\right) + \frac{\Delta T_6}{x}\frac{l_0}{\sqrt{l_0^2 + R_{\psi}^2\psi^2}}$$

$$K_{42} = \bar{h}K_{22}$$

$$K_{51} = \bar{h}K_{11}$$

(2-16)

Thus the mooring force could be written as:

$$F_{mooring} = K\xi$$

(2-17)

The systemic damping of TLP is considered to be produced by mooring system, the damping force can be written as:

$$F_D = C\dot{\xi} \tag{2-18}$$

where C is the damping matrix which can be expressed as a diagonal matrix and can be calculated by

$$C_{nn} = 2\zeta\sqrt{k_i'm_i} \tag{2-19}$$

C_{nn} (n=1,2…6) is the element of matrix C. k_i' is the eigen stiffness in each DOF and ζ is the structural damping ratio of TLP.

2.3 Conductor wire model

Assuming the conductor wire as an ideal elastic body, the lumped-parameter method [58-59], which approximates a flexible body as a collection of several discrete flexible units, is applied for modeling the conductor, as shown in Fig 2-3.
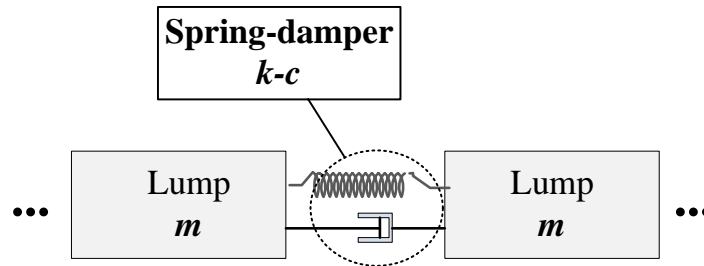

Fig 2-3. Conductor wire unit modelled by lumped parameter method

One flexible unit comprises two mass elements coupled with elastic joints, and the elastic properties can be possessed by the internal springs of transition, bending and rotation. The spring coefficients of the joints are assigned by Hooke's Law [68]:

$$K_{axial} = \frac{EA}{dl}$$

$$K_{bend} = \frac{EI}{dl} \qquad (2\text{-}20)$$

$$K_{rotate} = \frac{GJ}{dl}$$

where *E*, *G*, *I*, *J*, and *A* are the Young's modulus, shear modulus, second moment of sectional area, torsional constant, and sectional area of the conductor, respectively. dl is the length of the flexible unit.

For the connection between adjacent tower, the connect points of conductor wire can be convert by coordinate transform matrix:

$$\begin{bmatrix} x \\ y \\ z \end{bmatrix} = \begin{bmatrix} x_0 \\ y_0 \\ z_0 \end{bmatrix} + T \begin{bmatrix} x_p \\ y_p \\ z_p \end{bmatrix} \qquad (2\text{-}21)$$

$[x_0, y_0, z_0]$ is the earth coordinate of TLP, $[x_p, y_p, z_p]$ is the coordinate of connect point to TLP local system. T is the frame transform matrix and can be written as:

$$T = \begin{bmatrix} \cos\psi\cos\theta & -\sin\psi\cos\varphi + \cos\psi\sin\theta\sin\varphi & \sin\psi\sin\varphi + \cos\psi\cos\varphi\sin\theta \\ \sin\psi\cos\theta & \sin\theta\cos\varphi + \sin\varphi\sin\theta\sin\psi & -\cos\psi\sin\varphi + \sin\theta\sin\psi\cos\varphi \\ -\sin\theta & \cos\theta\sin\varphi & \cos\theta\cos\varphi \end{bmatrix}$$

$$(2\text{-}22)$$

2.4 Hydrodynamic load model

Since reducing computational loads is the first need in practical works, the boundary integral equation method (BIEM) based on the potential flow theory should still be the

first choice to evaluate the overall performance of large marine structures, compared to the computational fluid dynamics (CFD) methods based on the N-S equations. The wave load, which consists of 1st wave excitation force, the wave drift load and the sum frequency load, are calculated by diffraction theory [51-52,60-62]. The 1st wave excitation force with respect to the wave frequencies can be calculated by:

$$F_{exc}^1 = \mathbb{R}\left[\sum_{j=1}^{N} \varsigma_j \Gamma(\omega_j, \beta) e^{i(\omega_j t + \Phi_j + \epsilon_j)}\right] \tag{2-23}$$

$\Gamma(\omega)$ and $\angle\Gamma(\omega)$ are the amplitude and phase of the force RAOs according to frequency component, respectively. $\Delta\omega$ is the constant difference between the successive frequencies in the wave spectrum $s(\omega)$. To simulate the irregular wave environments, a random phase ε_ω is generated by a random function.

The wave drift load and sum frequency load are second-order wave loads that act on objects subject to irregular waves, and the values can be expressed by:

$$
\begin{aligned}
F_{exc}^2 = \mathbb{R}\Bigg[&\sum_{k=1}^{N}\sum_{j=1}^{N} \varsigma_k \varsigma_j D(\omega_k, \omega_j, \beta) e^{i[(\omega_k - \omega_j)t + \Phi_k - \Phi_j]} \\
&+ \sum_{k=1}^{N}\sum_{j=1}^{N} \varsigma_k \varsigma_j S(\omega_k, \omega_j, \beta) e^{i[(\omega_k + \omega_j)t + \Phi_k + \Phi_j]}\Bigg]
\end{aligned} \tag{2-24}
$$

Where Γ, Φ are the amplitude and phase of the first-order force RAOs, respectively. β is the wave direction. ϵ is the random phase angle. *D* and *S* are the difference- and sum-frequency quadratic transfer functions (QTFs). Wave amplitude ς_j can be calculated by:

$$\varsigma_j = \sqrt{2s(\omega_j)\Delta\omega} \tag{2-25}$$

$s(\omega_j)$ is the wave spectrum. $\Delta\omega$ is the constant difference between the successive

frequencies.

In addition, the present study uses Modified Pierson–Moskowitz Spectrum (MPM) to simulate the wave loads. Modified Pierson–Moskowitz Spectrum was developed by Pierson and Moskowitz (1963) and improved by International Towing Tank Conferences (ITTC) in 1978, which is used for an open sea environment.

The expression of MPM can be written as:

$$s(\omega) = C\omega^{-5}\exp{(-D\omega^{-4})} \qquad (2\text{-}26)$$

where parameters C and D can be calculated by

$$C = \frac{5\pi^3 \omega_M^4 H_s^2}{16} \quad D = \frac{5\omega_M^4}{4} \qquad (2\text{-}27)$$

where H_s and ω_M represent the significant wave height and modal wave frequency which can be summarized from observation records, respectively.
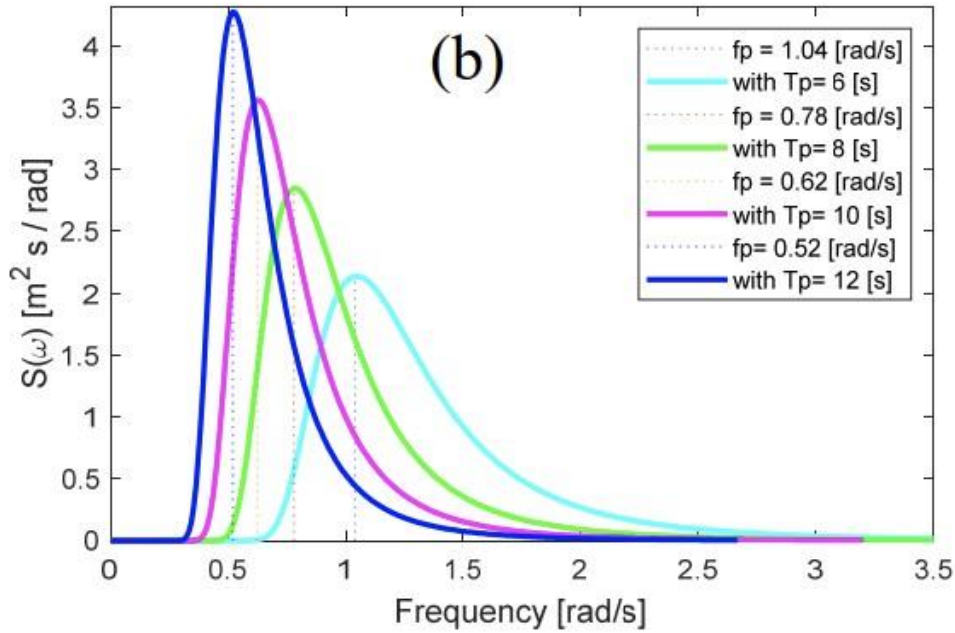

Fig 2-4. Wave simulation based on of P-M spectrum [62]

2.5 Aerodynamic load model

The aerodynamic load would significantly affect the tension and motion of conductor wires. Assuming the wind flows along a constant direction, The aerodynamic loads on each flexible unit are calculated by:

$$F_X = 0.5\rho D C_X U^2 dl$$
$$F_Y = 0.5\rho D C_Y U^2 dl$$

(2-28)

where F_X and F_Y denote the in-line and cross-flow hydrodynamic forces acting on the flexible unit, respectively. ρ is the air density, D is the diameter of the conductor unit (assumed as a cylinder), U is the undisturbed flow velocity. C_X and C_Y are in-line and cross-flow vortex force coefficients, respectively.
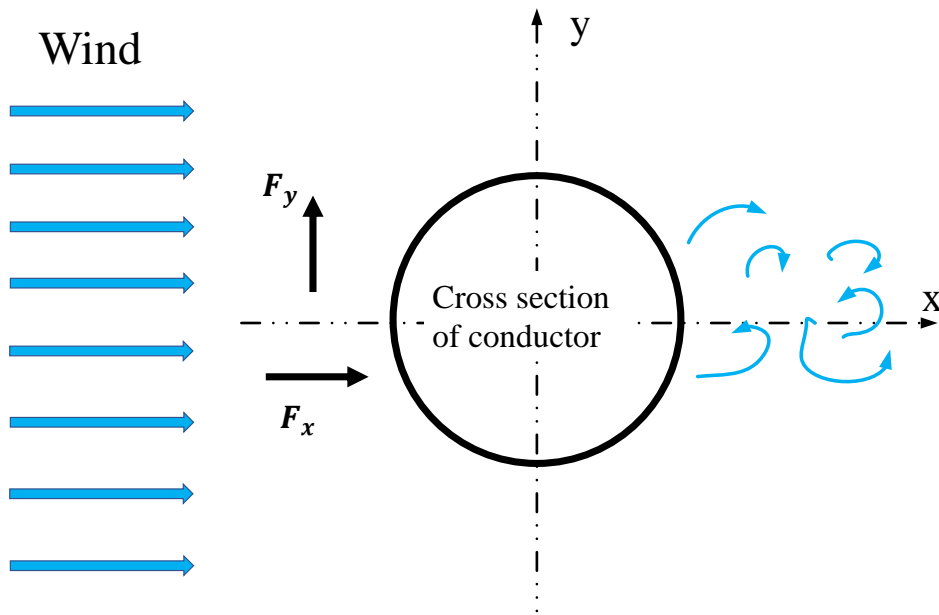

Fig 2-5. Diagram of aerodynamic load on conductor unit

To study the wind-induced conductor motion under the tower-wire interaction, we employ the wake oscillation model [63-64] in coupled expression in this study.

According to the theory, the wake oscillator q is introduced to describe the vortex in aerodynamics, and coefficients C_X and C_Y can be expressed as:

$$C_X = -C_{VL}\frac{v}{U^2}\dot{y} + C_M\frac{v}{U^2}v_x - \alpha C_{VL}^2\left(1 - \frac{\dot{x}}{U}\right)\left|1 - \frac{\dot{x}}{U}\right|$$

$$C_Y = C_{VL}\frac{v}{U^2}(u - \dot{x}) - C_M\frac{v}{U^2}\dot{y} \tag{2-29}$$

$$\frac{d^2q}{dt^2} + \epsilon\omega_s(q^2 - 1)\frac{dq}{dt} + (\omega_s^2 - \frac{\kappa}{D}\dot{x})q = \frac{A}{D}\dot{y}$$

where C_M is the mean drag force coefficient and set as 1.2 in the simulations. ϵ and κ are the tuning parameters determined by the wire cross-sectional shape. ω_s is the Strouhal frequency. C_{VL} is the instantaneous lift force coefficient which is associated to the wake oscillator q and can be calculated by:

$$C_{VL} = 0.5qC_{L0} \tag{2-30}$$

where C_{L0} is the mean lift force coefficient, and the value is set as 0.3 in the study.

2.6 Numerical setup

Definitely, FOPTS is a complex multi-body coupled structure with six Dofs, mainly subject to the environment loads of wind, waves, and currents. Modelling of FOPTS can be handled by Simscape Multibody® [65], a multi-body simulation environment for 3D mechanical systems widely used in simulations for robots [66], vehicle suspensions [67], construction equipment and aircraft landing gear. Taking advantage of the systematic tool, all the mathematical methods mentioned above can be modelled directly by

functional blocks, finally assembling the FOPTS. The structural diagram of the numerical model is given in Fig 2-6.
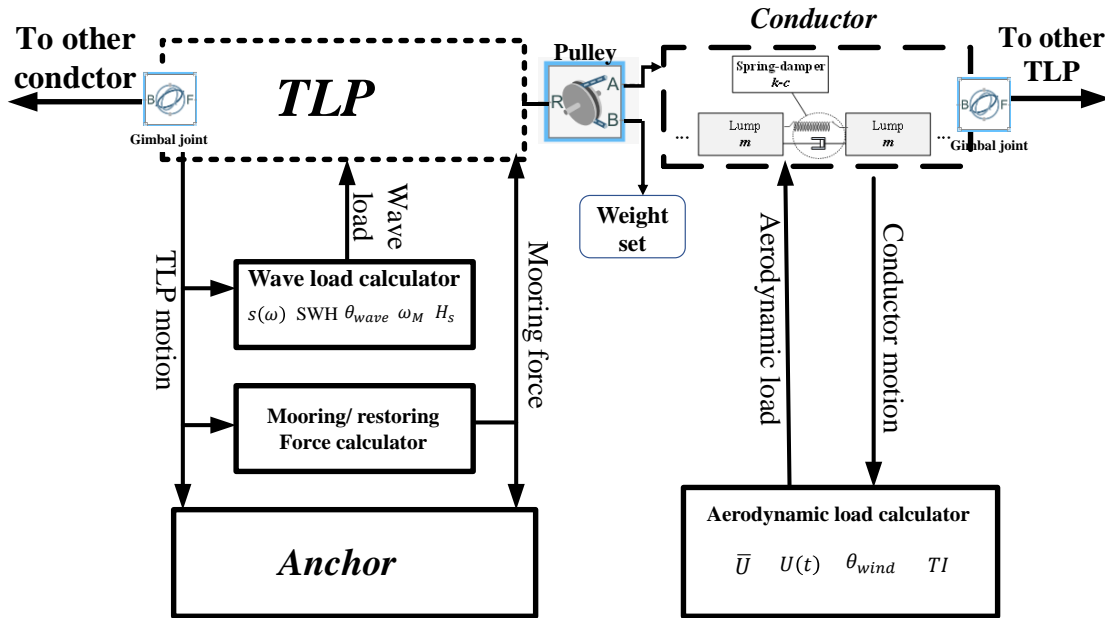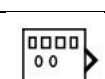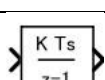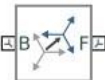

Fig 2-6. Diagram of numerical model

Modules used in the numerical tool are listed as follows [68-69]:

Table 2-1. Modules used in modelling

(1)		Solid block	Represents a solid element with geometry, inertia, color, and reference frame, which could be modified voluntarily.
(2)		Coordinate transform	Applies a time-invariant transformation between two frames. To connect TLPs, seabed and other parts in FOPTS.
(3)		Gimbal joint	Joint with rotational or translational freedoms. Serve as the connections in the lumped-mass model of overhead conductors.
		Prismatic joint	

(4)		Pulley	A grooved or toothed wheel wrapped in a cord. Serve as the intermediate mechanism in FOPTS.
		Belt cable	
		Cable properties	
(5)		MATLAB function	User-defined functions. Serve as hydro loads, aero loads, mooring forces, and restoring forces.
		MATLAB system	
		Signal generator	
(6)		Discrete integrator	Create discrete integrate model, used in calculations for the wake oscillation model
(7)		Transform sensor	Measures the relative spatial relationship between two arbitrary frames. Output the velocity, acceleration and position.
(8)		External force and torque	Blocks that apply general force and torque on rigid body frames. Serve as the forces calculated by (4) in Simcape-multibody system.
		Internal force and torque	
(9)		World frame	The global reference frame in Simcape-multibody system. Serve as the coordinate of the seabed.
(10)		Rigid transform	Applies a time-invariant transformation between two frames. Transfrom the base frame by translations and rotations.
(11)		Bushing joint	Joint with three translational and three rotational degrees of freedom. Represents the equivalent stiffness of mooring line.

(12)		Mechanism Configuration	Provides mechanical and simulation parameters to a mechanism. Parameters include gravity and a linearization delta for computing numerical partial derivatives during linearization.

CHAPTER III

Water tank test for tower-wire model

3.1 Introduction

Water tank experiments [48, 70-71] for triangle-type TLP were performed in 2019 at the Research Institute of Applied Mechanics (RIAM), Kyushu University. This experimental research is based on the previous research by Zhu and aims to study the dynamics of the TLP-wire system. The remainder of this chapter is organized as follows: Firstly, the design aspects of the TLP are introduced in Section 3.2. Then, the experimental setup is clarified in Section 3.3. In section 3.4, validations for the numerical model and experimental results will be presented, and the feasibility of the proposed system will also be discussed for further research.

3.2 Design aspects of the floating tower

Submerged TLPs are considered the supportive platforms for FOPTS because they have large water plane areas for self-stabilization during transportation and small water plane areas for reducing wave loads during operation. The platform is of triangular shape since it would save materials for both hull and tethers, and the foundation could be placed with larger tolerances compared to a four-legged TLP. The overview of a floating tower is shown in Fig 3-1. The anchor is a gravity anchor. However, a suction pile, a driven pile or any other anchoring means may also be used depending on seabed conditions. Synthetic fibre ropes are considered as the tendons since they are light and can retain strength even when wet.
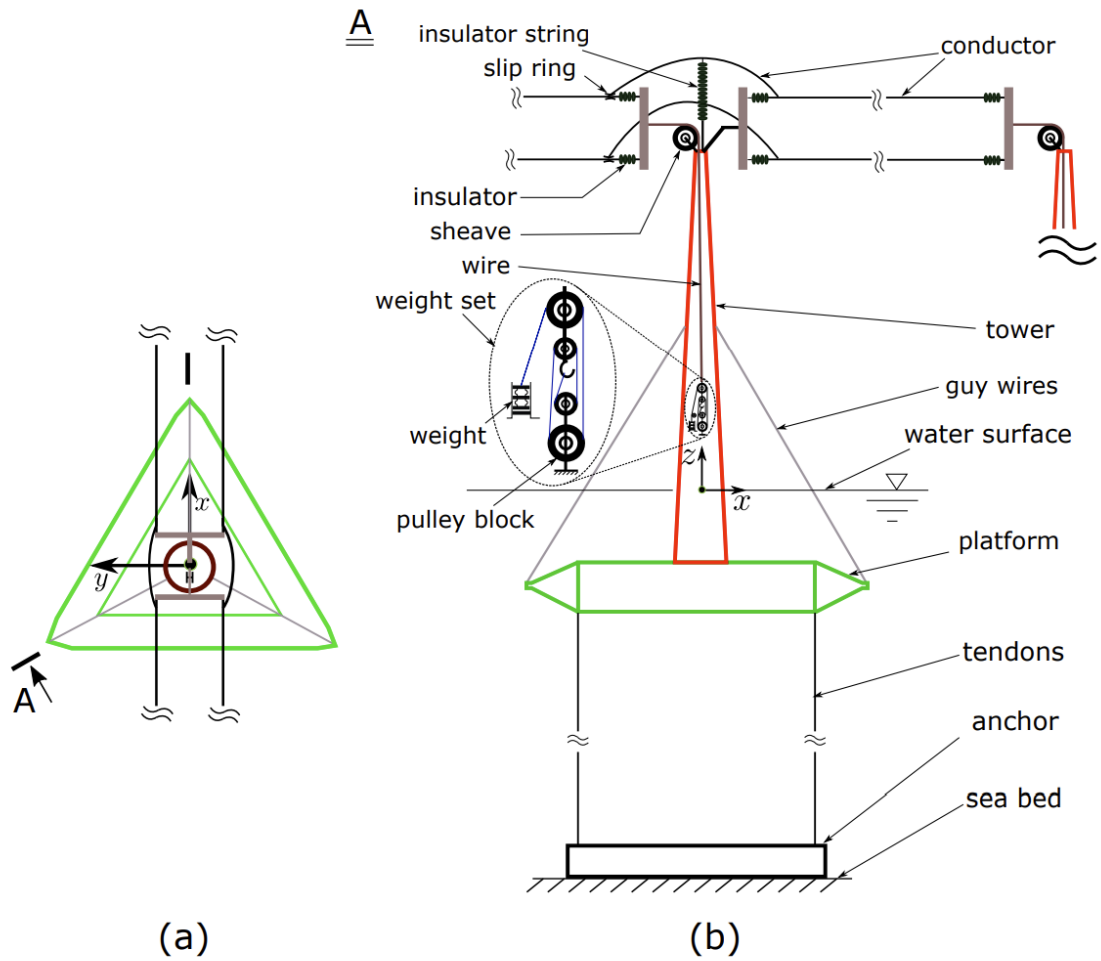
Fig 3-1. A conceptual design of the floating tower: (a) top view   (b) side view.[48]

The platform is placed so that one of its lines of symmetry is parallel with the transmission lines. Tubular steel towers are applied to support the transmission lines since they are proved to be robust for FOWT. On the tower top, a sheave is applied as the intermediate mechanism between the tower and one end of the conductor. Another end of the conductor is rigidly connected to an adjacent tower. A weight set is applied to strain the conductor, and the mass of the weight set (so as the conductor tension) is considered to be adjustable in response to external aero loads. By this consideration, the sag of the conductor would be limited within a safe value even in harsh environments.

In a practical situation, a sheave is applicable for reducing the mass of the weight set, and one example is illustrated in Fig 3-1(b).

Table 3-1 Properties of the TLP tower

Properties	Value
(effective) length of poontoon (m)	19.00
mass (kg)	2.34×10^5
displacement (m^3)	680
radii of Gyration (R_x, R_y, R_z) (m)	$(6.57, 6.57, 9.16)$
added mass coefficient of translational motion $(\epsilon_x, \epsilon_y, \epsilon_z)$	$(0.56, 0.56, 2.16)$
radii of Gyration of added moment of inertia (m)	$(9.30, 9.30, 7.02)$

3.3 Experimental Setup

The TLP platform and the gravity anchor are designed as Δ shaped bodies with through-hole form, as shown in Fig 3-2 and Fig 3-3.

The frame of the TLP platform is produced by a 3D printer. The tower truss is made of aluminium bars with a diameter of 0.02m, and the buoyancy-forming portion of the pontoons is made of cylindrical polystyrene foam. To adjust the mass and reinforce the TLP platform, we set PVC pipes inside the buoyancy part.

The anchor is made of 6 concrete blocks that are fixed by an aluminium frame, which serve as ballast tanks. To control the anchor's buoyancy, tanks are equipped with pipes connected to an air pump, which can change the mass of water in the anchor and adjust the anchor's weight. m. In addition, one set of three stainless wires with a diameter of 2 mm is applied as the tendons of the TLP.

(a) Floater

(b) Tower

Fig 3-2. TLP model for tank experiment

(a) Under assembling
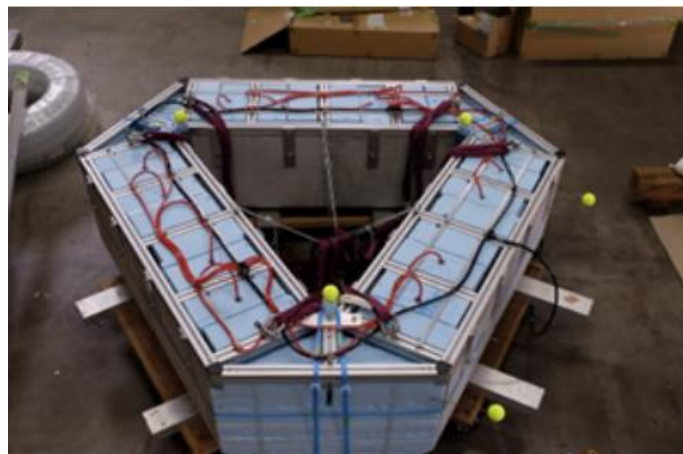
(b) Completed

Fig 3-3. Gravity anchor model for tank experiment

A minimum system consisting of a floating tower and two fixed towers standing in line with the floating tower is considered, and the properties of the system are shown in Table 3-2. Copper wire with a diameter of 0.9 mm is applied to represent the power wires. The tension of the wire can be adjusted by the weights beside the fixed towers. The model experiments were carried out in a water tank with a length 65 m, width 5 m and depth of 7 m at the Research Institute for Applied Mechanics (RIAM) of Kyushu University.
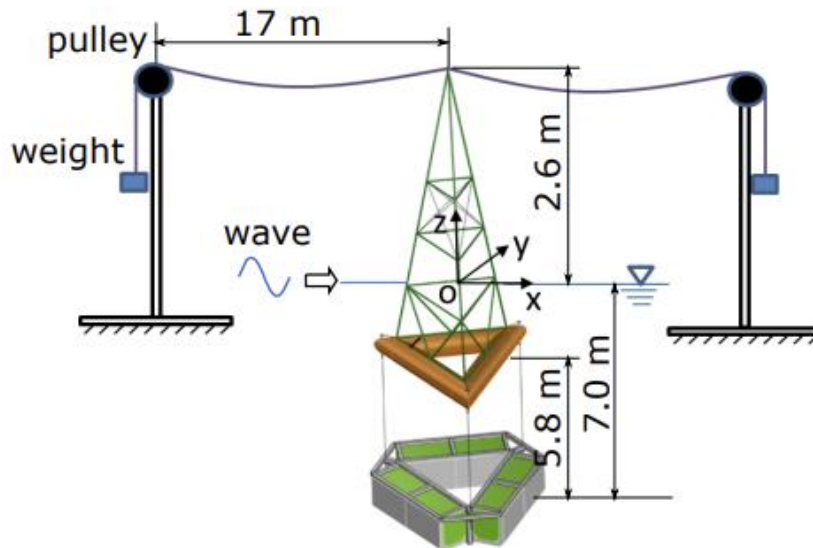
Fig 3-4. Overview of the experimental setup
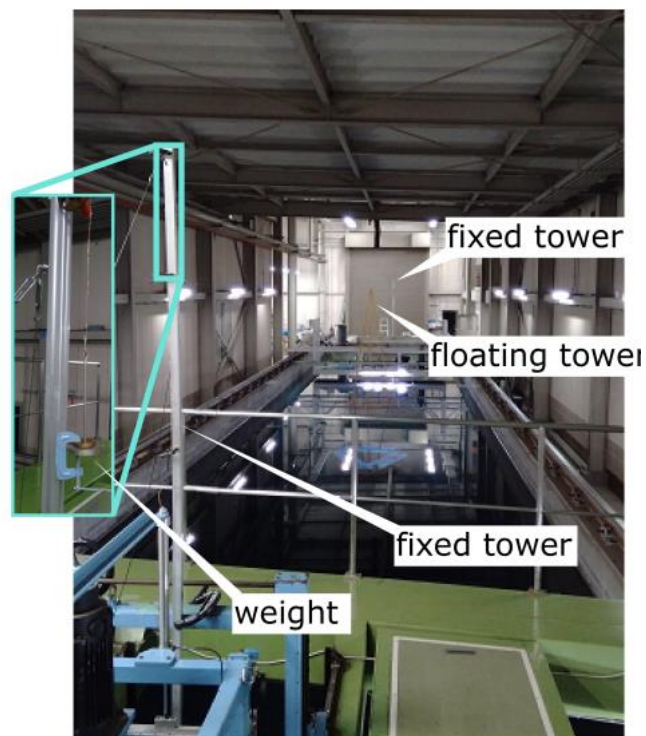
Fig 3-5. Photograph of the experimental setup

Table 3-2. Properties of the model

Property	Platform (with tower)	Anchor
Displacement (m^3)	0.20	0.35
Mass (kg)	22.4	647
Gyration radii (m)	[0.9,0.9,0.6]	[0.5,0.5,0.6]
Side length (m)	1.65	1.2
Diameter/height (m)	0.27	0.40
Mooring distance (m)	1.50	1.50
Weight (kg)		0.8/1.0/1.2/1.4

Table 3-3. Wave conditions for the experiment

Case	Wave Period	Wave Height
1	0.9s	2cm
2	1.1s	3cm
3	1.3s	4cm
4	1.5s	5cm
5	1.7s	6cm
6	1.9s	7cm

The wave conditions used in the experiment are shown in Table 3-3. They are all in the suitability range of linear wave theory and corresponds to the practical situations in an offshore environment.

3.4 Result and discussion

3.4.1 Free decay test of the TLP tower

The free decay response of the floating tower without and with tower-wire connection is first studied. In the cases of tower-wire connection, the tension of wire is adjusted by

changing the mass of the weight as m=0.8 kg, 1.0 kg, 1.2 kg, and 1.4 kg. In the experiments, the initial motion state of the platform in surge, sway and yaw degree-of-freedoms (DOFs) is set away from their equilibrium position by external forces. The forces are then removed to let the model decay freely. The results in surge DOF are shown in Fig 3-6, while the results in sway and yaw DOFs are ignored since their response are very similar to each other.

When the wire is fixed to a rigid port with a pretension of 1.0kgf (about 4% of TLP tower), the free decay curve shows a noticeable difference from others. The natural period of the platform can be investigated by studying the time-series free-decay signals, and the comparison is shown in Table 3-4. It is observed that the natural frequency is little affected by the wire when the pulley is applied. In addition, from the free-decay rate shown in Fig 3-6, it can also be obtained that the fixed tower-wire connection can change the damping factor of the platform.

The logarithmic decrement from the TLP motion, which is defined as the natural log of the ratio of the amplitudes of any two successive peaks, can be calculated by:

$$\Lambda = \frac{1}{n} \ln \frac{X(t)}{X[t + nT]} \tag{3-1}$$

where $X(T)$ is the overshoot of one peak at time t, $X[t + NT]$ is the overshoot of the peak n period away.

The damping ratio of the TLP system is then found from the logarithmic decrement by:

$$\zeta = \frac{1}{\sqrt{1 + \left(\frac{2\pi}{\Lambda}\right)^2}} \tag{3-2}$$

For systems where $\zeta < 0.2$, the damping ratio can approximate as:

$$\zeta \approx \frac{\Lambda}{2\pi} \tag{3-3}$$
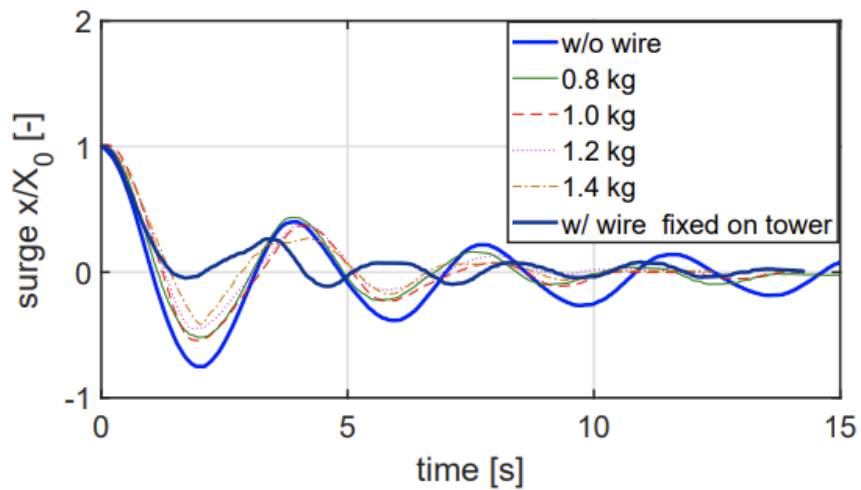
Fig 3-6. Comparison of the surge motion of the free decay test.

Table 3-4. Natural periods of surge for the TLP tower

Case	Period [s]
Without wire connection	3.95s
Pully m=0.8kg	3.92 s
Pully m=0.8kg	3.90 s
Pully m=0.8kg	3.89 s
Pully m=0.8kg	3.87s
Wire connected to rigid	2.5s
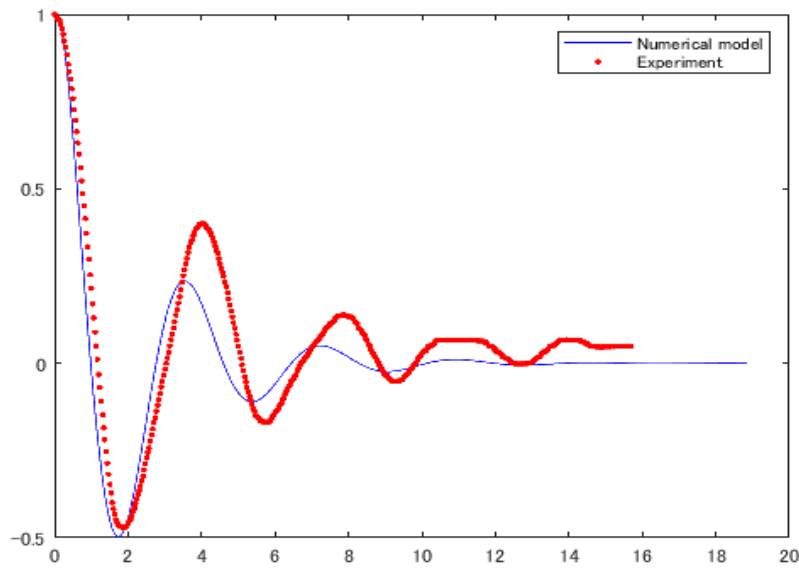
Fig 3-7. Comparison between experiment and simulation of free decay test

Validation of the experiment result and simulation is shown in Fig 3-7. It can be found that the numerical model modelled by formula (2-19) can more accurately reflect the attenuation of TLP in waters. The motion amplitude error may mainly come from viscous damping and water memory damping (calculated according to Section 2.5).

3.4.2 TLP tower motion

The tower motion is captured by another camera set beside the water tank. Same as the free decay test, the weight tied to the copper wire is adjusted to make contrasts. he TLP response to regular wave is shown in Fig 3-8.

The TLP motion is found to have a sudden rise when the wave period is close to 1.5s while the copper wire is connected to a rigid point. However, while the wire is tied to the weight, the TLP motions are almost the same as the change of the wight and increase with the decline of wave frequency.
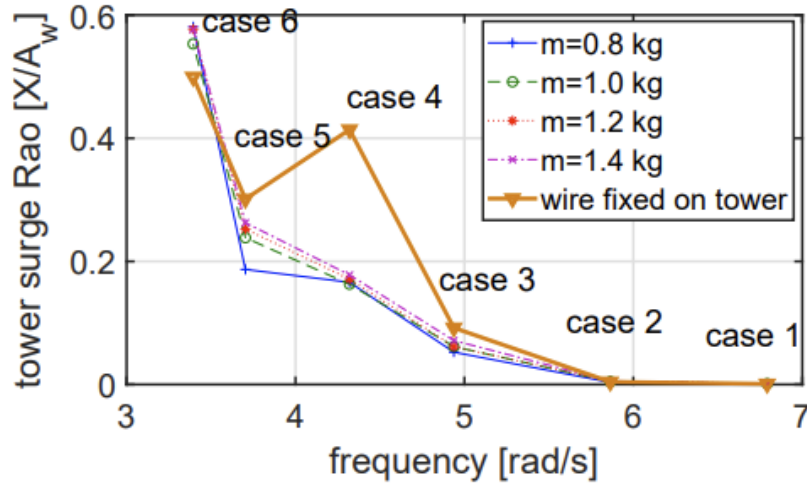
Fig 3-8. Comparison of the tower motion (RAO) in regular waves

3.4.3 Wire motion

To capture the wire motion, a small ball made of polystyrene foam (shown in Fig 3-9) is placed at the centre of copper wire, and a camera is applied to track the motion of the ball. The wire motion during different connections is shown in Fig 3-10.

Fig 3-9. Motion tracking system using a polystyrene ball
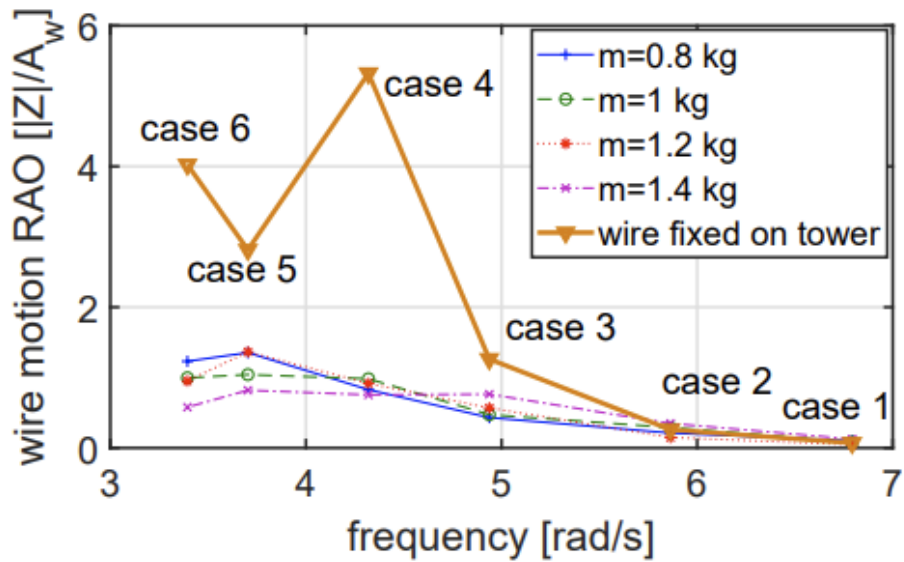
Fig 3-10. Comparison of the conductor motion (RAO) in regular waves
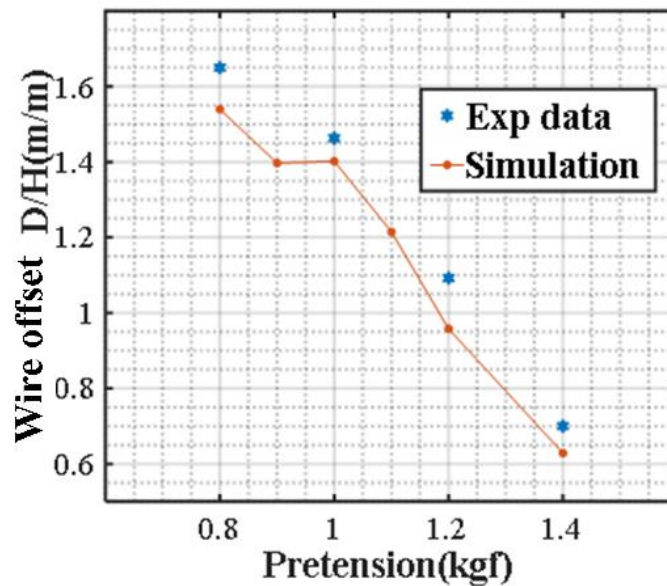
Fig 3-11. Comparison of conductor motion with different pretension

Similar to the motion of the TLP tower, it can be observed that as the wave

frequencies become small, the wire motion increases when the wave frequencies become small, except in case 4 under the condition that the wire is fixed on the tower. In this case, the wave frequency is close to the first symmetric in-plane vibration mode of the wire; therefore, the wire motion is significant. As the wire is fixed on the tower, the tower motion also becomes large owing to the inter-influence between the tower and the wire. In contrast, as the tower's natural frequencies are insensitive to the wire connection when the pulley is applied, the tower motion is smaller than the cases in that the wire is fixed on the tower.

When the wire is connected to the pulley, the wire motion declines by increasing the weight mass, indicating the effect of weight on the wire.

To verify the reliability of the numerical model in for interaction of TLP and tower, the experimental result of wire motion in regular wave conditions is applied to the present model and then made a comparison with the simulation. It is worth noticing that the value in the y-label is the ratio of wire sag D to regular wave height H. Good agreements can be obtained on wire motion, as shown in Fig 3-11. The present numerical model is validated in the simulation of the wire-tower interaction.

3.5 Conclusion

The water tank experiment preliminary explores the wire-tower interaction and then validates the hydrodynamics modules with a good agreement. The major findings are as follows:

(a) In the tower-wire connection system, the wire and tower can affect each other. Especially when the pretension of fixed wire is unneglectable to the TLP weight, the dynamics of TLP would be entirely changed.

(b) The pretension of the overhead wire would determine the wire's natural frequency and coupled motion under the tower-wire connection.

(c) A method using a pulley to mount the wire on the tower was studied, and it was observed that the method could reduce the coupling effects on TLP from the wire, which indicates the possibility for the separated design of TLP and conductor in the FOPTS study.

(d) The validation for the dynamics of wire and tower proves the reliability of the numerical model.

CHAPTER IV

Improvement of the TLP tower design

4.1 Introduction

A previous study by Zhu [50] presents a triangle TLP to support the overhead conductor. However, the triangle TLP shows an over 20-degree variation in yaw under the wind-wave misalignment condition, as shown in Fig 4-1. In significant yaw motion, a large deflection angle at the sheave would be caused, and the wire applied for straining the conductor might be wound during the operation.

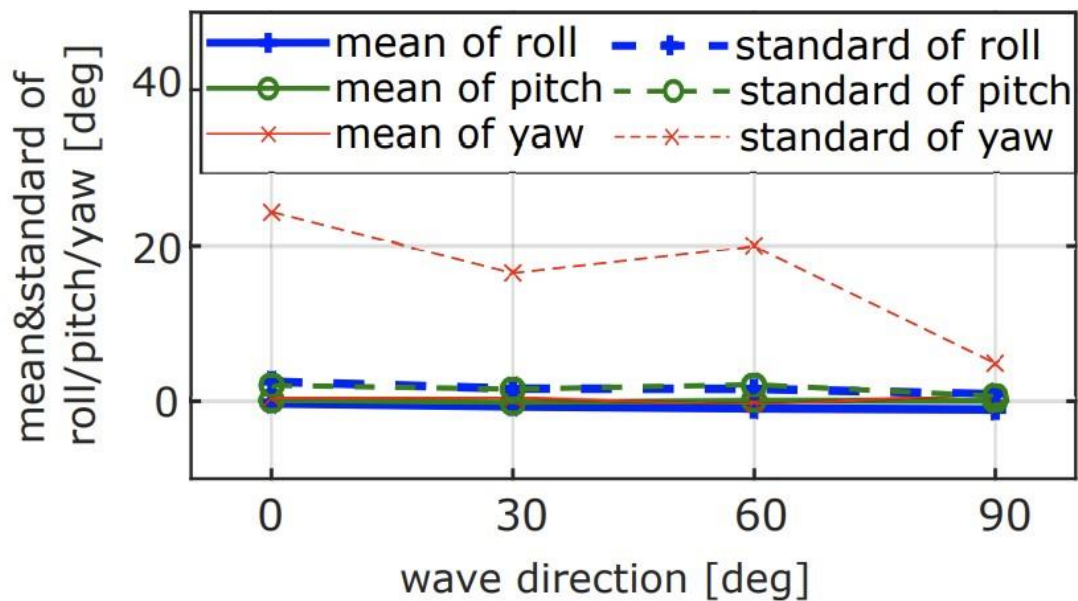Fig 4-1. Statistical characteristics of the original triangle TLP obtained by Zhu[50]

The present work aims to deepen the previous research by Zhu and Hu [50] to meet the demand for conductor safety. For this purpose, the FOPTS is re-designed. One of the critical points to be considered in the design is the TLP behaviour, characterized by the response amplitude operator (RAO). To avoid the weakness of a triangular platform in

suppressing the yaw displacement, a submerged TLP is adopted as the electric post referred to in the research by Zhao [39] and NREL [73]. The overview is shown in Fig 4-2. The floating foundation consists of four central columns to supply the buoyancy and steel beams to improve the structural stiffness. Fixed iron-ore-concrete ballasts, divided equally and placed at the base of the four central columns, are used to adjust the platform weight and the tendon pretension. A tubular steel tower involving a sheave-weight system is atop the central column and reserved to support the conductors.

The conductor wire $ACSR410mm^2$ is applied as the power conductor, whose rated tensile strength (RTS) of ACSR is 136KN for a Drake26/7 type. The everyday strength (EDS) [74], representing the tension of the conductor wire when the system is stationary, is set as 25% of the rated tensile strength (RTS) [74]. The 1st natural frequency (equivalent to the 1st out-of-plane frequency) can thus be calculated as 1.4 rad/s [75].

Fibre ropes, such as Dyneema ropes, are used for the mooring lines to satisfy the resistance requirement for saltwater and stable strength under bending. In this study, the conductor and the mooring line are considered linear elastic, and the elongation at 10% of the break strength (EBS) is regarded as the strength of the mooring line for proper operation.

A sheave is applied on the tower top as the tower-wire intermediate mechanism, as shown in Fig 4-2(a). The weight set strains the conductor wires that are restricted vertically and can move along the slideway. When the system is in operation, the mass of the weight set is calibrated by the motion of TLPs, so that conductor wire tension can be adjustable in responding to the wind and wave conditions.

(a)

conductor
(connected to other tower)

heave

surge

sway

tower

sheave

pulley

weight

water surface

center coulmn

steel beam

ballast tanks

tendons
(connected to anchor)

corner coulmn

(b)

Insulator

Conductor

θ_{wave}

θ_{wind}

**Wave
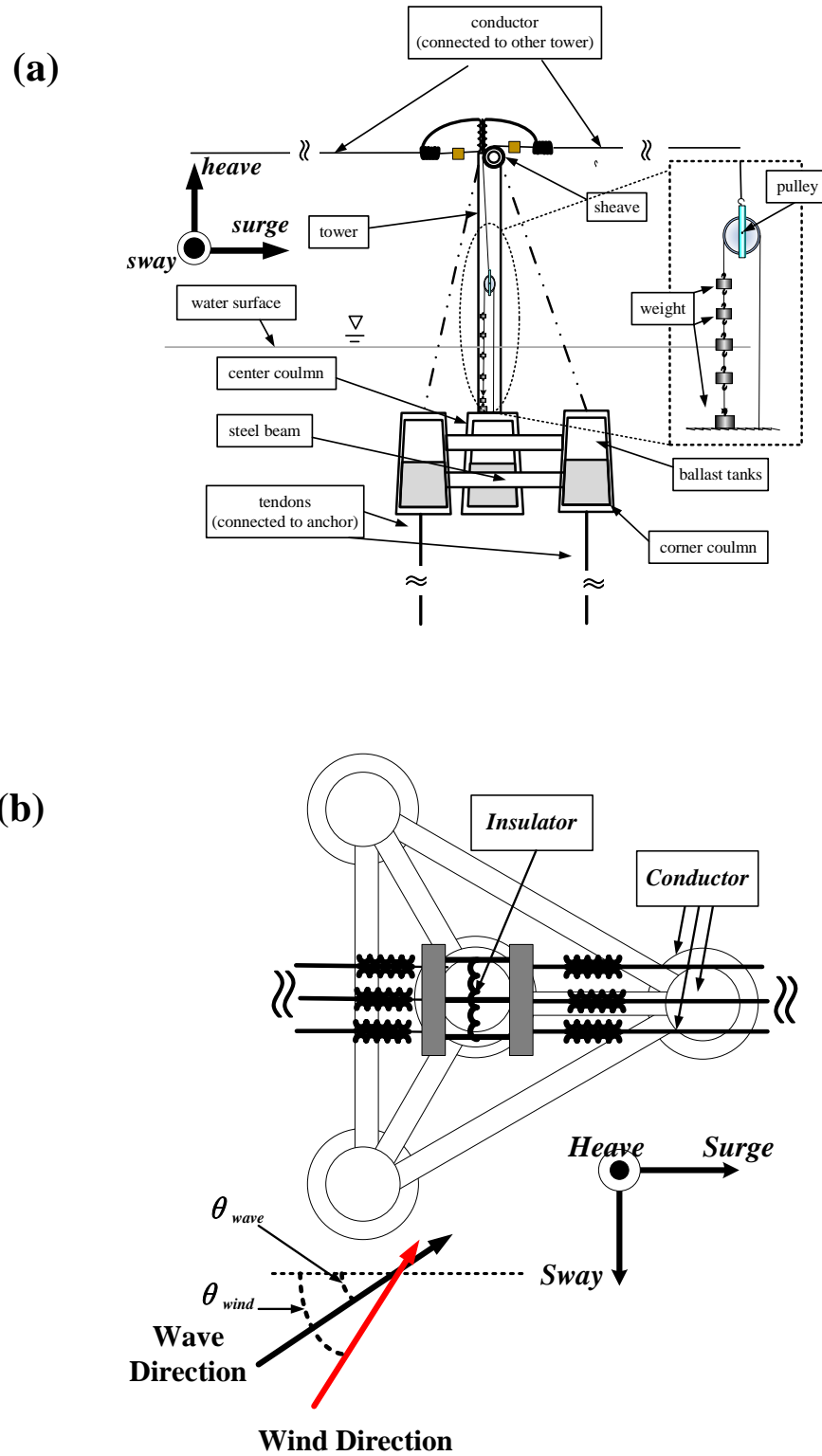Direction**

Wind Direction

Heave

Surge

Sway

Fig 4-2. An improved design of FOPTS: (a) side view; (b) top view.
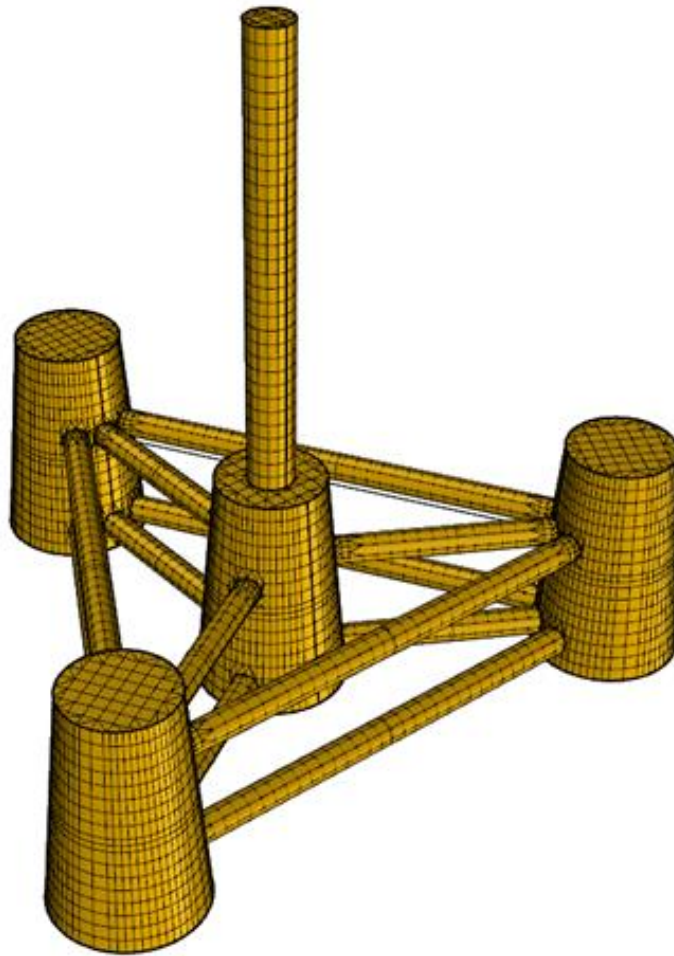
Fig 4-3. Surface mesh of the immersed part of the floating foundation for numerical simulation

4.2 An initial design of the TLP tower

TLP's parametric design is based on a frequency domain analysis [76-78].

In order to avoid resonance, we improved the design by using frequency domain analysis in practical working conditions. The natural frequency of the platform in heave, roll, and pitch should be designed in a high-frequency region, while the natural frequencies of the floating tower in the surge, sway, and yaw should be designed in a low-frequency level. The natural frequencies of TLP should satisfy:

$$
\begin{aligned}
(\omega_x, \omega_y, \omega_\psi) &\leq \omega_L \\
(\omega_z, \omega_\varphi, \omega_\theta) &\geq \omega_H
\end{aligned}
\tag{4-1}
$$

where x, y, ψ represent the motion in surge, sway and yaw, z, φ, θ represent the motion in heave, roll and pitch, respectively. $[\omega_L, \omega_H]$ is the expected range of environmental wave frequencies.

Design parameters of the TLP are determined by frequency analysis under extreme environmental conditions. Since the effect of the wire on the TLP tower is relatively small, the pretension of the wire T_0 should be satisfied as below according to the TLP properties:

$$
f_0 = \frac{\pi\sqrt{T_0/m_e}}{S_e} \geq \omega_H
\tag{4-2}
$$

The frequency domain in the design is shown in Fig 4-4.
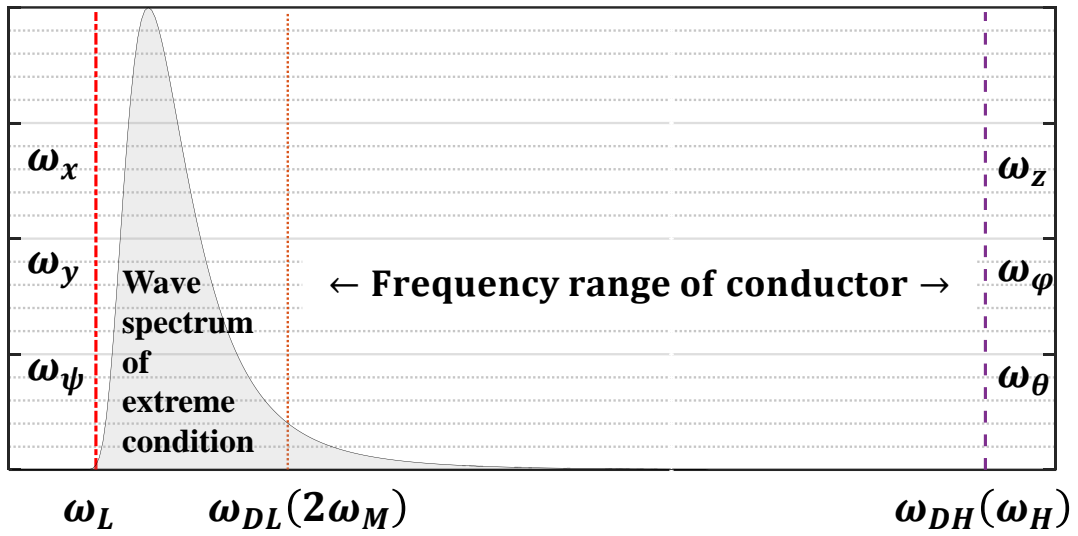
Fig 4-4. Frequency range considered in the design
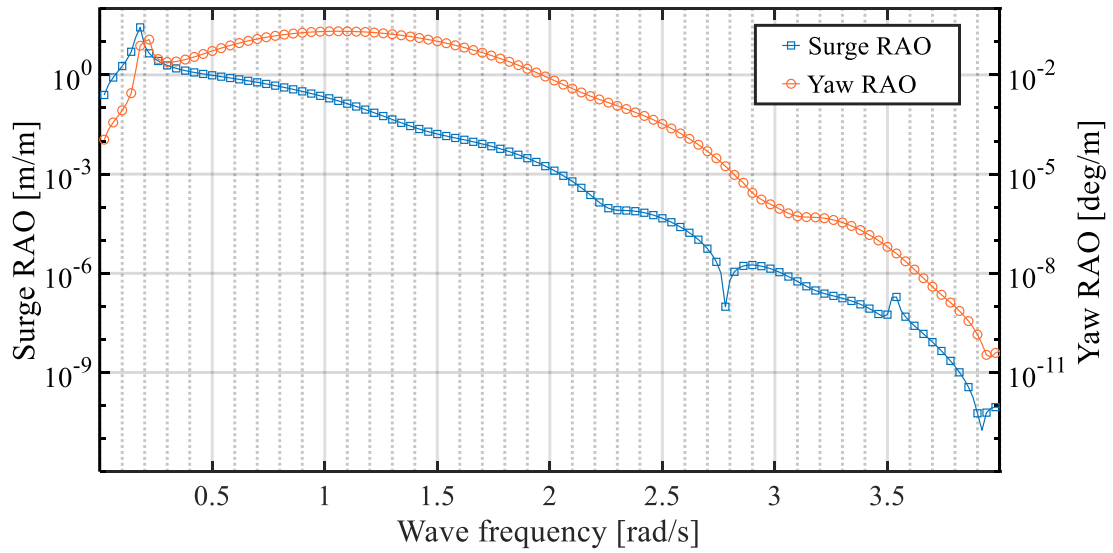
Fig 4-5. Motion RAOs of the floating tower in regular waves
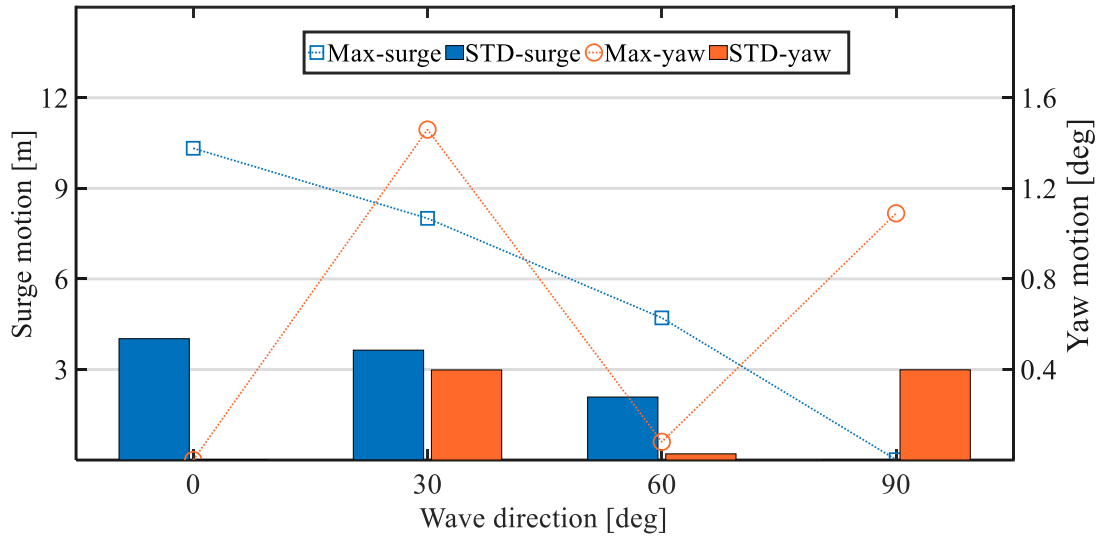
Fig 4-6. Hydrodynamic response under a harsh irregular wave condition: SWH=14 m; modal wave period (spectral peak period)=16 s

The RAOs in regular waves, essential indicators of the hydrodynamic performance of a floating platform, are presented in Fig 4-5. It is found that the yaw RAO of the TLP is always under $1^{\circ}/m$, suggesting a minor impact on the overhead conductor. Fig 4-6 shows the motion responses of the TLP in a severe wave condition. The maximum surge response falls below 15 m in correspondence to the irregular waves with a 14 m significant wave height (SWH), much smaller in contrast to the span of the conductor wires. The maximum yaw response is also within the design limit (5°) of a general floating wind turbine, being approximately 1.5°. These results prove that the designed TLP foundation performs satisfactorily in both regular and irregular wave conditions.

4.3 Sheave system for overhead conductor

A sheave is applied on the tower top as the tower-wire intermediate mechanism, as shown in Fig 4-7. The weight set is used to strain the conductor wires, and they are

restricted vertically and can move along the slideway. When the system is operating, the weight set's mass is considered to be adjustable by the motion of TLPs, so that the tension of the conductor wire can be modified in responding to the wind-wave condition.
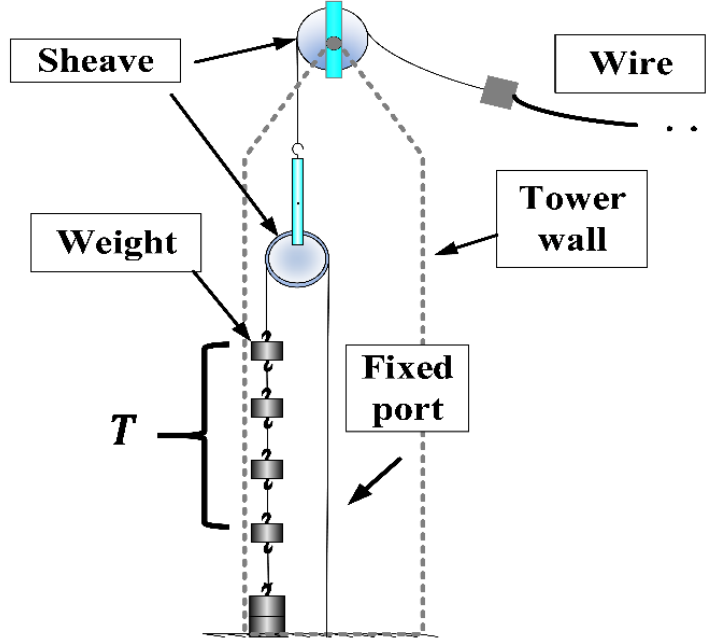
Fig 4-7. Sheave mechanism for conductor wires

Control laws for the weight T in the sheave mechanism are shown in Fig 4-8. The weight can be changed according to the offset H, which is caused by the interaction of the tower and wire. To make a contrast, control laws employed in the numerical study are set with the same limits $[T_{min}, T_{max}]$.

The weight $[T_{min}, T_{max}]$ could be calculated by:

$$T_{max} = T_0 \left(1 + \alpha_E \sqrt{\frac{m_E}{m_e}} \frac{R_M H_M \omega_M^2}{g} \right) < 2T_0$$

$$T_{min} = T_0 (1 - \alpha_E \sqrt{\frac{m_E}{m_e}} \frac{R_M H_M \omega_M^2}{g}) > 0 \tag{4-3}$$

$$\frac{T_{max}}{g} (g + R_M H_M \omega_M^2) \leq \frac{T_E}{\alpha_E}$$

where m_0 is the initial mass of weights when FOPTS remains stationary (at the stress of

EDS). ω_{ME} and H_{ME} is the modal wave frequency and the significant wave height of extreme conditions considered in the parametric design. α_E and β are safety factors. R_s is TLP's response amplitude operator (RAO) in surge-DOF, which can be obtained by:

$$R_M = \frac{|\Gamma(\omega_{ME})|}{\sqrt{(-\omega_{ME}^2 m + k)^2 + [\omega_M B(\omega_{ME})]^2}} \tag{4-4}$$

In the equation, $\Gamma(\omega_{ME})$ is the amplitude of wave load RAOs, $B(\omega_{ME})$ is the added hydro damping respected to the retardation function K mentioned in Section 3.1.
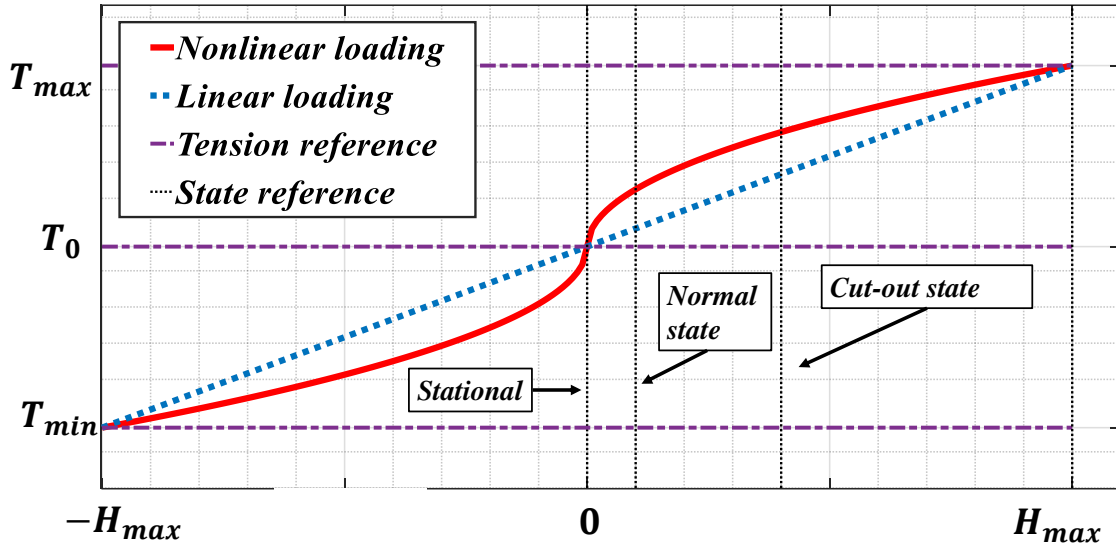
Fig 4-8. Fit curve of control laws in simulations [79], where weight mass T is mapped to its offset H ($H = 0$: position when the system is stationary, the reference state corresponds to $H = R_s H_s \omega_s^2$)

4.4 A design of FOPTS

The general properties of FOPTS are given in Table 4-1.

Table 4-1. FOPTS properties

Properties	Value
TLP	
Mass of TLP (tower + platform)	212 t
Ballast mass (fluid)	161 t
Displacement	620 m^3
Center of gravity (COG)	[0,0,-16.5] m
Inertia radius	[7.06,7.06,9.36] m
Side-length	20.8 m
Tower height	50 m
Air draft	35 m
Natural frequencies for 6 DoFs	[0.18,0.18,3.50,4.10,4.10,0.24] rad/s
Water depth	120 m
Mooring line	
Initial strain / Elongation at 10% Break strength (EBS)	0.2/0.55 (%) (Fiber rope)
Overhead conductors	
Conductor type	ACSR 240/410/610 mm^2 (Drake 26/7 type)
Rated tensile strength (RTS)	136 KN
Everyday strength(EDS)	25% RTS
Span	300 m
Stationary sag	4.9 m
1st natural frequency(stational)	1.4 rad/s

CHAPTER V

Wind tunnel experiment for FOPTS model

5.1 Introduction

A wind-tunnel experiment for comparison was performed at RIAM, Kyushu University. This experiment focuses on the conductor wire and mainly aims to validate the situation of the conductor wire under wind-wave conditions.

The TLP model (including the tower and the platform) is connected to a rigid port using springs to represent the mooring force. A motor is employed to simulate the wave-induced motion of TLP. With the aid of control circuits, the TLP is driven by simulative forces in sine waveforms to move harmonically around its balanced position. The driving force direction can be altered while the wind direction is kept constantly at 90°, thus creating conditions of wind-wave misalignment.

Hanging acrylic hollow pipes are used to represent the conductor wires in FOPTS. The pipe is hung by a nylon line, one end of which slides across the pulley. A micro load cell is attached to the nylon line to capture the line tension [80]. The tension increment exerted on the load cell will extend the strain gauges inside and can be measured as a voltage. Since the mass of the micro load cell is much smaller than the weight or pipe (less than $5g$), its impact on the system can be neglected.

Video cameras are used to track the pipe's motion to validate the aerodynamic model. The properties of the experimental setup are listed in Table 5-1. Note that the system damping is calculated from free decay test results and constantly employed in the numerical model.

(a)

(b)
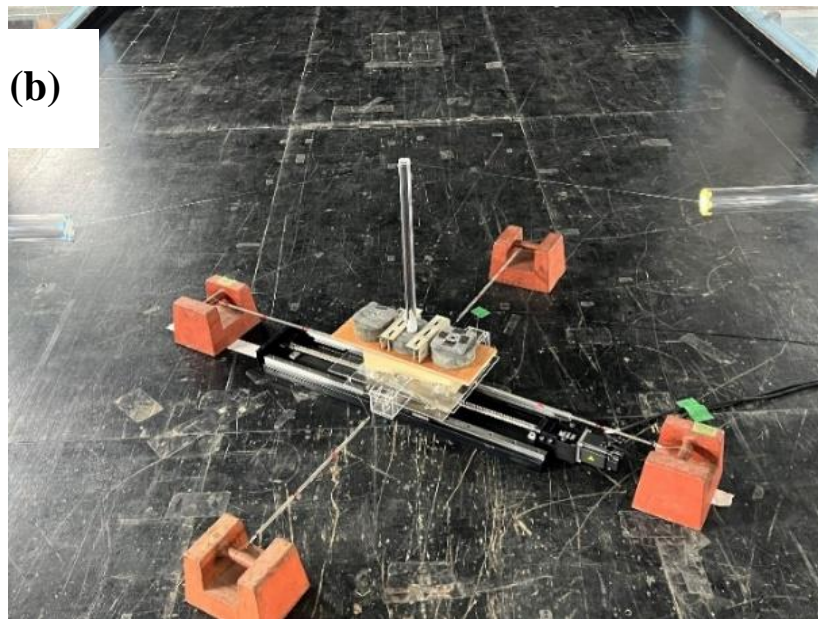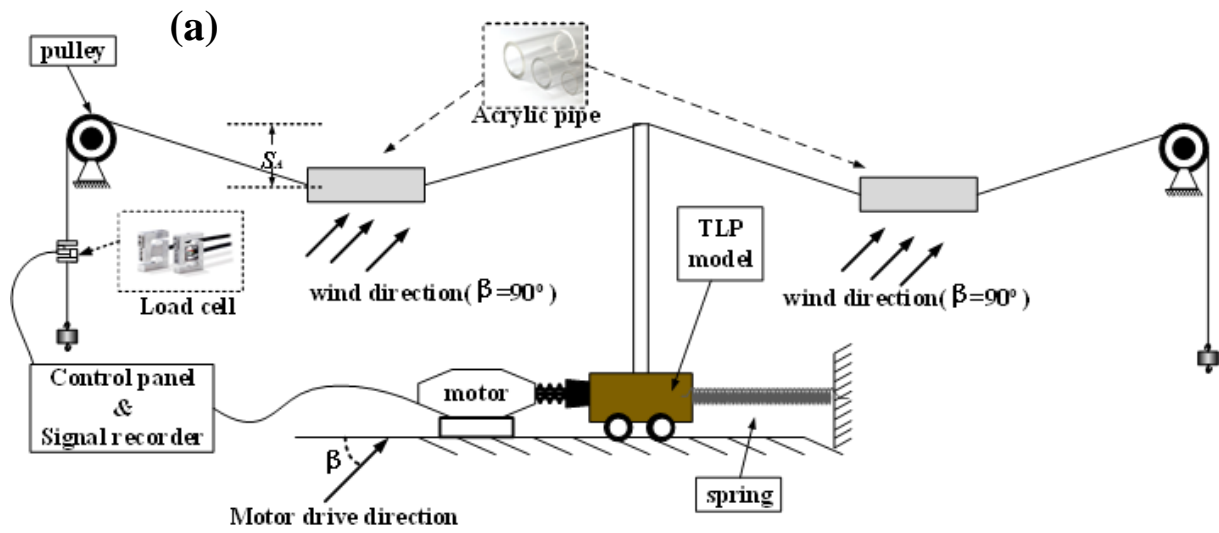
Fig 5-1. Experimental setup: (a) schematic view; (b) photograph in the wind tunnel

5.2 Experimental setup

In the experiment studies, the 1/35 scaled wind tunnel experiment aims to certify the conductor wire motion in hybrid wind-wave conditions. The TLP mass is set as $(M + A(\infty))$ to include the added mass in water. The spring that connects to the TLP is used to imitate the mooing equivalent stiffness in surge DoF. Since the entire model system is restricted to moving translationally, the rotation motions are negligible.

The natural period of the first vibration mode of a stationary conductor model (acrylic hollow pipe) can be obtained by [75,81]:

$$T_{1st} = 2\pi \sqrt{\frac{S_A}{g}} \qquad (5\text{-}1)$$

where S_A is the sag of an acrylic pipe, g is the gravitational acceleration. The 1st out-of-plane frequency of the acrylic pipe can be made in line with that of the prototype by adjusting its EDS.

The natural frequency of acrylic pipe is normalized using Froude's similarity to study the interaction between the conductor and the tower. The tower motion and the wind speed applied in the experiment are based on the data of the real sea environment, as given in Table 5-2.

Table 5-1. Properties of the experimental setup

	Prototype	Exp model
Mass of platform (added mass included)	720 t	16.5kg
Equivalent mooring stiffness K_{surge}	24600N/m	20N/m
Span	300m	2m
Operation wind speed	3-30m/s	1-10m/s
θ_{mis}		30°/90°
1st natural frequency of conductor	1.4 rad/s	8.5 rad/s
Froude number ($1/F_r$)	1	1/35
Systemic damping		3%(by test)

Table 5-2. Experimental conditions (Froude similarity: $A_{\mathrm{exp}} = A_{\mathrm{pro}}/F_r$, $T_{\mathrm{exp}} = T_{\mathrm{pro}}/\sqrt{F_r}$)

Case	Motion amplitude of TLP model (A_{exp})	Wave period in EXP(T_{exp})	Offshore situation
1	9.5 cm	2.20 s	Harsh
2	6.0 cm	1.85 s	Very rough
3	4.5 cm	1.55 s	Rough
4	2.5 cm	1.26 s	Rough
5	2.0 cm	1.18 s	Moderate
6	1.0 cm	1.00 s	Moderate

5.3 Comparison between numerical simulation and experiment

The statistical characteristics of the wire tension obtained from the experiments and simulations are shown in Fig 5-4. Different levels of EDS are considered in validating the lumped-mass model.

Fig 5-2. Conductor model with acrylic pipe for the wind tunnel experiment

As shown in Fig 5-4(a) and 5-4(b), the deviations in most cases are less than 10%, indicating a good agreement. When the conductor reaches a double natural period (i.e., half the natural frequency), subharmonic resonance plays a dominant role in the conductor's motion. Especially in the case of low EDS, the conductor has a violent vibration under moderate environments, which is dangerous in engineering practices. In general, at an extended period, the wire motion is mainly driven by the tower motion, whereas at a short period, the wires are close to subharmonic resonances. When the

frequency of the excitation load exerted on the tower reaches half of the wire's natural frequency, subharmonic resonances will happen.

Moreover, it is worth noting that Fig 5-4(c), which represents 170% EDS of the prototype, exhibits more significant deviations between the experiment data and the simulation results. The rapid variations of the nylon line damping in the presence of a larger EDS may cause this. In contrast, the numerical simulation employs a constant damping ratio in modelling. It is found that increasing EDS leads to a decrease in the impact of subharmonic resonances [82-83]. Under such a circumstance, the wire motion driven by the tower motion takes the dominant role.
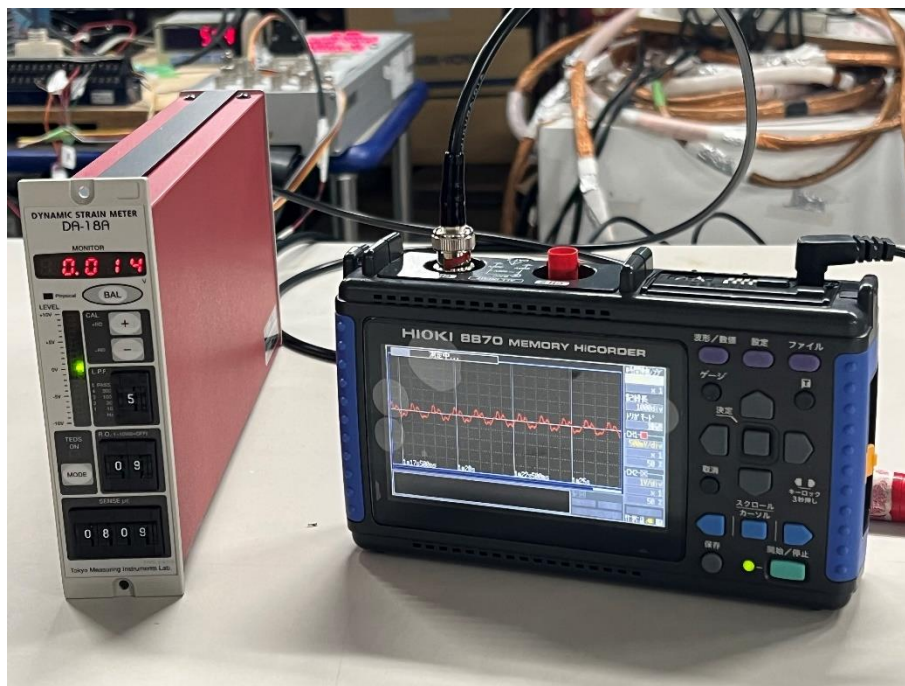
Fig 5-3. Signal recorder for the load cell

We also validate the numerical model by comparing the motion of the conductor. This validation can indicate the accuracy of the aerodynamic model. Fig 5-5 depicts the motion of the conductor model in the experiment. Similar to the results in Fig 5-4, the

deviations are generally less than 15%, except at the subharmonic resonance region. For high wind speeds, the error of the wake oscillation model shows a significant effect on simulation, wherein the deviation can reach 20%. This is probably due to that in the wake oscillation model. A constant parameter may not be sufficiently accurate at a high wind speed. In Fig 5-5(d), the simulation exhibits a more significant difference when the wave period approaches the subharmonic resonance region owing to the linear elasticity of the nylon line.
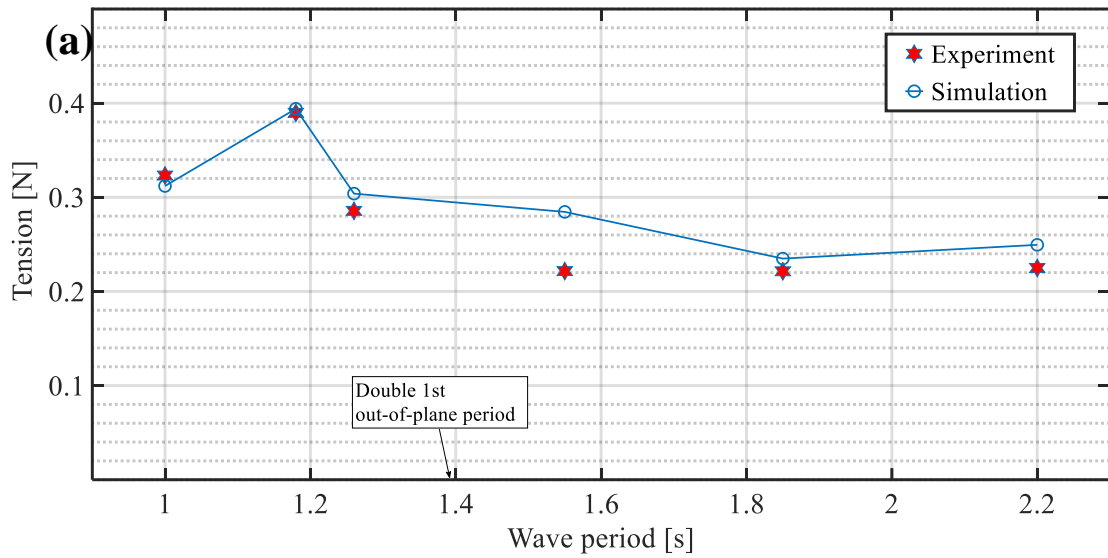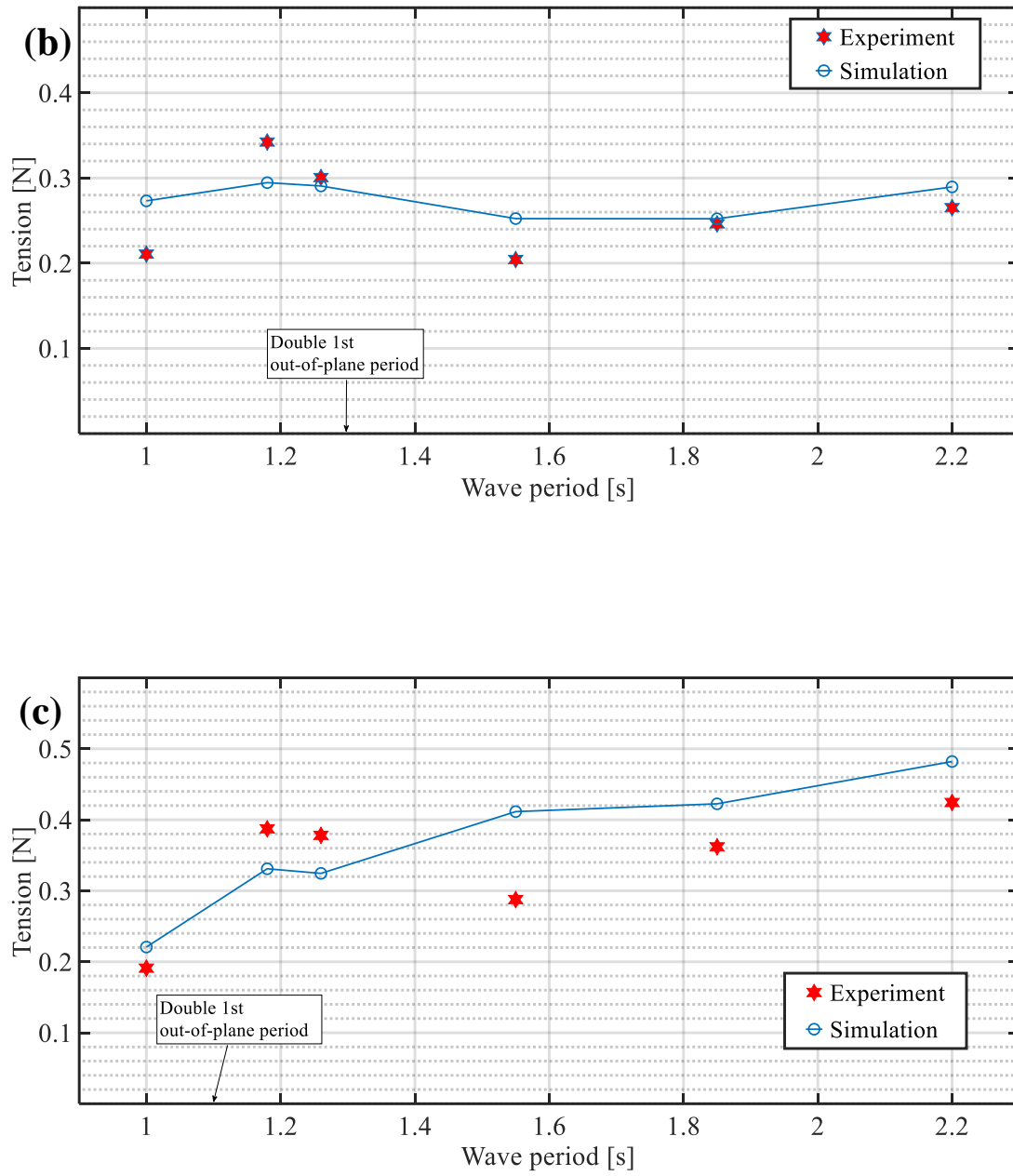
Fig 5-4. Comparison of conductor tension under different EDS: (a) $T_{1st} = 0.7s$, 0.7 EDS; (b) $T_{1st} = 0.65s$, 1.0 EDS; (c) $T_{1st} = 0.55s$, 1.7 EDS.

(a)

(b)
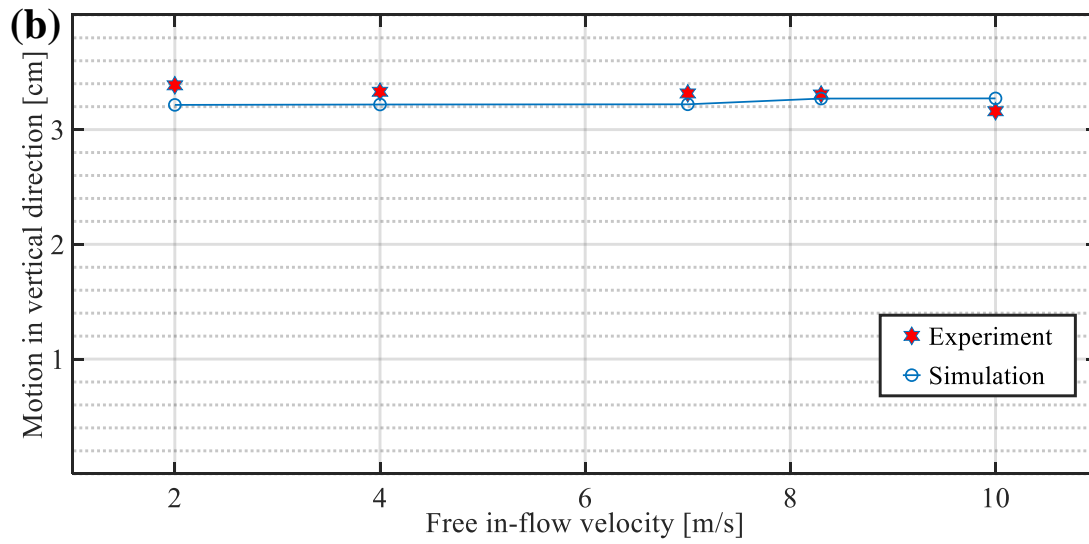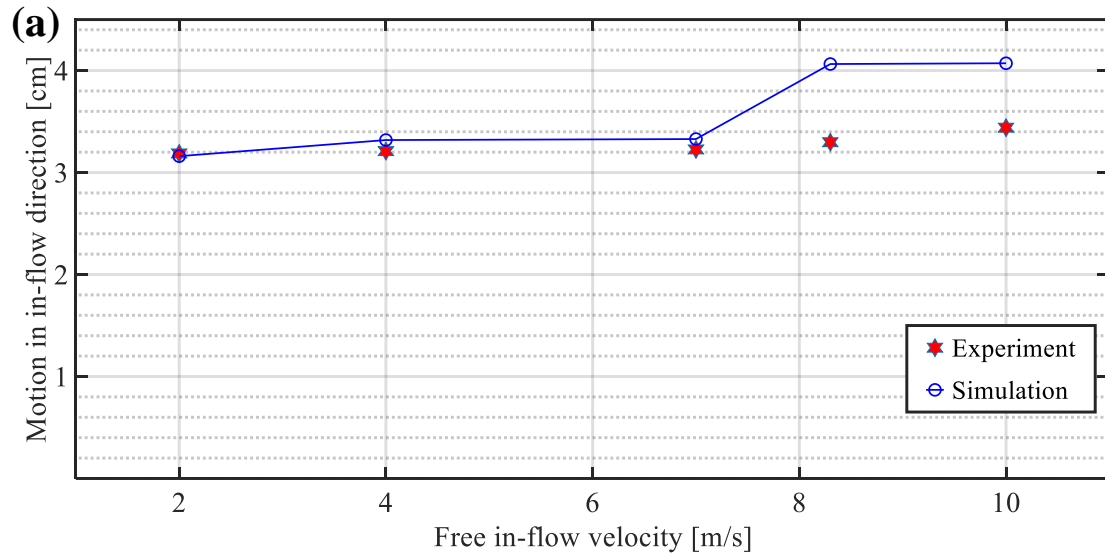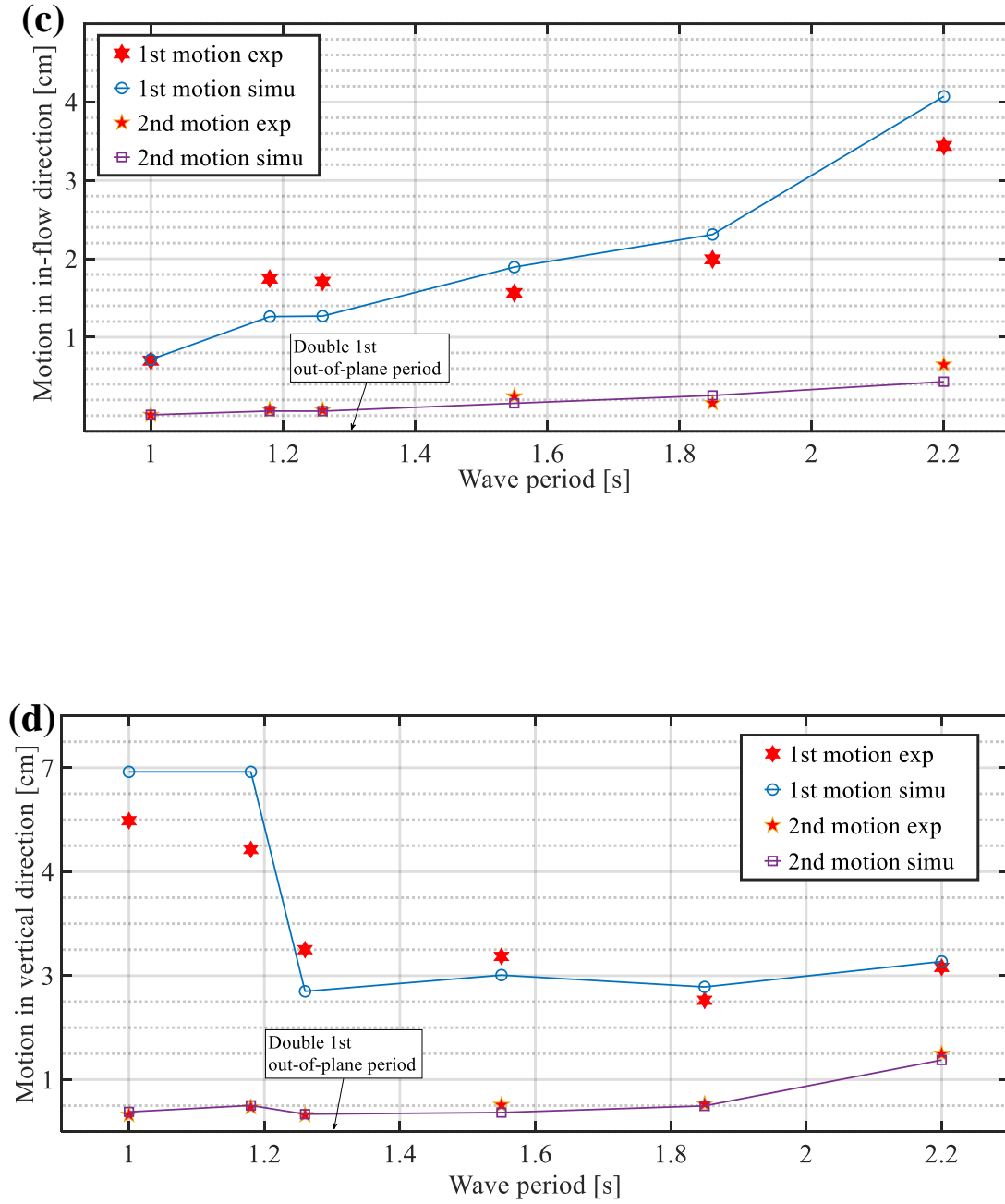
Fig 5-5. Comparison of conductor motion: (a) $T = 2.1s$, in-flow direction; (b) $T = 2.1s$, vertical direction; (c) by wave period, in-flow direction; (d) by wave period, vertical direction.

5.4 Conclusion

Major conclusions from the experimental study are as follows:

(a) The numerical simulation agrees well with the experiment. It is shown that the main factors affecting the accuracy of the present numerical model are the system damping and the nonlinear elastic property.

(b) EDS has a remarkable effect on the conductor's motion. A low EDS may induce significant subharmonic resonance in moderate sea environments. A suitable EDS should be selected for FOPTS in the system design.

(c) The wind speed would affect the accuracy of the aerodynamic model (wake oscillation model) (Reynold Number). When the wind speed is over 8m/s, the motion of the conductor shows a markable deviation from the experiment result.

(d) The result of conductor tension and motion are validated with the numerical model and reaches a good agreement, proving the reliability of the aerodynamic module introduced in Section 2.5.

CHAPTER VI

Numerical investigation of FOPTS

6.1 Introduction

In this chapter, a comprehensive numerical simulation is performed to investigate FOPTS response to the wind-wave environment. Section 6.5.1 will discuss conductor safety in view of tension, and navigational safety will be illustrated in Section 6.5.2. The safety of the mooring line is investigated in Section 6.5.3. For reference of accuracy, the effect of second wave force in the numerical model will be discussed in Section 6.6.

6.2 Environmental conditions
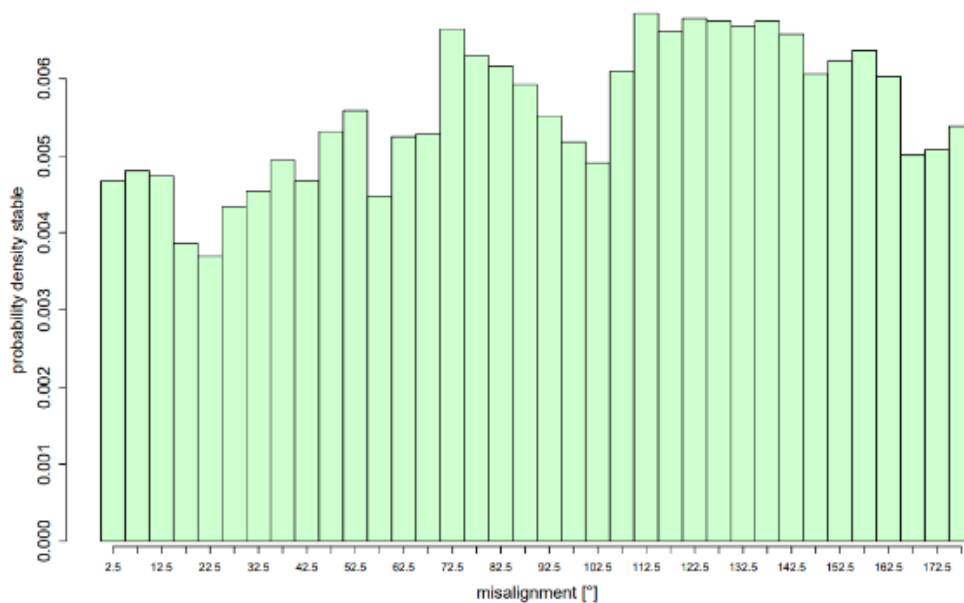
(a) stable
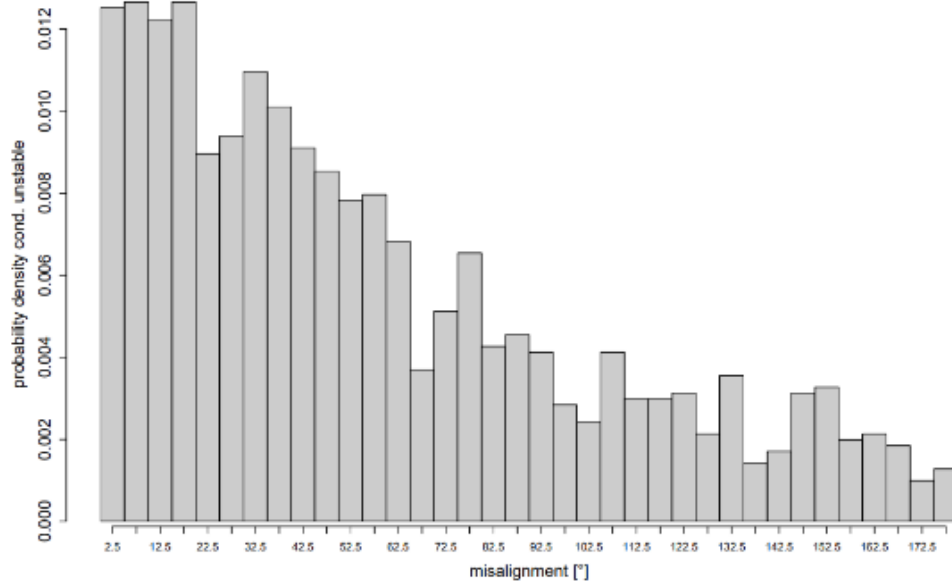
(b) conditional unstable
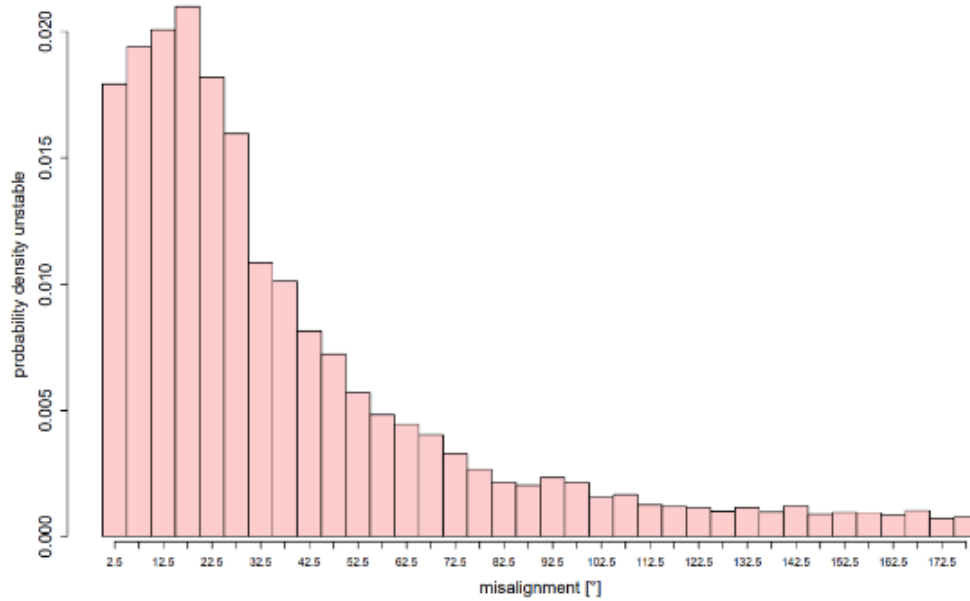
(c) unstable

Fig 6-1. Probability density distribution with the wind-wave misalignment angle θ_{mis} under different atmospheric conditions [85]

As common in real offshore environments, wind-wave misalignment is an important factor in the simulation of marine structures. The misalignment angle θ_{mis} depends on the stability of atmospheric boundary layers and is defined by:

$$\theta_{mis} = |\theta_{wave} - \theta_{wind}|. \tag{6-1}$$

As shown in Table 6-1, under the stable condition corresponding to sea levels 0-5, the probability of wind-wave misalignment is almost equally distributed due to decoupled wind layers, like the situation shown in Fig 6-1(a). Accordingly, the misalignment under unstable conditions highly depends on wave directions because of the turbulence in the air.

Table 6-1. Atmospheric conditions for different sea states

Sea state	Wind speed	Average SWH	Atmospheric condition (most probable)	Wind turbulence intensity
~5	$0{\sim}16 \, m/s$	$0{\sim}5 \, m$	stable	$\geq 15\%$
5~8	$16{\sim}30 \, m/s$	$5{\sim}10m$	conditional stable	$10{\sim}20\%$
8~	$\geq 30m/s$	$\geq 10m$	unstable	$\leq 10\%$

Turbulence is also essential in evaluating wind-induced cable damage [86-87]. This study also considers the turbulence intensity (TI) for random aerodynamic loads on conductor wires. The turbulence intensity is defined as the ratio of the standard deviation of wind speed to the mean wind speed:

$$TI = \frac{U_\sigma}{\overline{U}} \tag{6-2}$$

where U_σ is the standard deviation of the wind speed series, $\overline{U}$ is the mean wind speed.

A noise generator is applied to generate normally distributed random signals for the fluctuations of wind speed in turbulent conditions. The averaging power spectral density (APSD) can be defined as:

$$APSD = TI * \bar{U} * t_c \tag{6-3}$$

where t_c is the sample time of the random number generator.
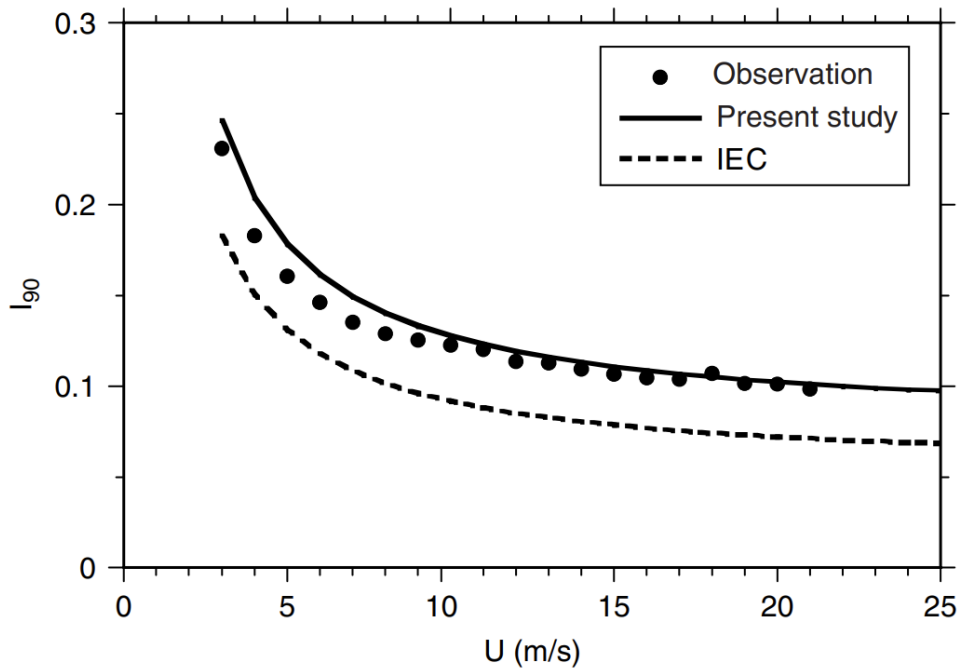
Fig 6-2. Variation of turbulence intensity with offshore wind speed (Location: Naraha-machi, Fukushima Prefecture) [91]

The FOPTS is assumed to be installed at a moderate water depth of 120m, and the environmental conditions are referred to in the meteorological data of the East Japan Sea [52,88-90]. The environmental condition for simulations is shown in Table 6-2. According to the definition of cut-out speed, the wind farm is assumed to work while the wind speed is below 25m/s, corresponding to LC 1, 2 and 3. It is known that the wind-wave misalignment angle θ_{mis} is small under typhoons [92].

Table 6-2. Environmental conditions for numerical simulation

Load Case	SWH/Period	Wind speed(T.I.)[93]	θ_{mis}	Operation status of wind farm
1	0.75 m/6 s	6 m/s (35%)	$0° - 90°$	Operation (normal)
2	3.5 m/8 s	12 m/s (25%)	$0° - 90°$	Operation (maximum output)
3	8 m/11 s	25 m/s (20%)	$0° - 60°$	Cut-out
4	14 m/16 s	50 m/s (10%)	$0° - 30°$	Blocked

6.3 FOPTS properties

The aluminium conductor steel-reinforced cable (ACSR) is employed as the overhead conductor, a type of high-capacity, high-strength stranded conductor typically used in overhead power lines. High-purity aluminium is chosen as outer strands for its good conductivity, low weight, low cost, resistance to corrosion and decent mechanical stress resistance. The centre strand is made of steel to help support the weight of the conductor with additional strength. Steel is of higher strength than aluminium, allowing for increased mechanical tension to be applied to the conductor. Steel also has lower elastic and inelastic deformation (permanent elongation) due to mechanical loading (e.g., wind and ice) as well as a lower coefficient of thermal expansion under current loading.

By using the proposed numerical model, numerical studies have been carried out on the system reliability of FOPTS against actual sea environments. A FOPTS is designed for the numerical simulation, as shown in Fig 6-4, including conductors, towers, and substations. The following discussions are based on time-domain simulations.

The properties of FOPTS system can be referenced in section 4.4, and the

properties of different ACSR types are shown as Table 6-3. Definitely ACSR 610mm^2 has a smaller electrical resistance and brings the highest conductivity efficiency among three ACSR.

Table 6-3. Properties of ACSR conductors (Drake 26/7 type)[94]

Conductor type	RTS	Young's modulus	Unit mass	Electrical resistance	Outer diameter
ACSR 240mm^2	99.5 KN	89.1 Gpa	1151 kg/km	0.120 Ω/km	2 cm
ACSR 410mm^2	136.0 KN	82.0 Gpa	1734 kg/km	0.088 Ω/km	2.7 cm
ACSR 610mm^2	180 KN	78.3 Gpa	2436 kg/km	0.044 Ω/km	3.1cm
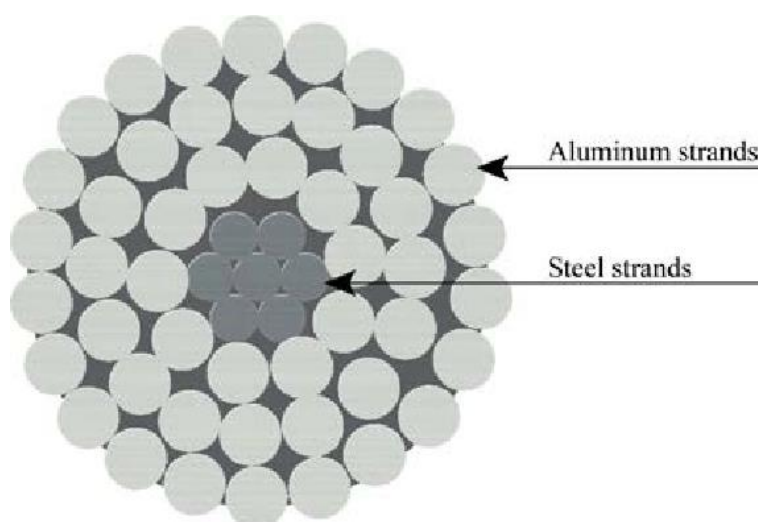
Fig 6-3. Cross section of Drake 26/7 conductor[94]
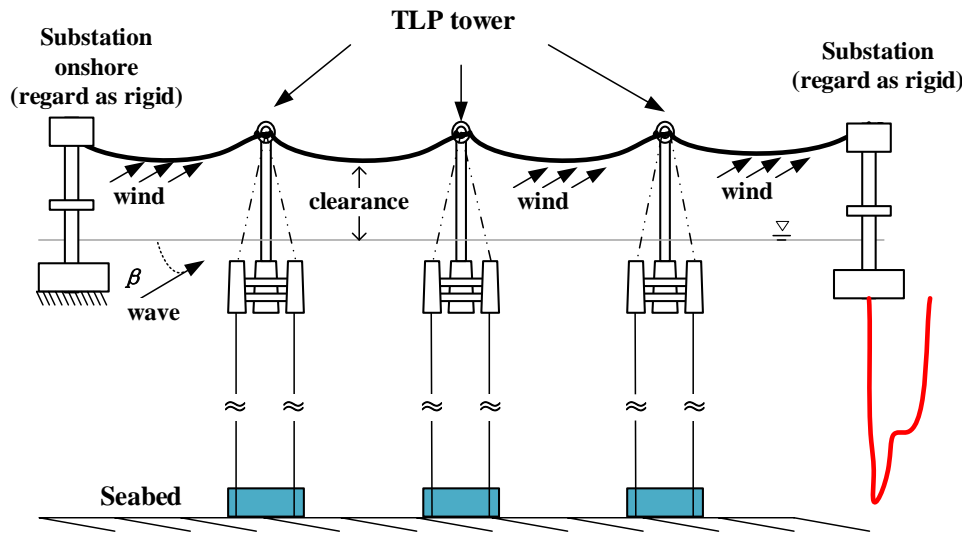
Fig 6-4. FOPTS designed for numerical simulation

6.4 Numerical investigation on wind-only condition

Numerical simulations are conducted to assess the stability of the overhead conductor in turbulent wind environments. In a perpendicular wind inflow, a conductor will have a maximum sag. The conductor will become unstable if it is made of light materials or has a slight pretension. For this reason, a perpendicular wind inflow is selected to check the stability of the conductor in the present study. Three types of ACSR are discussed, and the 1st natural frequency is set as $1.4\ rad/s$ for comparison (same in Section 6.5).
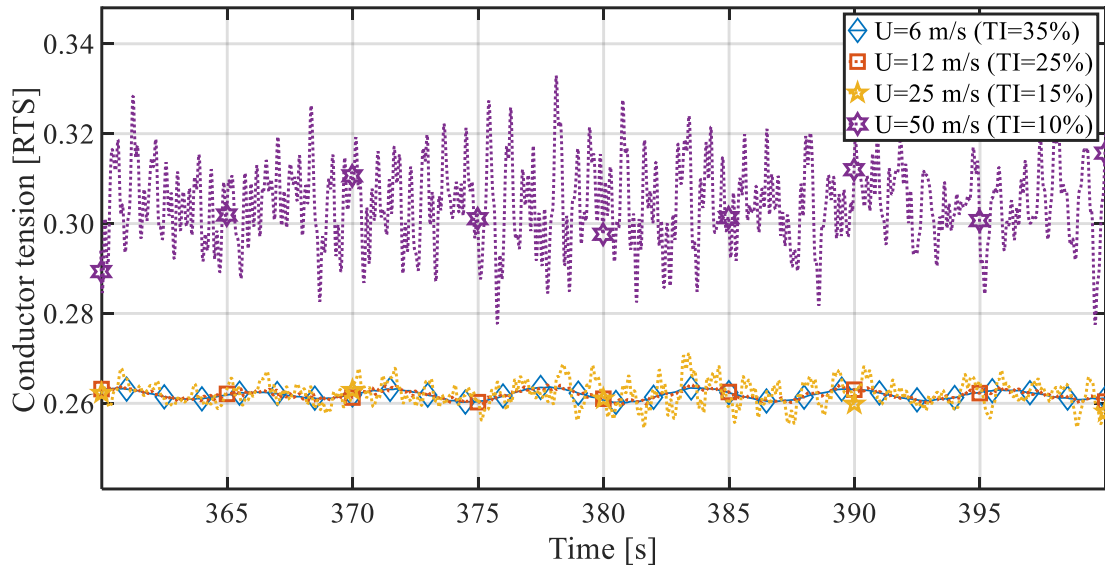
Fig 6-5. Time series of the $ACSR410mm^2$ tension under wind only conditions
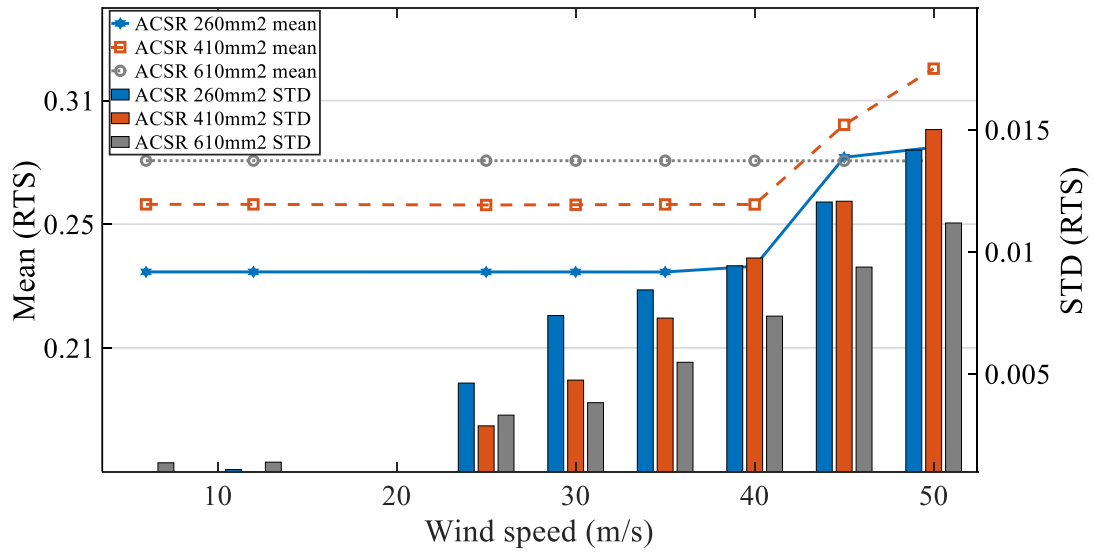
Fig 6-6. Conductor tension under wind only conditions ($\beta_{wind} = 90°$,

$ACSR240mm^2, ACSR410mm^2, ACSR610mm^2$)

The tensions of the conductor ($ACSR410mm^2$) under various wind conditions are shown in Fig 6-5 by turning off the wave conditions. The mean tension of the conductor is found to be insensitive to the turbulent wind when wind speed is below 40m/s, indicating a weak correlation between θ_{wind} and the conductor tension. However, when the wind speed increases to 50m/s, the mean tension shows an 18% rise, and the STD increases to 1.5% RTS. From these results, it can be concluded that the overhead conductor of the FOPTS is stable in most offshore environments.

Fig 6-6 presents a statistical analysis of the time series for three types of ACSR. ACSR 610mm^2, with the most enormous unit mass, has less STD to the turbulent wind. ACSR 240mm^2, which always shows the largest tension STD, indicates a weak adaption to strong wind.

6.5 Numerical investigation on coupled wind-wave condition

6.5.1 Conductor force

Two metrics can measure the safety of conductor wires when FOPTS is in operation. One is the fatigue performance [95-97] under daily conditions (i.e., LC 1 and 2 in Table 5), which is essential to evaluate the lifetime of conductors. The other is the stress under harsh environments (i.e., LC 3 and 4), which indicates the system's response to emergencies.

Fig 6-7. Conductor force under LC 1 and 2 (ASCR 410mm^2, $\theta_{wave} = 0°, \theta_{wind} = 10°$)
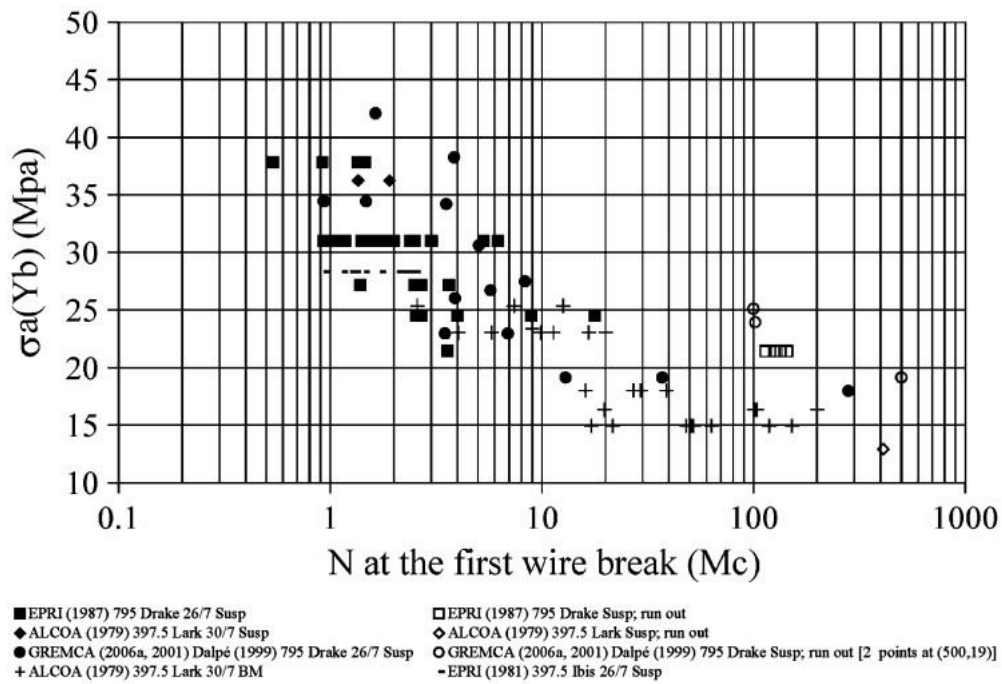
Fig 6-8. Fatigue tests data of two-layer ACSR.[96]
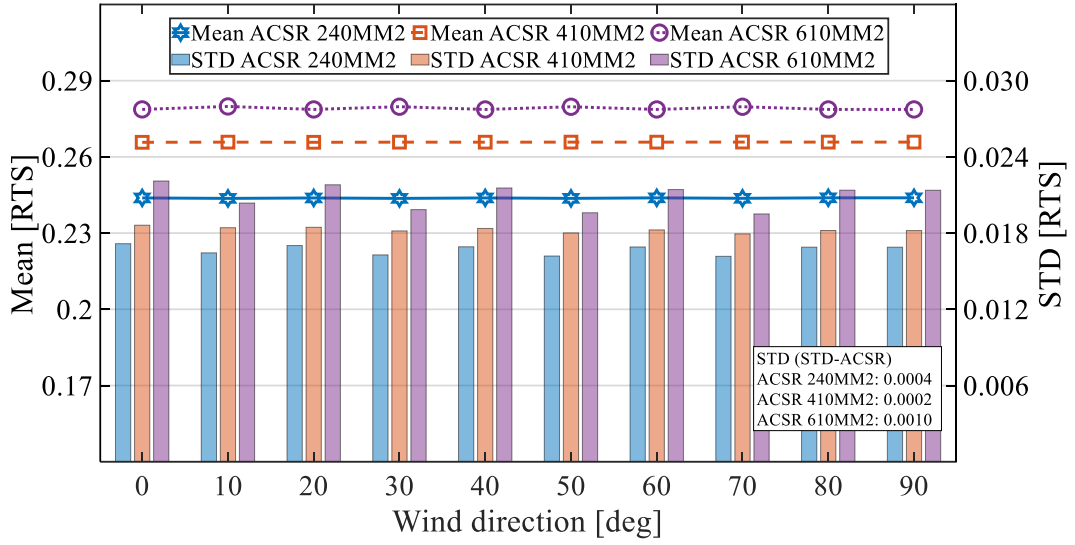
Fig 6-9. Conductor tension under different θ_{wind} ($\theta_{wave} = 60°$, LC 2)
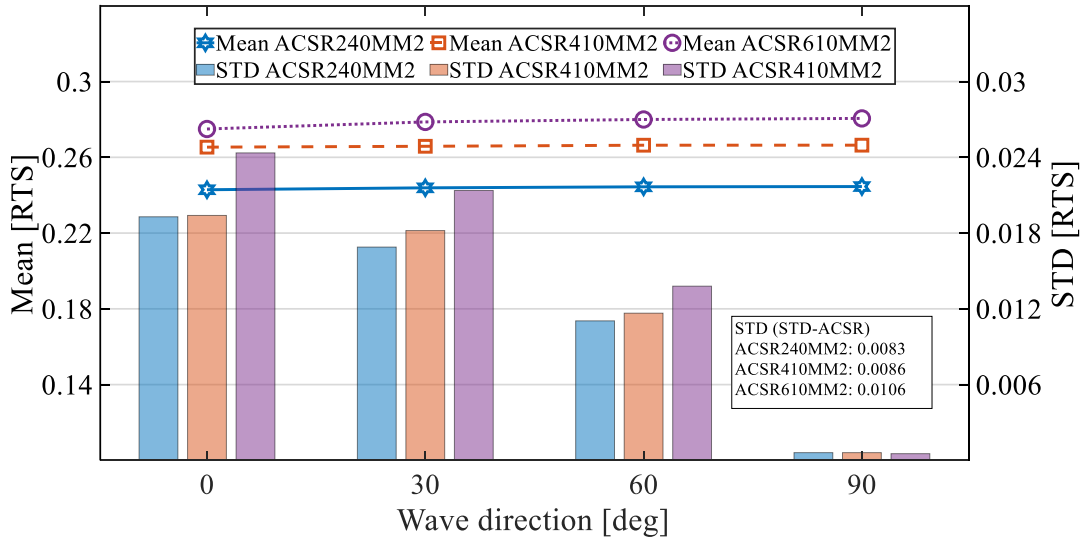
Fig 6-10. Conductor tension under different θ_{wave} ($\theta_{wind} = 30°$, LC 2)

6.5.1.1 Mild environment
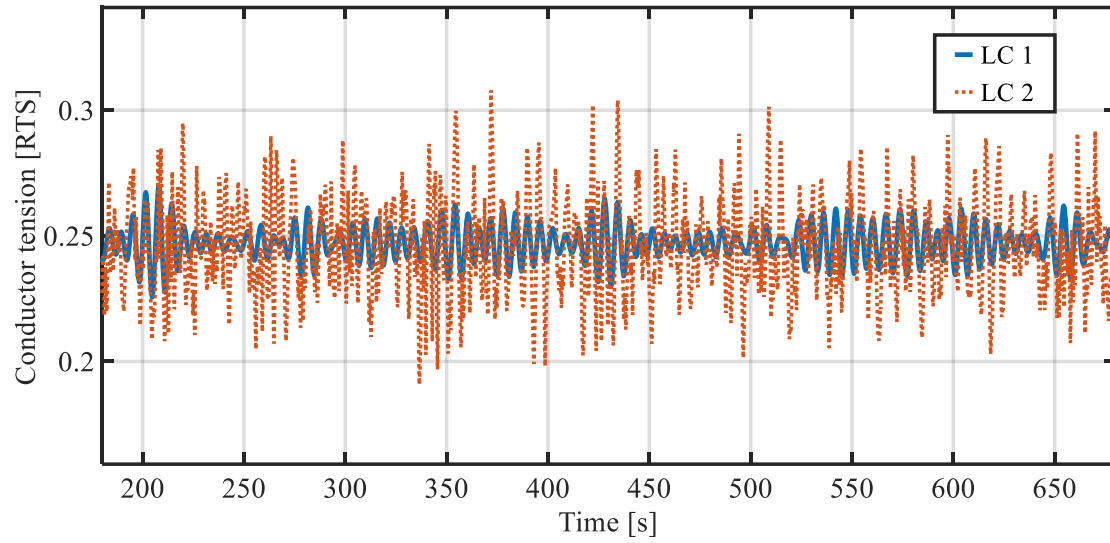
The time series of stress under LC 1 and 2 are plotted in Fig 6-7. The conductor can work within a limit of 30% RTS under daily conditions. The standard division (STD) of conductor force is calculated to check the fatigue performance evaluation. Based on the S-N curve of the Drake 26/7 conductor (shown as Fig 6-8), the conductor would break at an over-100 million-cycle under 15 Mpa stress amplitude, corresponding to a lifetime of :

$$T_{life} > 100 * T_s \approx 19.2 \ (year). \hspace{2cm} (6\text{-}4)$$

where T_s is the the average period of the cycle load.

The difference between the three types is plotted in Fig 6-9 and Fig 6-10. From the effect of wind direction plotted in Fig 6-9, the tension STD of ACSR 410mm^2 is found to be the smallest variation to the change in wind direction.

As shown in Fig 6-10, wave direction significantly affects the conductor tension. Comparing other ACSR types, ACSR 610mm^2 especially shows a violent STD wave direction change, indicating a shorter lifetime according to the S-N analysis.

6.5.1.2 Harsh environment

The stress in harsh environments (LC 3 and 4) can also be discussed considering the wind-wave misalignment. A time series of conductor force is shown in Fig 6-11. The conductor force would be limited to 55% RTS in all simulations, which remains enough tolerance for sudden loads. The low bound of conductor force, which is close to 5% RTS, should also be noticed for the instability of long-span cable. When wind/wave flows along the direction of 90°, the conductor force can also reach 33% RTS with a low STD by the effect of strong winds.
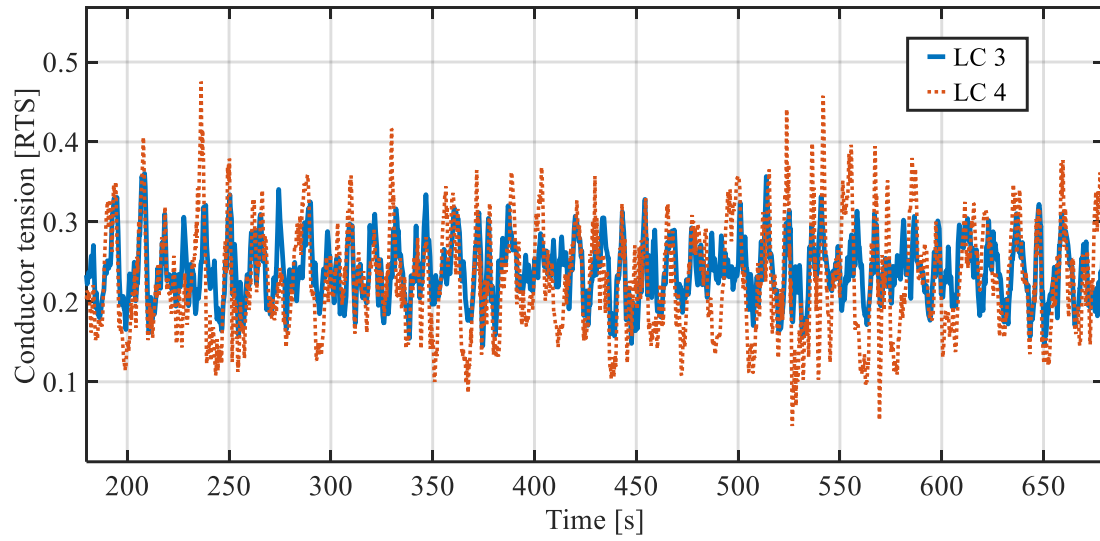
Fig 6-11. Conductor force under LC 3 and 4(ASCR 410mm^2,$\theta_{wave} = 0°$, $\theta_{wind} = 10°$)

Table 6-4. Upper and low bound of conductor force (ASCR 410mm^2, LC 4)

|	$\theta_{wave} = 0°$, $\theta_{wind} = 30°$	$\theta_{wave} = 30°$, $\theta_{wind} = 0°$	$\theta_{wave} = 60°$, $\theta_{wind} = 90°$	$\theta_{wave} = 90°$, $\theta_{wind} = 90°$
Max/Min (RTS)	0.51/0.04	0.48/0.03	0.39/0.18	0.33/0.25
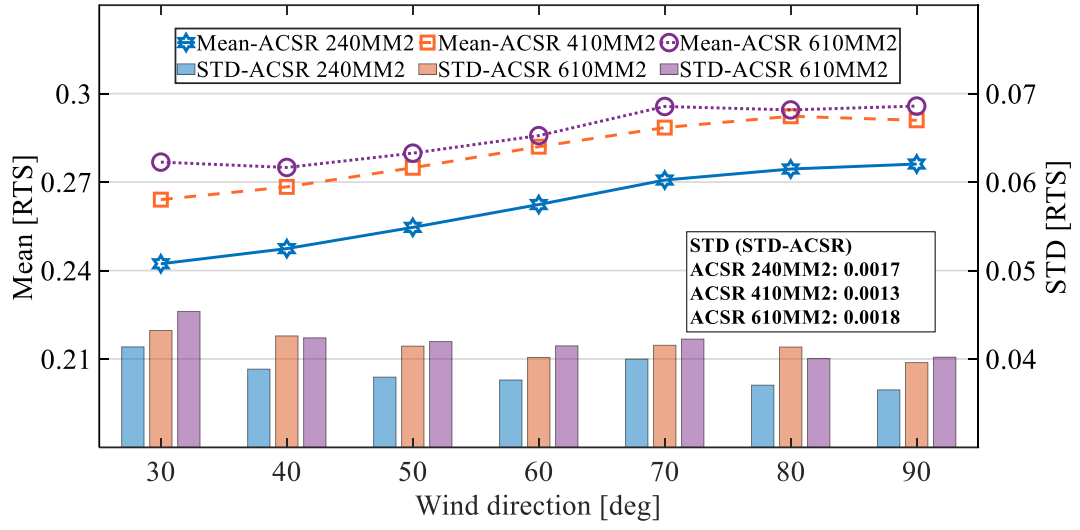
Fig 6-12. Conductor tension under different θ_{wind} ($\theta_{wave} = 60°$, LC 4)
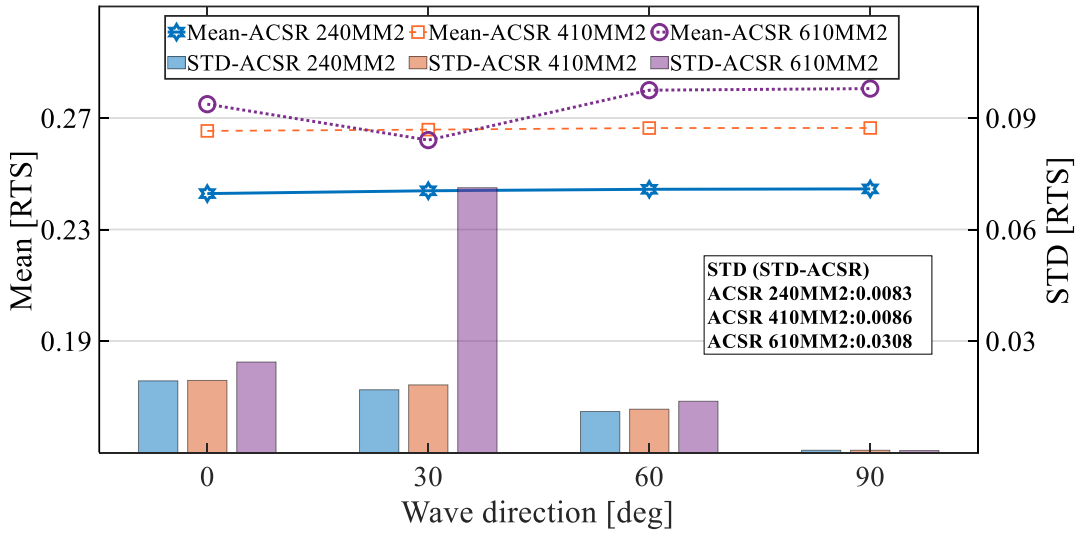
Fig 6-13. Conductor tension under different θ_{wave} ($\theta_{wind} = 30°$, LC 4)

Fig 6-12 illustrates the effect of wind direction on the wire tension under the same wave conditions. It is found that the mean wire tension increases with the wind direction angle θ_{wind}. However, the increment is small due to the presence of the pulleys. In contrast, the standard deviation of the wire tension decreases with the increase of the wind speed U, possibly due to the reason that wires are stretched and highly tensioned at high wind speeds. Note that the standard deviation of the wire tension significantly decreases in hybrid wind and wave conditions when the misalignment angle is zero ($\theta_{wave} = \theta_{wind} = 60°$).

Fig 6-13 illustrates the effect of wave direction on the wire tension when the wind speed keeps constant. When waves incident along the platform sway direction ($\theta_{wave} = 90°$), the standard deviation of the wire tension becomes zero, and the tower motion has little effect on the conductor wires. Similarly, due to the presence of the pulleys, the mean wire tension in extreme conditions is less affected by the combined wind and waves.

Similar to the result in Section 6.5.1.1, ACSR 610mm^2 shows a larger STD in the statistical analysis. Especially when the wave direction θ_{wave} turns to 30°, the STD shows a sudden rise, which may lead to a dangerous situation in extreme environments such as storms or typhoons.

6.5.2 On navigational safety

Conductor clearance to the water surface is studied because of its effect on the electric-field distribution [98-99]. The conductor wire should be kept above the reference height in view of electromagnetism while operating. The sailing area under the conductor,

assumed to be possibly affected by the electric field from the high-voltage conductor, is denoted as the shadow area in Fig 6-14.
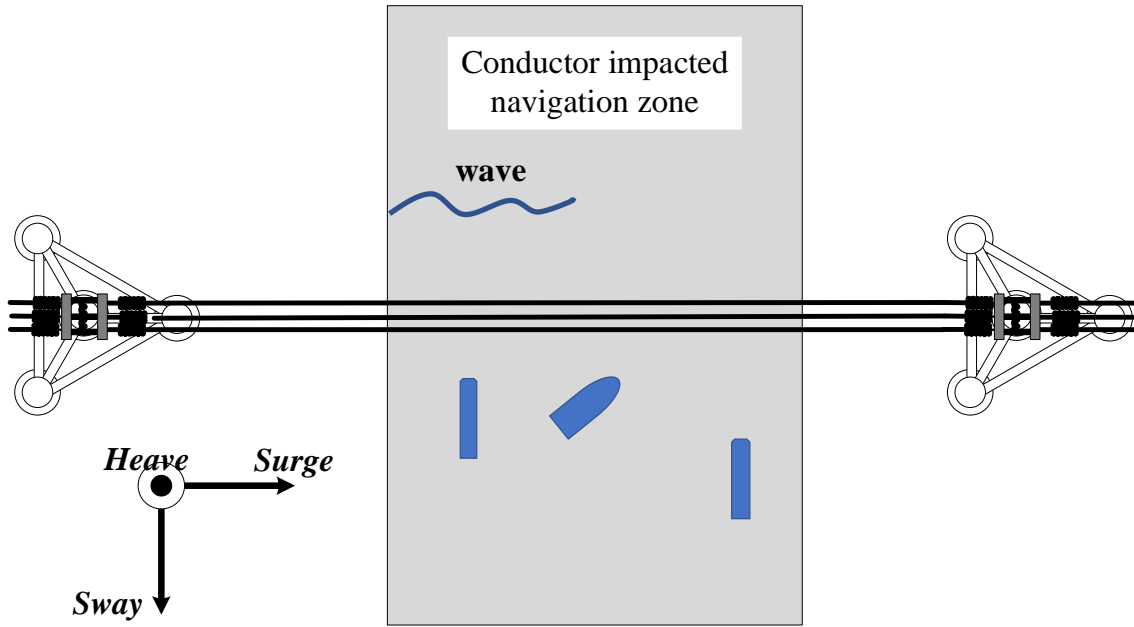
Fig 6-14. Conductor impacted navigation zone of FOPTS

According to the allowable clearance limits specified by the National Electrical Safety Code (NESC) [100], the clearance to open water surfaces can be calculated by Eq. (6-5):

$$Safety\ clearance = \ H_{22} + D_{22\sim}(V - 22),$$ (6-5)

where H_{22} is the reference height when the conductor operates under $22kV$. $D_{22\sim}$ denotes the increasing rate when the operation voltage is large than $22KV$. Values of the two terms are determined by the sailing area shown in Fig 6-14. Considering a safety area of 200 acres, the value of H_{22} is set as 8.7m while $D_{22\sim}$ is $0.012\ m/kV$. Thus, for a $115\ kV$ conductor, the desired clearance should be at least $9.3m$ to vessels on the sea while power transmission is operating.

Table 6-5. Vertical clearance of overhead conductors [100]

Nature of surface Underneath wires, conductors, or cables	Naked conductors with a 22KV operation voltage (m)
Track rails of railroads	8.1
Roads, streets, and other areas subject to truck traffic	5.6
Driveways, parking lots and alleys	5.6
Other land traversed by vehicles, such as cultivated, grazing, forest, or chards, etc	5.6
Spaces and ways subject to pedestrians or restricted traffic only	4.4
Water areas not suitable for sailboating or where sailboating is prohibited	5.2
Water areas suitable for sailboating including lakes, ponds, reservoirs, tidal waters, rivers, streams, and canals with an unobstructed surface area of	
Less than 20 acres	6.2
Over 20 to 200 acres	8.7
Over 200 to 2000 acres	10.5
Over 2000 acres	12.3
Roads, streets, or alleys	5.6
Roads where it is unlikely that vehicles will be crossing under the line	5.0
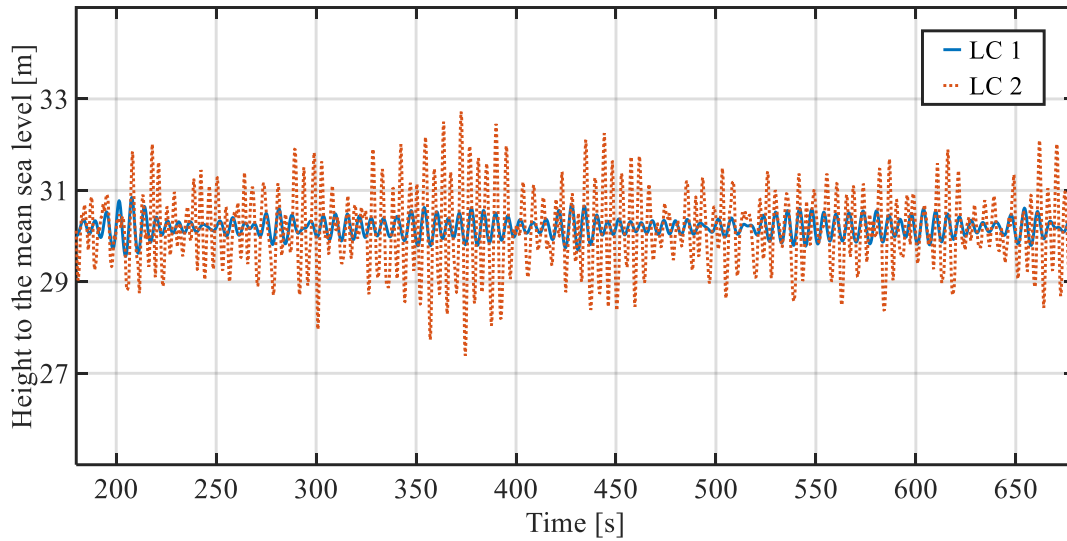
Fig 6-15. Predicted Sag under LC 1 and 2 (ASCR 410mm^2, $\theta_{wave} = 0°, \theta_{wind} = 10°$)

Table 6-6. Clearance of conductor under different environments (ASCR 410mm^2,

$\theta_{wave} = 0°, \theta_{wind} = 10°$)

	LC 1	LC 2	LC 3
Lower bound of clearance	29.4 m	27.2 m	23.1 m

Assuming that the power transmission system is working under LC (Load Case) 1, 2 and 3, the clearance of conductor wire, calculated from time-domain simulations, is given in Table 6-6. Under LC 1 and 2, the clearance of conductor wires to the mean sea level can be kept above $27m$, which indicates an allowance for vessels within $18\,m$ air draft (e.g., 1500-tonnage carriers [101]). Under LC 3, the air draft can be kept below $12\,m$, providing accessibility for the traffic of small-scale ships and carriers in harsh environments.
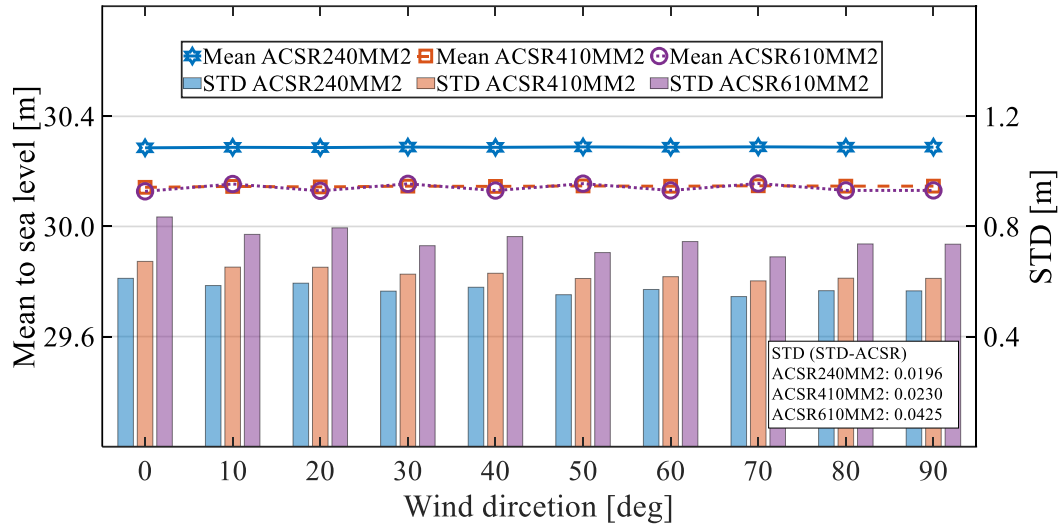
Fig 6-16. Sag of different ACSR by the wind direction (LC 2)
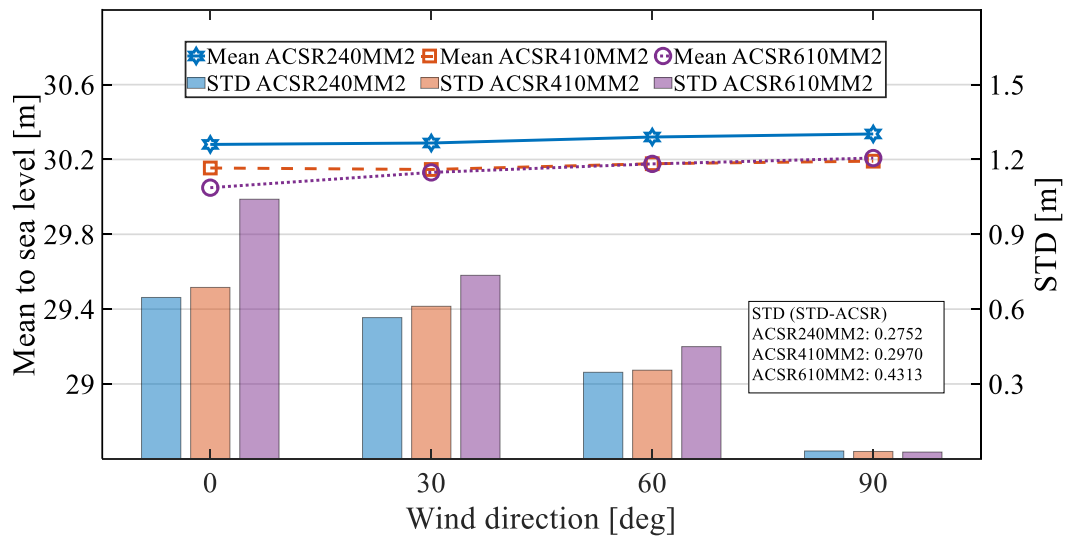
Fig 6-17. Sag of different ACSR by the wave direction (LC 2)

Comparisons of different ACSR type are shown in Fig 6-16 and Fig 6-17. While FOPTS are working for power transmission, ACSR 610mm^2 has the largest sag change to wind-wave excitations (near 1.5 times of others), indicating the same conclusion as Section 6.5.1.1.

6.5.3 On mooring line safety

6.5.3.1 Mild environment

Fig 6-18 shows the mooring line tension in usual environments (LC 1 and 2 in Table 6-2). The tendon would work in a range of 127% pretension, and load amplitude would be limited below 10% EBS. Assuming the equivalent diameter of rope as 0.1m, the rope continuously under daily environments has a $10\ Mpa$ nominal stress range (which can be approximated by standard deviations), which indicates an over-15-year lifetime in the view of fatigue analysis [102-103].
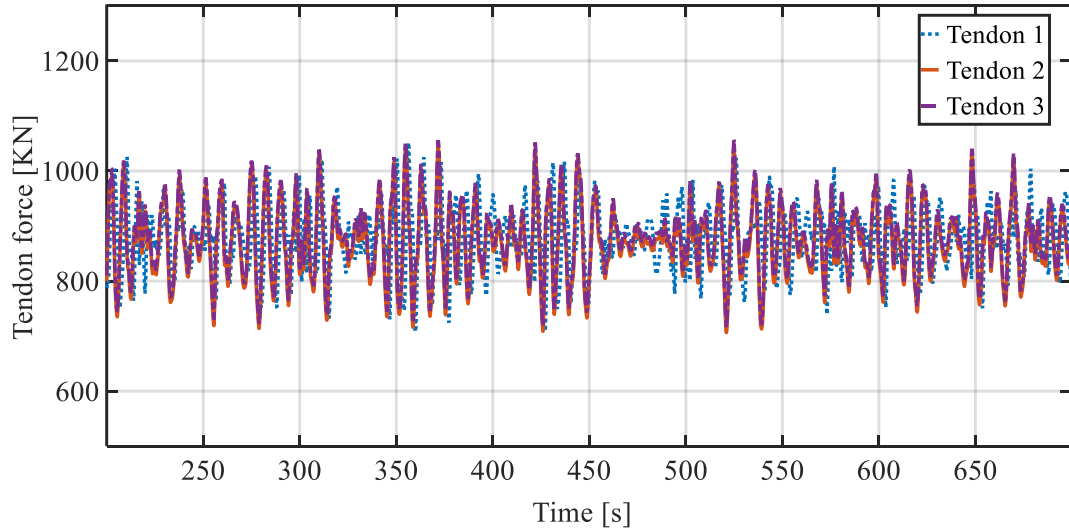
Fig 6-18. Predicted tendon force under LC 2 ($\theta_{wave} = 30°, \theta_{wind} = 60°$)

6.5.3.2 Harsh environment

The tension under an extreme sea environment (LC 4 in Table 6-2) is shown in Fig 6-19. It is observed that the tendons are always tightened under extreme conditions for transverse waves. The max value of tendon force under a transverse wave occurs at the 0° incident wave with 30° wind inflow (202% pretension), which is less than the designed break limit of 275% pretension. Notably, the min tensile force that occurs at the 30° incident wave with a 60° wind inflow, which may be caused by the rapid variation of the yaw motion of the TLP, should be carefully considered for Mathieu stability [104-105] in practical situations.
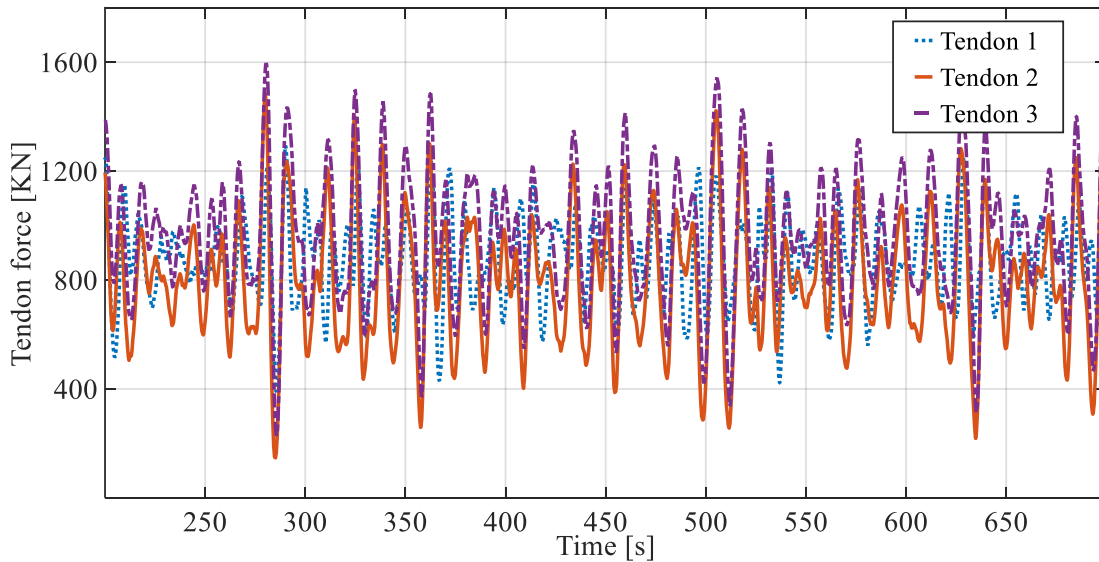
Fig 6-19. Tendon force under LC 4 ($\theta_{wave} = 30°, \theta_{wind} = 60°$)

The effect of the wind direction on mooring tendon tensions is presented in Fig 6-20. Worth noting is that when $\theta_{wave} = 60°$ and the wind speed is relatively low, the

mean tendons of Tendons 1 and 2 are almost the same due to symmetry. With the increase of θ_{wind}, the tendons in the three mooring lines tend to be different. However, the associated standard deviations have smaller variations. Furthermore, under different wave directions, the mean line tendon keeps in between 1.0-1.1F, as shown in Fig 6-21. In the 90° incident wave, the standard deviations of the tendon tensions tend to be the same.

Due to the fact that the underwater part of the FOPTS is much larger than the rest part, the mooring tendon tensions are mainly controlled by wave forces unless in strong winds. The mean value and the standard deviation of the mooring tendon tensions are generally at a comparable level, indicating that the mooring system has a good function in station-keeping of the FOPTS. Furthermore, the averaged mooring tension in Tendon 3 (at the lee side of the incident wave) is relatively large, and the standard deviation in correspondence also increases a little bit.
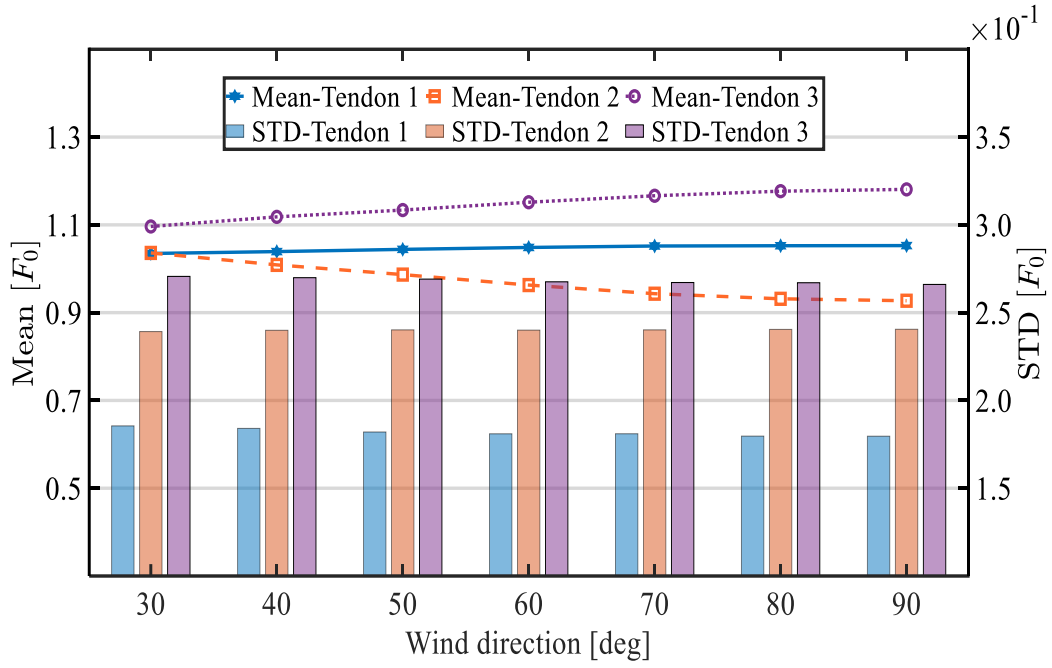
Fig 6-20. Tendon force under different θ_{wind} ($\theta_{wave} = 60°$, LC 4, F_0 denoting the pretension).
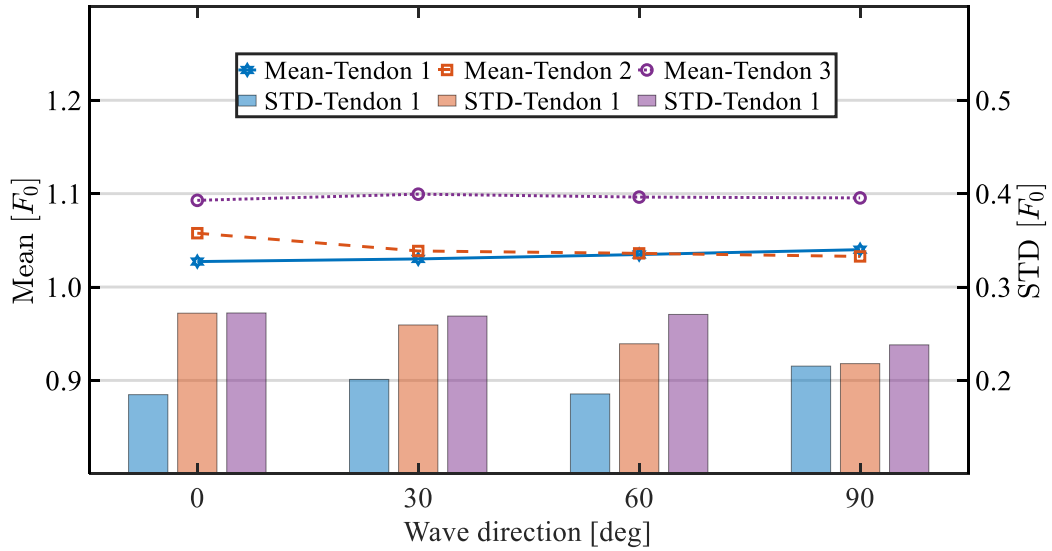
Fig 6-21. Tendon force under different θ_{wave} ($\theta_{wind} = 30°$, LC 4)

6.6 On second order wave force

As an essential part of irregular wave load, the second-order wave force, which is calculated in the formula (2-24), is discussed for its effect on the FOPTS simulation. The effect of second-order wave force is defined as:

$$effect = \frac{V_{2nd} - V_{no2nd}}{V_{no2nd}}$$

where V is the value of conductor tension.

Different values of everyday stress (EDS) are employed as simulation conditions to make contrasts. From the time-domain simulation, the max value and standard division (STD) are calculated for the indicators.

Fig 6-22 shows the effect under the condition of $\theta_{wind} = 0°$. It is found that the second-order wave force reflects a smaller effect on the conductor tension while the EDS increases. The max effect occurs in the wave direction 30° or 60°, which indicates the drive from multi-DOFs would amplify the second-order wave force effect. When the EDS decreases to 15%, the effect of second-order wave force reaches a state of 7% and plays a significant role in the prediction of the conductor dynamics.

(b)

(c)
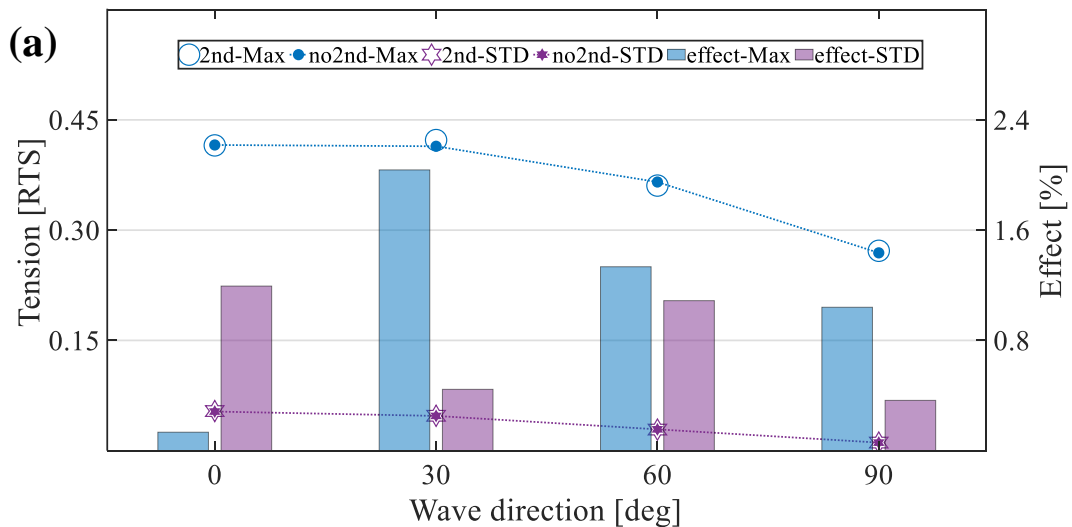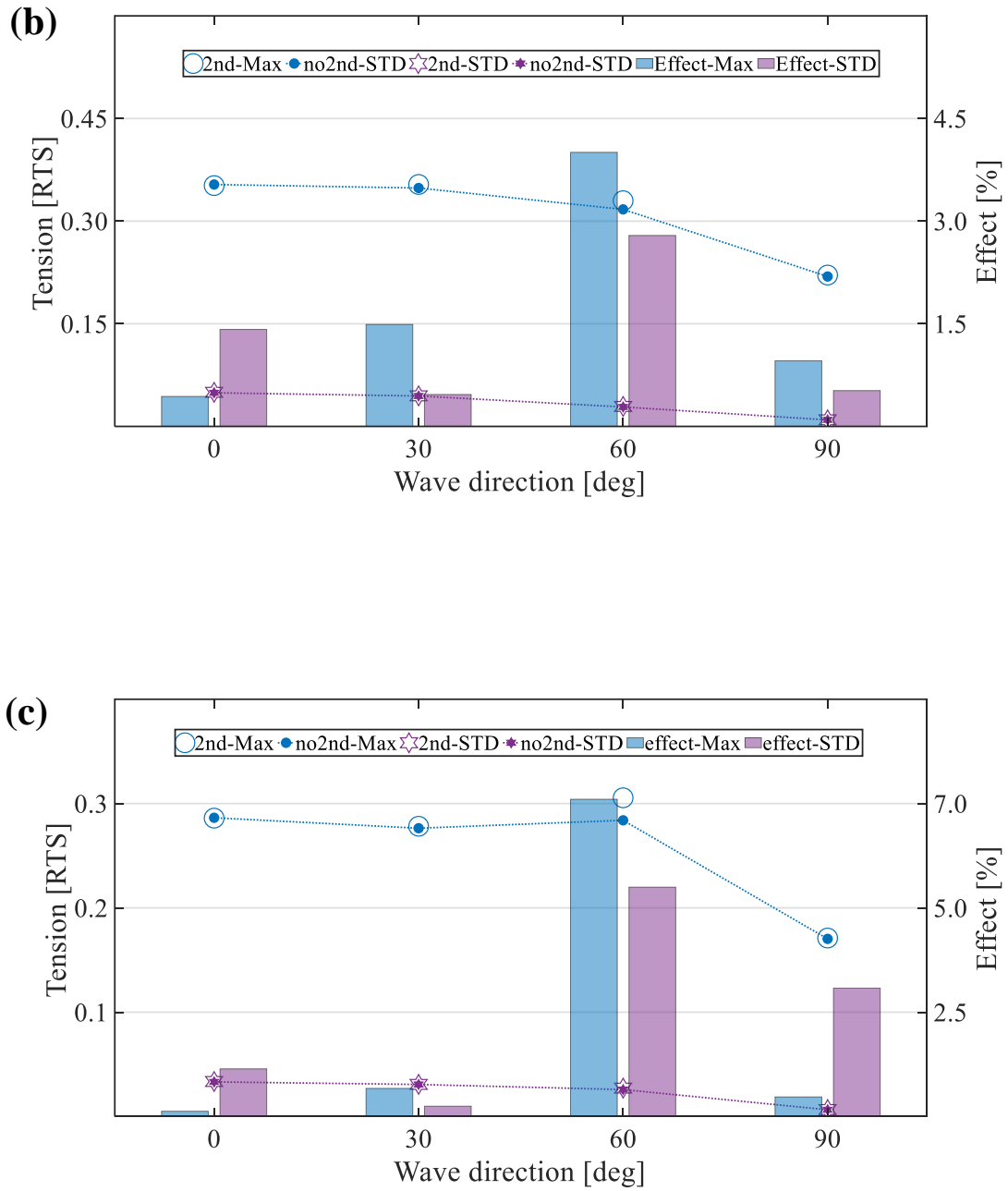
Fig 6-22. The effect of 2nd order wave force under $\theta_{wind} = 0°$: (a) EDS=25%RTS; (b) EDS=20%RTS; (c) EDS=15%RTS.

The effect under a wind direction of 90° is shown in Fig 6-23. When the conductor is highly tensioned at high wind speeds, the effect of second-order wave force is relatively much smaller than the situation of θ_wind=0°, indicating that the high wind speed will suppress the conductor's multi-DOF motion caused by TLP. It is also found that the effect was not significantly related to the EDS, which shows the aerodynamic load will affect the FOPTS more when the conductor is highly tensioned by the wind.

Overall, the max effect on the conductor occurs at the wave direction of 30° or 60° , once again proving the importance of the wind-wave misalignment in the FOPTS numerical research.
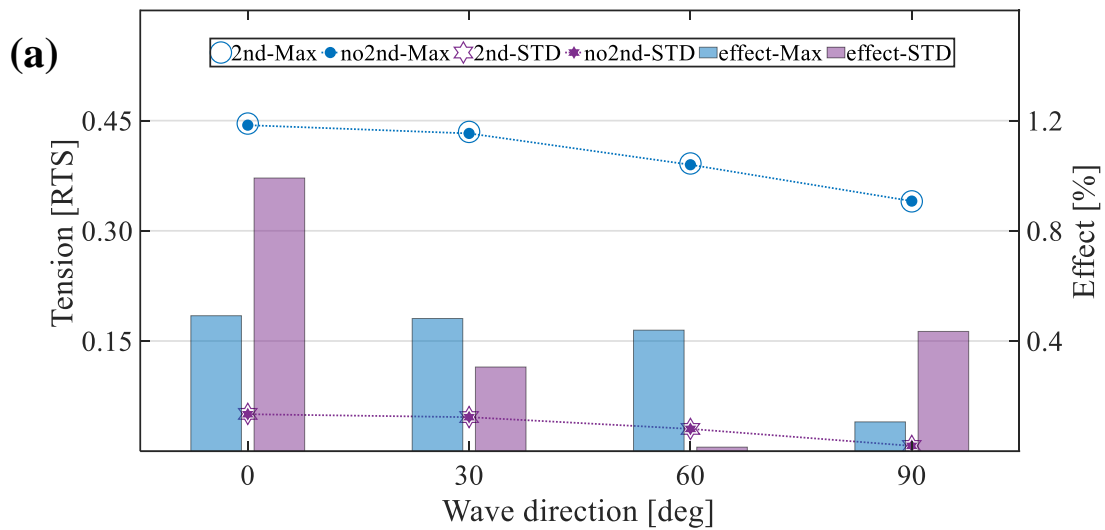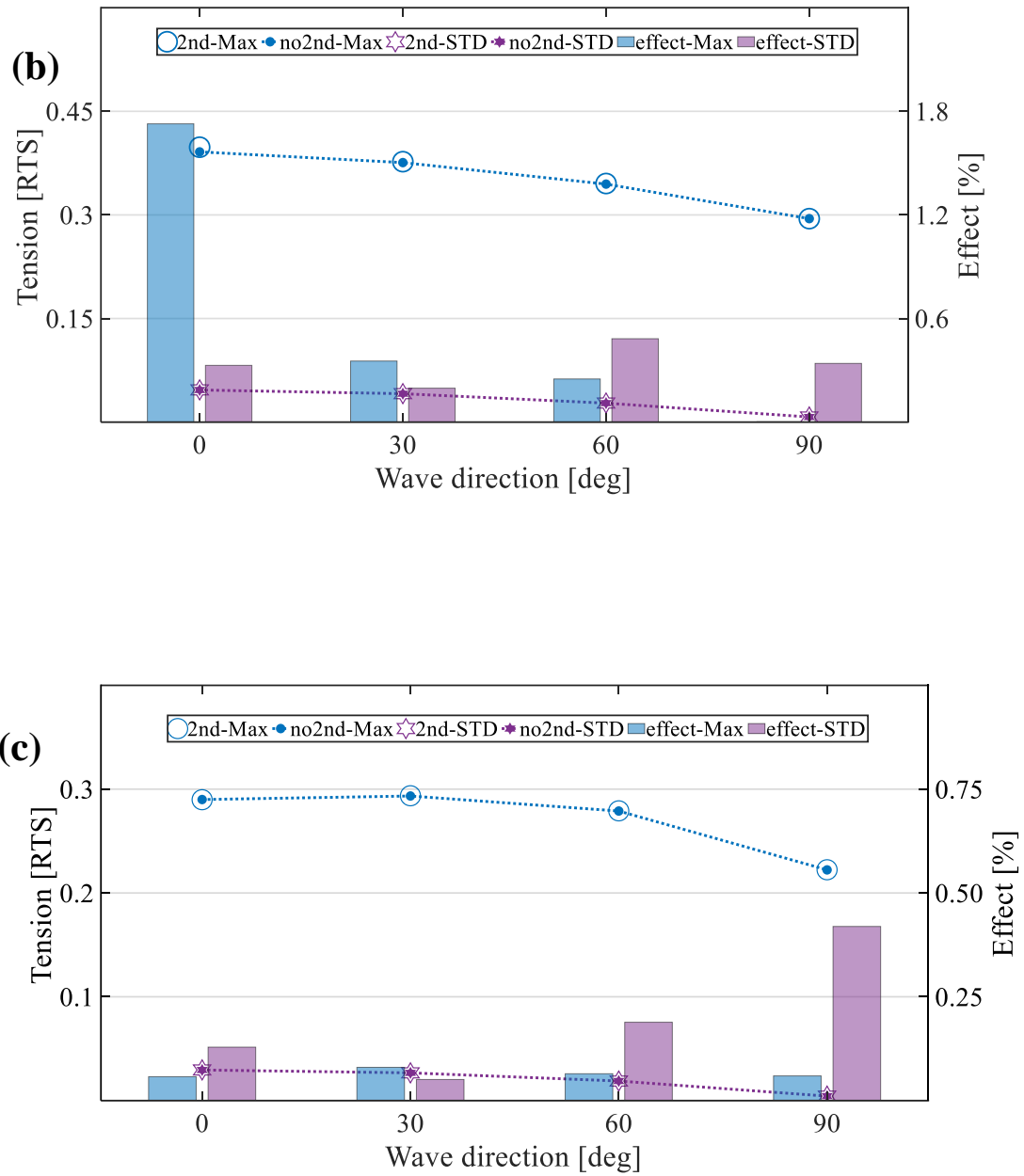
Fig 6-23. The effect of 2nd order wave force under $\theta_{wind} = 90°$: (a) EDS=25%RTS; (b) EDS=20%RTS; (c) EDS=15%RTS.

6.7 Conclusion

The reliability of FOPTS is discussed in this chapter by numerical investigations. Major findings are listed as follows:

(a) The ACSR conductor performs well under the environmental conditions the present study considered. The conductor can have an over-19-year lifetime in view of mechanic fatigue analysis under daily conditions. It reaches a half-RTS tolerance in harsh sea environments, which is acceptable for practical needs.

(b) Design of FOPTS should consider the conductor dynamic. In the present study, ACSR 610mm^2, which has smaller electrical resistance and the highest conductivity efficiency, behaves worse under the offshore environment, which should be noticed while the conductor option.

(e) The most dangerous situation for the FOPTS occurs in harsh waves and strong wind conditions. The wind-wave misalignment significantly affects the low bound of tendon force. Furthermore, the Mathieu stability should be carefully considered because of the near-zero tension.

(f) Given navigational safety requirements, the current design could allow vessels with a safe air draft to cross the sea area in typical sea environments.

(g) The study for the second wave force effect is conducted in Section 6.6. The effect is lower than 3% under the design condition of a 25% RTS pretension, which is negligible in the evaluation of FOPTS.

(h) The low EDS will amplify the effect of second-order wave force on the conductor. The effect will also become more significant when the wave is not in parallel with the axial direction of the conductor.

(i) The wind-wave misalignment will affect the conductor dynamics according to the simulation in Section 6.5, and the calculation accuracy is also affected by it. This proves that the wind-wave misalignment is an essential factor in the prediction of FOPTS.

CHAPTER VII

Conclusion and future work

Floating overhead power transmission system (FOPTS) is a newly proposed solution to offshore power transmissions. Due to its advantages in cost and standardization process, the FOPTS is expected to be an option of offshore power transmission in the future offshore wind power (OWP) industry. To realize the concept, there are many challenges to be overcome, and the following important topics have been studied in this research.

(1) Design and improvement of a floating transmission tower foundation for FOPTS.

(2) Development of a reliable numerical simulation method for coupled analysis of hydrodynamics and aerodynamics.

(3) Safety investigation of the proposed FOPTS under extreme offshore environments.

Experimental and numerical investigations have been carried out. A numerical tool has been developed in this research. The hydrodynamics model, the aerodynamics model, and the mooring line calculation model by using MATLAB functions, the TLP rigid body model by using Simscape®, have been separately developed and they are finally combined. By comparing to the experimental measurements in the wave tank and the wind tunnel tests, it is found that the combination of a hybrid model for hydrodynamics and a wake-oscillation model for aerodynamics is a reasonable approach to model the FOPTS. This approach have been used in the numerical investigation of safety issues for the FOPTS in the real sea environments.

Through the numerical investigation, it is found that the proposed FOPTS is hydrodynamically and aerodynamically safe under daily offshore conditions. The use of sheave can effectively suppress the dynamic tension of the conductor so as not to

exceed its rated tensile strength (RTS), which indicates the FOPTS feasibility. Other major findings from this study can be summarized as follows:

(i) The frequency design is proved effective in the FOPTS study.

(ii) The three-legged TLP shows good hydrodynamics and affords to support the overhead conductor in the offshore environment.

(iii)   Subharmonic resonance is the main factor which would affect the safety of overhead conductors under mild environmental conditions. It is worth paying more attention to the conductor dynamics at high frequencies.

(iv) The wind-wave misalignment is essential in the prediction of overhead conductors. The conductor in a loose state always has a more unstable performance in the offshore environment.

(v) The conductor option should also consider the environmental effect. An overweight conductor, which has higher power transmission efficiency, may behave worse under harsh conditions.

It is worth noting that the present research aims to provide options for offshore power transmission and contribute to the development of offshore wind energy. However, there are still many challenges to overcome in order to achieve this goal.

One problem is that the simplified QTF method used in the study may not accurately reflect the wave loads at low-frequency and high-frequency, which may affect the accuracy of the motion prediction of overhead conductors in FOPTS. A complete method is desired in the future.

Another problem is the linear approximation of the conductor, which may not sufficient for the FOPTS. Since the conductor dynamics is an essential part of the safety assessment for FOPTS, a nonlinear model should be put on the table for the next step of

the study.

The third problem is related to the experiment. The experiments on wave-induced motion and wind-induced motion are performed separately to validate the hydrodynamics model and aerodynamics model. In the future it is expected to perform a model test in the wind-wave tank, in which the coupled wind-wave effect can be investigated directly and precisely.

Bibliography

[1] R. Pelc, R. M. Fujita. Renewable energy from the ocean. *Marine Policy* 2002; 26: 471–479. DOI: 10.1016/S0308-597X(02)00045-3.

[2] N. Khan, A. Kalair, N. Abas, A. Haider. Review of ocean tidal, wave and thermal energy technologies. *Renewable and Sustainable Energy Reviews* 2017; 72: 590–604. DOI: 10.1016/j.rser.2017.01.079.

[3] M. Melikoglu. Current status and future of ocean energy sources: A global review. *Ocean Engineering* 2018; 148: 563–573. DOI: 10.1016/j.oceaneng.2017.11.045.

[4] P. Q. P. Nguyen, V. H. Dong. Ocean energy–A clean, renewable energy source. European Journal of Engineering Research and Science 2019; 4:5-11. DOI: 10.24018/ejers.2019.4.1.1062.

[4] Carlos V.C.Weiss, Raúl Guanche. Marine renewable energy potential: A global perspective for offshore wind and wave exploitation. *Energy Conversion and Management* 2018; 177: 43-54. DOI: 10.1016/j.enconman.2018.09.059

[5] M. Lehmann, F. Karimpour, C. A. Goudey, P. T. Jacobson, M.-R. Alam. Ocean wave energy in the united states: Current status and future perspectives. *Renewable and Sustainable Energy Reviews* 2017; 74:1300–1313. DOI: 10.1016/j.rser.2016.11.101.

[6] M.deCastro, S.Salvador, M.Gómez-Gesteira,etc. Europe, China and the United States: Three different approaches to the development of offshore wind energy. *Renewable and Sustainable Energy Reviews* 2019; 109: 55-70. DOI: 10.1016/j.rser.2019.04.025.

[7] https://www.ren21.net/reports. *Renewables Global Status Report*, (2021)

[8] D. Zhang, J. Wang, Y. Lin, Y. Si, C. Huang, J. Yang, B. Huang, W. Li. Present situation and future prospect of renewable energy in China. *Renewable and Sustainable Energy Reviews* 2017; 76: 865–871. DOI: 10.1016/j.rser.2017.03.023.

[9] https://www.upstreamonline.com/energy-transition/china-overtakes-uk-with-world-s-largest-offshore-wind-power-capacity/2-1-1044437. China overtakes UK with world's largest offshore wind power capacity, Energy Transition, Upstream. 26 July 2021.

[10] deCastro. M, Costoya. X, etc. An overview of offshore wind energy resources in Europe under present and future climate. *Annals of the New York Academy of Sciences*

2019; 1436: 70-97. DOI: 10.1111/nyas.13924.

[11] Dilara Gulcin Caglayan, David Severin Ryberg, etc. The techno-economic potential of offshore wind energy with optimised future turbine designs in Europe. *Applied Energy* 2019; 255. DOI: 10.1016/j.apenergy.2019.113794.

[12] https://windeurope.org. European offshore wind farms map. *WindEUROPE* 2023.

[13] Munim Kumar Barai, Bidyut Baran Saha. Energy Security and Sustainability in Japan. *Evergreen* 2015; 2(01):49-56. DOI: 10.5109/1500427.

[14] Kana Moroga, Akiya Nagata, Yasutaka Kuriyama, Toshiya Kobayashi, Koichi Hasegawa. State of Implementation of Environmental and Energy Policies Adopted by the Regional Governments in Japan. *Evergreen* 2015; 2(02):14-23. DOI: 10.5109/1544076.

[15] Hiroki Gima, Tsuyoshi Yoshitake. A Comparative Study of Energy Security in Okinawa Prefecture and the State of Hawaii. *Evergreen* 2016; 3(02):36-44. DOI: 10.5109/1800870.

[16] Yoshinori Ueda. The Recent Offshore Wind Power Development. *Journal of the Japan Institute of Energy* 2018; 97:25-134. DOI: 10.20550/jieenermix.97.2_125.

[17]https://www.enecho.meti.go.jp/category/saving_and_new/saiene/yojo_furyoku/dl/vision/vision_first.pdf. Offshore wind industry vision of Japan. *Ministry of Economic, Trade and Industry* 2020; Japan.

[18] Firestone, A. W. Bates, A. Prefer. Power transmission: Where the offshore wind energy comes home, Environmental Innovation and Societal. *Environmental Innovation and Societal Transitions* 2018; 29 : 90–99. DOI: 10.1016/j.eist.2018.06.002.

[19] Rodney Itiki, Silvio Giuseppe Santoa ,Cinthia Itiki, Madhav Manjrekar, Badrul Hasan Chowdhury. A comprehensive review and proposed architecture for offshore power system. *International Journal of Electrical Power & Energy Systems* 2019; 111: 79-92. DOI: 10.1016/j.ijepes.2019.04.008.

[20] Sheng-Wei Huang, Edward Chen, and Jenhwa Guo. Efficient Seafloor Classification and Submarine Cable Route Design Using an Autonomous Underwater Vehicle. *IEEE Journal of Oceanic Engineering* 2018; 43(1): 7-18. DOI: 10.1109/JOE.2017.2686558.

[21] Valeriu-Florian VASILESCU, Dumitru DINU. Installation Of Submarine Cables In

The Offshore Wind Industry And Their Impact On The Marine Environment. *Journal of Marine Technology and Environment* 2021; 1:43-51. DOI: 10.53464/JMTE.01.2021.07.

[22] I. M. De Alegria, J. L. Mart´ın, I. Kortabarria, J. Andreu, P. I. Ere˜no. Transmission alternatives for offshore electrical power. *Renewable and sustainable energy reviews* 2009; 13(5):1027–1038. DOI: 10.1016/j.rser.2008.03.009.

[23] W. Fischer, R. Braun, I. Erlich. Low frequency high voltage offshore grid for transmission of renewable power. *3rd IEEE PES Innovative Smart Grid Technologies Europe (ISGT Europe)* 2012. DOI: 10.1109/ISGTEurope.2012.6465646.

[24] Ed L. Pope, Peter J. Talling, Lionel Carter. Which earthquakes trigger damaging submarine mass movements: Insights from a global record of submarine cable breaks? *Marine Geology* 2017; 384: 131-146. DOI: 10.1016/j.margeo.2016.01.009.

[25] A. Myhr, C. Bjerkseter, A. Agotnes, T. A. Nygaard. Levelised cost of energy for offshore floating wind turbines in a life cycle perspective. *Renewable energy* 2014; 66:714–728. DOI: doi.org/10.1016/j.renene.2014.01.017.

[26] G. Liu, J. Cao, Y. Lu. Selection Criteria of High-voltage Submarine Cables for Offshore Wind Farms by Life Cycle Cost. *High Voltage Engineering* 2015; 41:2674-2680. DOI: 10.13336/j.1003-6520.hve.2015.08.019.

[27] Kristen R. Schell, João Claro, Seth D. Guikema. Probabilistic cost prediction for submarine power cable projects. *Electrical Power and Energy Systems* 2017; 90: 1–9. DOI: 10.1016/j.ijepes.2017.01.017.

[28] Kalair, N. Abas, N. Khan. Comparative study of hvac and hvdc transmission systems. *Renewable and Sustainable Energy Reviews* 2016; 59:1653–1675. DOI: 10.1109/PES.2007.385993.

[29] I. Ushiyama, H. Nagai, T. Saito, etc. Japan's Onshore and Offshore Wind Energy Potential as well as Long-term Installation Goal and Its Roadmap by the Year 2050. *Wind Energy* 2010; vol 34. DOI: 10.1260/0309-524X.34.6.701.

[30] Yoshinori Ueda. The Recent Offshore Wind Power Development. *Journal of the Japan Institute of Energy* 2018; 97:25-134. DOI: 10.20550/jieenermix.97.2_125.

[31] X. Wu, Y. Hu, Y. Li, J. Yang, L. Duan, T. Wang, T. Adcock, Z. Jiang, Z. Gao, Z. Lin, et al. Foundations of offshore wind turbines: A review. *Renewable and Sustainable Energy Reviews* 2019; 104:379–393. DOI: 10.1016/j.rser.2019.01.012.

[32] Dominique Roddier, Christian Cermelli, Alexia Aubault,etc. WindFloat: A floating foundation for offshore wind turbines. *Journal of Renewable and Sustainable Energy* 2010; vol 2. DOI: 10.1063/1.3435339.

[33] M. Kausche. F. Adam, F. Dahlhaus, J. Großmann. Floating offshore wind economic and ecological challenges of a TLP solution. *Renewable Energy* 2018; 126: 270–280. DOI: 10.1016/j.renene.2018.03.058.

[34] A.Martinez,G.Iglesias. Site selection of floating offshore wind through the levelised cost of energy: A case study in Ireland. *Energy Conversion and Management* 2022; vol 266. DOI: 10.1016/j.enconman.2022.115802.

[35] S. Bhattacharya. *Design of foundations for offshore wind turbines*. Wiley Online Library; 2019. DOI: 10.1002/9781119128137.

[36] Xuefei Wang,Xiangwu Zeng, Jiale Li, Xu Yang, Haijun Wang. A review on recent advancements of substructures for offshore wind turbines. *Energy Conversion and Management* 2018; 158: 103-119. DOI: 10.1016/j.enconman.2017.12.061.

[37] Xiaoni Wu, Yu Hu, Ye Lia, Jian Yang,Lei Duan, Tongguang Wang, Thomas Adcock, Zhiyu Jiang, Zhen Gao, Zhiliang Lin, Alistair Borthwick, Shijun Liao. Foundations of offshore wind turbines: A review. Renewable and Sustainable Energy Reviews 2019; 104:379-393. DOI: 10.1016/j.rser.2019.01.012.

[38] Yaohua Guo,Haijun Wang, Jijian Lian. Review of integrated installation technologies for offshore wind turbines: Current progress and future development trends. *Energy Conversion and Management* 2022; vol 255. DOI: 10.1016/j.enconman.2022.115319.

[39] Yongsheng Zhao, Jianmin Yang, Yanping He. Preliminary Design of a Multi-Column TLP Foundation for a 5-MW Offshore Wind Turbine. *Energies* 2012; 5: 3874-3891. DOI: 10.3390/en5103874.

[40] Elif Oguz, DavidClelland, Alexander H.Day,etc. Experimental and numerical analysis of a TLP floating offshore wind turbine. *Ocean Engineering* 2018; 147: 591-605. DOI: 10.1016/j.oceaneng.2017.10.052.

[41] Lucie Barj, Jason M. Jonkman, Amy Robertson, etc. Wind-Wave Misalignment in the Loads Analysis of a Floating Offshore Wind Turbine. *32nd ASME Wind Energy Symposium*; 2014. DOI: 10.2514/6.2014-0363.

[42] Erin E. Bachynski, Marit I. Kvittem, Chenyu Luan, Torgeir Moan. Wind-Wave Misalignment Effects on Floating Wind Turbines: Motions and Tower Load Effects. *Journal of Offshore Mechanics and Arctic Engineering* 2014; 136(4). DOI: 10.1115/1.4028028.

[43] Shigeo Yoshida, Tomoaki Utsunomia. Effects of Wave −Wind Directional Misalignment on Dynamic Characteristics and Fatigue Loads of Spar−type Floating Offshore Downwind Turbine. *Japan Society of Mechanical Engineering (JSME) Fluids Engineering Conference*; 2010. DOI: 10.1299/jsmefed.2010.407.

[44] Xiuhe Li, Caichao Zhu, etc. Effects of the yaw error and the wind-wave misalignment on the dynamic characteristics of the floating offshore wind turbine. *Ocean Engineering* 2020; Vol 199. DOI: 10.1016/j.oceaneng.2020.106960.

[45] B.Yeter, Y. Garbatov, C. Guedes Soares. Ultimate strength assessment of jacket offshore wind turbine support structures subjected to progressive bending loading. *Ships and Offshore Structures* 2019; vol 14. DOI: 10.1080/17445302.2018.1484030.

[46] A.Campanile, V.Piscopo,A.Scamardella. Mooring design and selection for floating offshore wind turbines on intermediate and deep water depths. *Ocean Engineering* 2018; 148: 349-360. DOI: 10.1016/j.oceaneng.2017.11.043.

[47] Y. Desai, P. Yu, N. Popplewell, A. Shah. Finite element modelling of transmission line galloping. Computers & structures 1995; 57:407-420. DOI: 10.1016/0045-7949(94)00630-L.

[48] H. Zhu, R. Luo, C. Hu, J. Noda. An experimental study on tower-wire interaction for offshore overhead power transmission concept. *Autumn Meeting of The Japan Society of Naval Architects and Ocean Engineers(JASNAOE)* 2020; pp. 2020A–GS13–4.

[49] C.Hu, H. Zhu, M. Sueyoshi, M. Kobayashi, J. Noda. Tank experiment on the installation process of floating power transmission tower. *The Japan Society of Naval Architects and Ocean Engineers (JASNAOE)* 2020; pp. 2020S–GS13–3.

[50] H. Zhu, C.Hu. A Study on Floating Overhead Power Transmission System for Offshore Energy Development: Design, Modeling and Numerical Analysis. *Ocean Engineering* 2021, vol 236. DOI: 10.1016/j.oceaneng.2021.109528.

[51] T. I. Fossen. Handbook of marine craft hydrodynamics and motion control. *John Wiley & Sons* 2011.

[52] Faltinsen .O .M. Sea loads on ships and offshore structures. *Cambridge University Press* 1990.

[53] Lee, C. H. (1995). WAMIT theory manual. *Massachusetts Institute of Technology*, Department of Ocean Engineering.

[54] Bureau Veritas. Hydrostar for expert's user manual. https://www.docenti.unina.it/webdocenti-be/allegati/materiale-didattico/576434. [accessed on 26/April/2019] (2016).

[55] Liu, Y. (2019). HAMS: A frequency-domain preprocessor for wave-structure interactions—Theory, development, and application. *Journal of Marine Science and Engineering*, 7(3), 81.

[56] Liu, Y., Yoshida, S., Hu, C., Sueyoshi, M., Sun, L., Gao, J., Cong, P. He, G. (2018). A reliable open-source package for performance evaluation of floating renewable energy systems in coastal and offshore regions. *Energy conversion and Management*, 174, 516-536.

[57] Y. M. Low. Frequency domain analysis of a tension leg platform with statistical linearisation of the tendon restoring forces. *Marine structures* 2009; 22 : 480–503. DOI: 10.1016/j.marstruc.2009.01.002.

[58] J. P. Sadler, G. N. Sandor. A Lumped Parameter Approach to Vibration and Stress Analysis of Elastic Linkages. *Journal of Engineering for Industry* 1973; 95(02). DOI: 10.1115/1.3438189.

[59] Mostafa. A. Rushdi, Shigeo Yoshida, Tarek N. Dief. Simulation of a Tether of a Kite Power System Using a Lumped Mass Model, 4th International Exchange and Innovation Conference on Engineering & Sciences (IEICES), 18-19th October, 2018, Fukuoka, Japan.

[60] RC Mac Camy, RA Fuchs. Wave forces on piles: a diffraction theory. *Technical memorandum (United States. Beach Erosion Board)* 1954 ; 69.

[61] O. C. Zienkiewicz, P. Bettess. Fluid-structure dynamic interaction and wave forces. An introduction to numerical treatment. *International Journal For Numerical Methods In Engineering* 1978; 13:1-16. DOI: 10.1002/nme.1620130102.

[62] Safdar Rasool, Kashem M. Muttaqi, Danny Sutanto. Modelling Ocean Waves and an Investigation of Ocean Wave Spectra for the Wave-to-Wire Model of Energy

Harvesting. *Engineering Proceedings* 2021; 12(01). DOI: 10.3390/engproc2021012051.

[63] Y TAMURA. Wake-oscillator model of vortex-induced oscillation of circular cylinder. *Journal of Wind Engineering* 1981. DOI: 10.5359/jawe1980.1981.10_13

[64] Yang Qu, Andrie. V. Metrikine. A single van der pol wake oscillator model for coupled cross-flow and in-line vortex-induced vibrations. *Ocean Engineering* 2020; vol.196. DOI: 10.1016/j.oceaneng.2019.106732.

[65] Devendra K. Chaturvedi. Modeling and Simulation of Systems Using MATLAB and Simulink. *CRC Press* 2010.

[66] Mohd Azizi Abdul Rahman, Makoto Mizukawa. Model-Based Development and Simulation for Robotic Systems with SysML, Simulink and Simscape Profiles. International Journal of Advanced Robotic Systems 2013; 10(02). DOI: 0.5772/55533

[67] Maksym Spiryagin, Scott Simson, Colin Cole, Ingemar Persson. Co-simulation of a mechatronic system using Gensys and Simulink. Vehicle System Dynamics 2012; 50(03):495-507. DOI: 10.1080/00423114.2011.598940.

[68] ww2.mathworks.cn/help/simscape/index.html. MATLAB SIMSCAPE® Manual. Published by Mathworks®.

[69] S. Miller, T. Soares, Y. Van Weddingen, J. Wendlandt. Modeling flexible bodies with Simscape multibody software. Published by Mathworks®.

[70] Changhong Hu, Hongzhong Zhu, M. Sueyoshi, M. Kobayashi, J. Noda. Tank experiment on the installation process of floating power transmission tower. *30th Annual Spring Meeting, the Japan Society of Naval Architects and Ocean Engineers* 2020; Article:2020S-GS13-3.

[71] Hongzhong Zhu, Changhong Hu. A unified seakeeping and maneuvering analysis of multiple linked towing systems with triangular Bodies. *Ocean Engineering*2021; 222. DOI: 10.1016/j.oceaneng.2021.108577.

[72] A Brandt. Noise and vibration analysis: signal analysis and experimental procedures. *John Wiley & Sons* 2011.

[73] Andrew Joseph Goupee; Bonjun Koo; Kostas Lambrakos; Richard Kimball. Model Tests for Three Floating Wind Turbine Concepts. *Offshore Technology Conference* 2012, Houston, Texas, USA. DOI: 10.4043/23470-MS.

[74] Friedrich Kiessling, Peter Nefzger, João Felix Nolasco, Ulf Kaintzyk. Overhead Power Lines: Planning, Design, Construction. Springer Publications; 2003.

[75] M. Irvine (1992). Cable Structures. Dover Publications.

[76] E. Bachynski, T. Moan. Design considerations for tension leg platform wind turbines. *Marine Structures* 2012; 29 (1) :89–114. DOI: 10.1016/j.marstruc.2012.09.001.

[77] S. Chakrabarti. Handbook of Offshore Engineering (2-volume set). *Elsevier* 2005.

[78] E.M Lewandowski. The dynamics of marine craft: maneuvering and seakeeping. *World Scientific Publication* 2004.

[79] Ruo Luo, Hongzhong Zhu, Changhong Hu. A Numerical Investigation of an Offshore Overhead Power Transmission System. *Evergreen* 2022, vol.9, Issue 03. DOI: 10.5109/4842521.

[80] Anton Satria Prabuwono, Habibullah Akbar, Wendi Usino. PC Based Weight Scale System with Load Cell for Product Inspection. *International Conference on Computer Engineering and Technology (IEEE)*2009. DOI: 10.1109/ICCET.2009.182.

[81] Hisato Matsumiya, Takashi Nishihara, Tomomi Yagi. Aerodynamic modelling for large-amplitude galloping of four-bundled conductors. *Journal of Fluids and Structures* 2018; 82:559-576. DOI: 10.1016/j.jfluidstructs.2018.08.003.

[82] C. R. Raghunandan, G. V. Anand. Subharmonic vibrations of order 1/3 in stretched strings. *The Journal of the Acoustical Society of America* 1978; vol 64. DOI: doi.org/10.1121/1.381966.

[83] Mergen H. Ghayesh. Subharmonic dynamics of an axially accelerating beam. *Archive of Applied Mechanics* 2012; 82: 1169–1181. DOI: 10.1007/s00419-012-0609-5.

[84] Den Hartog. *Mechanical vibrations*1985. Dover Publication, New York.

[85] Barth. S. Description of the Relation of Wind, Wave and Current Characteristics at the Offshore Wind Farm Egmond Aan Zee(OWEZ) Location in 2006. *ECN Technical Report* 2007; No. ECN-E-07-104.

[86] Masaru Matsumoto, Hiromichi Shirato, Tomomi Yagi, Mitsutaka Goto, Seiichiro Sakai, Jun Ohya. Field observation of the full-scale wind-induced cable vibration. *Journal of Wind Engineering and Industrial Aerodynamics* 2003; 91:13-26. DOI: 10.1016/S0167-6105(02)00332-X.

[87] Federico Cluni, Vittorio Gusella, Filippo Ubertini. A parametric investigation of wind-induced cable fatigue. *Engineering Structures* 2007; 29: 3094–3105. DOI: 10.1016/j.engstruct.2007.02.010.

[88] Tim Fischer, Patrick Rainey, Ervin Bossany, Martin Kühn. Study on control concepts suitable for mitigation of loads from misaligned wind and waves on offshore wind turbines supported on monopiles. *Wind Engnieering* 2011; 35(5):561-574. DOI: 10.1260/0309-524X.35.5.561.

[89] Hye-Jin Wooa, Kyung-Ae Park. Long-term trend of satellite-observed significant wave height and impact on ecosystem in the East Japan Sea. *Deep Sea Research Part II: Topical Studies in Oceanography* 2017; 143:1-14. DOI: 10.1016/j.dsr2.2016.09.003.

[90] Hye-Jin Wooa, Kyung-Ae Park. Estimation of Extreme Significant Wave Height in the Northwest Pacific Using Satellite Altimeter Data Focused on Typhoons (1992–2016). *Remote Sensing* 2021; 13(6). DOI: 10.3390/rs13061063.

[91] Takeshi Ishihara, Atsushi Yamaguchi, Muhammad Waheed Sarwar. A Study of the Normal Turbulence Model in IEC 61400-1. *Wind Engineering* 2012; 36(6):759-766. DOI: 10.1260/0309-524X.36.6.759.

[92] Arndt Hildebrandt,Boso Schmidt,Steffen Marx. Wind-wave misalignment and a combination method for direction-dependent extreme incidents. *Ocean Engineering* 2019; 180:10-22. DOI: 10.1016/j.oceaneng.2019.03.034.

[93] Matthias Turk, Stefan Emeis. The dependence of offshore turbulence intensity on wind speed. *Journal of Wind Engineering and Industrial Aerodynamics* 2010; 98: 466–471. DOI: 10.1016/j.jweia.2010.02.005.

[94] https://www.kitaniti-td.co.jp/technical/. Technical Material of ACSR Products. Kitanihon Electric Cable Co. Ltd.

[95] R.B.Kalombo, J.M.G.Martínez, J.L.A.Ferreira, C.R.M.daSilva, J.A.Araújo. Comparative Fatigue Resistance of Overhead Conductors Made of Aluminium and Aluminium Alloy: Tests and Analysis. *Procedia Engineering* 2015; 133:223-232. DOI: 10.1016/j.proeng.2015.12.662.

[96] Wadih Naim, Kateryna Morozovska, Patrik Hilber. Effects of Dynamic Line Rating on the Durability and Mechanical Strength of Aluminum Cable Steel Reinforced (ACSR) Conductors. *Energy Procedia* 2019; 158:3164-3169. DOI: 10.1016/j.egypro.2019.01.1019.

[97] Sylvain Goudreau, Frédéric Lévesque, Alain Cardou, Louis Cloutier. Strain Measurements on ACSR Conductors During Fatigue Tests II—Stress Fatigue Indicators. *IEEE Transactions on Power Delivery* 2010; 25:2997-3006. DOI: 10.1109/TPWRD.2010.2042083.

[98] A.V. Mamishev; R.D.Nevels; B.D. Russell. Effects of conductor sag on spatial distribution of power line magnetic field. *IEEE Transactions on Power Delivery* 1996; 11(3): 1571 – 1576. DOI: 10.1109/61.517518.

[99] Adel Z. El Dein, Mohamed A. A. Wahab. The Effects of the Span Configurations and Conductor Sag on the Electric-Field Distribution Under Overhead Transmission Lines. *IEEE Transactions on Power Delivery* 2010; 25(4): 2891-2902. DOI: 10.1109/TPWRD.2010.2051340.

[100] *National Electrical Safety Code*, IEEE Std. **C2-2007**, IEEE, New York, 2006.

[101] Hironao Takahashi, Ayako Goto. Study on Ship Height by Statistical Analysis. *Research Report of National Institute for Land Infrastructure Management (NILIM)* 2006; No.31.

[102] C. Humeau,P. Davies, P. Smeets. Tension fatigue failure prediction for HMPE fiber ropes. *Polymer Testing* 2018; 65:497-504. DOI: 10.1016/j.polymertesting.2017.12.014.

[103] Brett Sanborn, Ann Mae DiLeonardi, Tusit Weerasooriya. Tensile Properties of Dyneema SK76 Single Fibers at Multiple Loading Rates Using a Direct Gripping Method. *Journal of Dynamic Behavior of Materials*2015 1:4-14. DOI: 10.1007/s40870-014-0001-3.

[104] M.H. Patel, H.I. Park. Dynamics of tension leg platform tethers at low tension. Part I - Mathieu stability at large parameters. *Marine Structure* 1991; 3-4(257-273). DOI: 10.1016/0951-8339(91)90004-U.

[105] B.J.Koo, M.H.Kim, R.E.Randall. Mathieu instability of a spar platform with mooring and risers. *Ocean Engineering* 2004; 31(17-18):2175-2208. DOI: 10.1016/j.oceaneng.2004.04.00

Acknowledgement

I would like to express my sincere gratitude to my supervisor, Professor Changhong Hu, for his continuous encouragement and support over the course of this research work. I'm grateful for his important help to my doctoral study, his assistance in revising my publications, his organization of my thesis defense committee and his guidance on my living in Fukuoka.

I would like to express my special appreciation to the staffs of Professor Hu's labolatory: Dr. Yingyi Liu, Dr. Hongzhong Zhu, and Mr. Joshiro Noda. They give me many advices in the study of potential flow theory, experimental manipulation, and English writing. Definitely it would not be possible to complete the dissertation writing without their patient help and collaboration.

Many labmates both seniors and those at my level were also helpful in various ways, from helping with experimental setups to discussions on the theoretical aspects of all my proposed research ideas. There were many types of criticisms that helped me succeed in producing the necessary results to show for the time spent in the PhD program.

Lastly, I would show my heartfelt thanks to my families and friends. They have continuously supported my Japan life over the past three years. I want to dedicate this thesis to my parents, sister, grandmother, and all the people who encouraged me in my overseas career.